Ab-Initio Quantum Phase Diagrams
of Ultracold Atomic Gases
in Optical Lattices

Vom Fachbereich Physik
der Technischen Universität Darmstadt

zur Erlangung des Grades
eines Doktors der Naturwissenschaften
(Dr. rer. nat.)

genehmigte

Dissertation

von

Dipl.-Phys. Felix Schmitt
aus Seeheim-Jugenheim

Darmstadt 2009
D17

Zusammenfassung

Ultrakalte atomare Gase in optischen Gittern bieten einen einzigartigen Rahmen für das Studium von Quantenphänomenen in stark korrelierten Systemen. Jenseits der präzisen Kontrolle über die Parameter im Experiment, können diese Experimente durch ein fundamentales Modell der Festkörperphysik beschrieben werden. Für die bosonische Version dieses Modells, das sogenannte Bose-Hubbard-Modell, wurde ein Phasenübergang von einem Superfluid zu einem Mottisolator theoretisch vorhergesagt und später in einem ultrakalten Gas aus ^{87}Rb Atomen in drei- und eindimensionalen optischen Gittern experimentell nachgewiesen. Neben homogenen optischen Gittern können auch komplexe Gittertopologien wie Zweifarb-Supergitter realisiert werden. Diese führen zu einem facettenreichen Phasendiagramm, in dem exotische Phasen wie das Bose-Glas auftreten.

Wir verwenden verschiedene effiziente Vielteilchentechniken wie exakte Diagonalisierungen in vollständigen und trunkierten Hilberträumen und die Dichte-Matrix Renormierungsgruppen (DMRG) Methode, um die Phasendiagramme des eindimensionalen Bose-Hubbard-Modells sowie des Bose-Fermi-Hubbard-Modells zu untersuchen.

Der Großteil der theoretischen Studien dieser Systeme untersucht die Phasendiagramme als Funktionen der generischen Parameter des Hubbard-Modells. Diese Hubbard-Parameter hängen jedoch in nicht-trivialer Weise von den Kontrollparametern des Experiments ab. Der Schwerpunkt dieser Arbeit ist eine *ab-initio* Berechnung des Phasendiagramms von ^{87}Rb in eindimensionalen optischen Supergittern, welche direkt von einem wohldefinierten Experiment ausgeht. Dazu verwenden wir Bandstrukturrechnungen, um die Hubbard-Parameter aus den experimentellen Parametern zu gewinnen. Zur Lösung des Vielteilchenproblems für realistische Teilchenzahlen und Gittergrößen, die im Experiment auftreten, verwenden wir moderne DMRG Methoden.

Unsere Ergebnisse zeigen, dass allein die Kontrolle der Intensitäten der Laser die das Zweifarb-Supergitter bilden ausreicht, um alle relevanten Quantenphasen des Systems zu realisieren. Wir haben weiterhin herausgefunden, dass die kritischen Intensitäten der Laser, welche die Phasengrenzen bestimmen, von einem dritten Parameter abhängen. Dieser dritte Parameter ist entscheidend für eine realistische Betrachtung des Experiments. Er beschreibt die Stärke eines harmonischen Fallenpotentials, welches das Gauss-förmige Profil der Laser und ein zusätzliches magnetisches Potential zur Lokaliserung der Atome im Zentrum der Falle berücksichtigt.

iv

Summary

Ultracold atomic gases in optical lattices provide an unique framework to study quantum phenomena in strongly correlated systems. In addition to the precise control over all relevant parameters in the experiment, these experiments can be mapped to a fundamental model from solid-state physics. For the bosonic version of this model, the so-called Bose-Hubbard model, a phase transition from a superfluid to a Mott insulator was theoretically predicted and later experimentally observed in an ultracold gas of ^{87}Rb atoms in three-dimensional as well as in one-dimensional optical lattices. Apart from homogeneous optical lattices one can introduce more complex lattice topologies such as two-color superlattices which give rise to a rich phase diagram including more exotic phases like the Bose-glass.

We employ various powerful many-body techniques like exact diagonalization in complete and truncated Hilbert spaces and the Density-Matrix Renormalization Group (DMRG) algorithm to study the phase diagrams of the one-dimensional Bose-Hubbard and the one-dimensional Bose-Fermi-Hubbard Hamiltonian.

Most theoretical studies of these systems discuss the phase diagrams with respect to the generic parameters of the Hubbard model. These Hubbard parameters, however, depend non-trivially on the control parameters used in experiments. The focus of this work is on the *ab-initio* calculation of the phase diagram of ultracold ^{87}Rb in one-dimensional optical superlattices starting directly from the experimental setup. To this end, we first employ band-structure calculations to extract the Hubbard parameters from the experimental parameters. Then, we use state-of-the-art DMRG techniques to solve the many-body problem for realistic particle numbers and lattice sizes that occur in experiments.

Our results show that by using the intensities of the two laser fields forming the two-color superlattice as control parameters while keeping all other experimental parameters fixed, it is possible to access all relevant quantum phases of the system. Furthermore, we found out that the critical values of the laser intensities for the different phase transitions depend strongly on a third parameter that has to be included for a realistic description of the experiment. This third parameter is the strength of a harmonic trapping potential which accounts for the Gaussian shape of the laser fields and an additional magnetic potential used to confine the atoms in the center of the trap.

Contents

Chapter 1

Introduction

Ever since the pioneering work on low temperature physics by Heike Kamerlingh Onnes leading to the discovery of superconductivity in 1911, and to a Nobel Prize in Physics in 1913, the fascination for the cold secrets of nature was a stimulant for many physicists. A theoretical indication for exciting physics at low temperatures was provided in 1924 in Albert Einstein's publication "Quantentheorie des einatomigen idealen Gases" [1], which itself based on a work of Satyendra Nath Bose [2]. In this manuscript, he predicted a new phase of matter at very low temperatures which is nowadays known as the Bose-Einstein condensate. It took more than three decades until in 1957 superconductivity was theoretically understood by John Bardeen, Leon N. Cooper, and John R. Schrieffer as a condensation of correlated electron pairs—the so-called Cooper pairs [3].

Although quantum mechanics is ubiquitous in our daily life, the domain of ultra-low temperature physics is special in the sense that peculiar quantum effects can emerge on macroscopic scales. Bose-Einstein condensates provide a link from the microscopic to the macroscopic world, because in a condensate a single quantum-mechanical state is occupied by a macroscopic number of particles. Indirect hints for new quantum effects have appeared very early, e.g., in the form of superconductivity and superfluidity. And tremendous progress in trapping and cooling techniques for atomic gases finally led to the realization of the first pure Bose-Einstein condensates in 1995 by Wolfgang Ketterle [4], Eric A. Cornell and Carl E. Wieman [5]. They were jointly awarded the Nobel Prize in Physics in 2001.

By now, laboratories all over the world have the expertise to prepare Bose-Einstein

condensates, and the focus has shifted from production towards manipulation of these condensates. Among a wide variety of fascinating experiments in this branch of low-temperature physics, we focus on ultracold atomic gases in optical lattices [6]. In these experiments three standing-wave laser fields, one in each spatial direction cross and result in a three-dimensional periodic potential for the atoms. The experimental setup of the lasers and the resulting optical lattice are illustrated in Figure 1.1. Above a certain
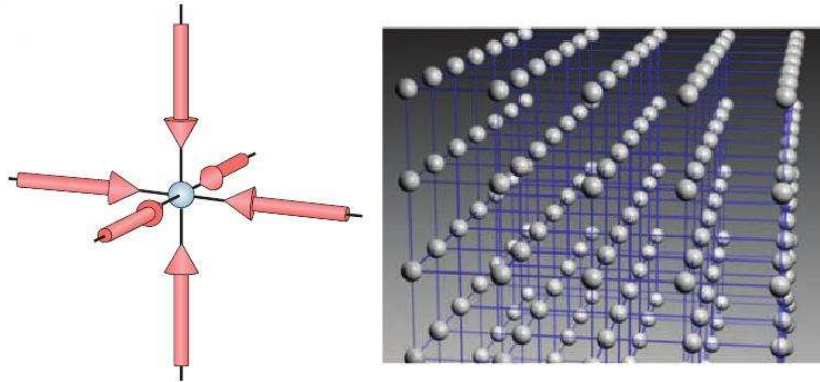
Figure 1.1: Left panel: Three laser beams focus on a spot. Right panel: Zoom into the spot illustrating the sites of the optical lattice. The pictures are taken from [6].

intensity of the laser beams, i.e., a certain optical potential depth, the atoms become localized at the potential minima and only tunneling between these *lattice sites* allows for a residual mobility of the atoms. Furthermore, due to the localization of the atoms at the lattice sites, they interact strongly if they occupy the same lattice site.

Historically, interacting particles in periodic potentials are the domain of solid-state physics. However, the spatial length of the periodicity in the ionic-lattice of a metal is hundreds of picometers while it is typically hundreds of nanometers in optical lattices, i.e., three orders of magnitude larger. By tuning the intensity of the laser beams one has the unique ability to precisely adjust the depth of the periodic potential *in-situ*, and therefore, to continuously control whether tunneling or interaction dominates the behavior of the atoms. Moreover, while electrons, i.e., fermions sit in the periodic potentials in solids, one can put atoms with integer or half-integer spin, i.e., bosons or fermions, or even mixtures in optical lattices, allowing for experiments with different quantum statistics.

From a theoretical point of view, these experiments are also very appealing because they can be mapped to a very fundamental model from solid-state physics, the so-called Hubbard model [7]. Originally formulated in 1963 to describe correlations between electrons in solids, the bosonic version of the Hubbard model, known as the Bose-Hubbard model, predicts a quantum phase-transition[1] form a superfluid to a Mott-insulator [8]. In 2001, this phase transition was observed experimentally [9] using a technique called time-of-flight imaging. Shortly after the ultracold atom cloud is released from the lattice, the resulting density distribution is irradiated with resonant laser light and the absorption is imaged. In the superfluid phase where tunneling dominates, these density distributions show clear interference patterns due to the existing phase coherence between the atoms. In the Mott-insulating phase, however, tunneling is suppressed and the phase coherence is lost, as a result no interference is visible. The time-of-flight images from the experiment are shown in Figure 1.2. This nice correspondence between experi-
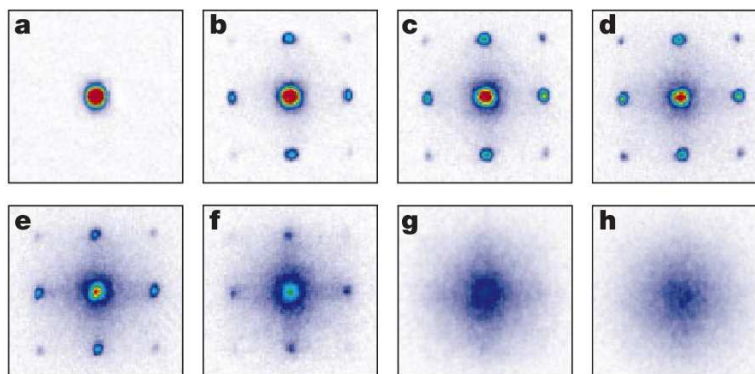
Figure 1.2: Absorption images of multiple matter wave interference patterns. These were obtained after suddenly releasing the atoms from an optical lattice with different potential depths. The time of flight of was 15 ms. The potential depths were: (a) $0\,E_r$, (b) $3\,E_r$, (c) $7\,E_r$, (d) $10\,E_r$, (e) $13\,E_r$, (f) $14\,E_r$, (g) $16\,E_r$, and (h) $20\,E_r$. The recoil energy E_r is the natural energy scale in these systems. The picture is taken from [9].

ment and theory, where observables like the interference patterns can be calculated, was the beginning of a very fruitful collaboration.

One reason for the continuing interest in these systems is the possibility to realize experiments with lower dimensionalities. When one of the laser beams is tuned to very large

---

[1]The terminology quantum phase-transition is due to the quantum fluctuations which drive the phase transition instead of thermal fluctuations in a classical system.

intensities, tunneling along its direction is suppressed and one ends up with a stack of isolated two-dimensional lattice planes. If the intensity of a second beam is increased as well, the result is an array of one-dimensional lattices. In 2004, the superfluid to Mott-insulator transition was observed in such an one-dimensional lattice [10]. Instead of the interference patterns, the excitation spectrum of the atomic gas was used to distinguish the two phases. In the superfluid phase, the system is soft and does not exhibit a gapped excitation spectrum, while sharp excitation peaks appear in the more rigid Mott-insulating phase. The results from the experiment are shown in Figure 1.3.
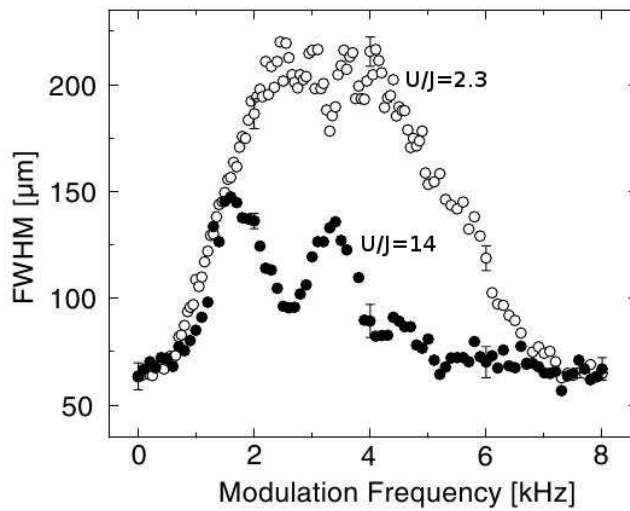
Figure 1.3: Spectroscopy of the 1D superfluid phase (open circles) and the Mott insulating phase (solid circles) with values of U/J of approximately 2.3 and 14, respectively. The system is excited via a modulation of the intensity of the laser beam. The picture is taken from [10].

So far, there are two parameters in Hubbard model: U, the energy scale of the interaction process, and J, the energy scale of the tunneling process. In homogeneous optical lattices, these two parameters uniquely describe the properties of the system. Yet, one can introduce inhomogeneities via an additional energy ϵ_l for each individual lattice site l. These on-site energies account for the topology of an inhomogeneous lattice. In the experiment, these energies appear for different reasons. Usually, an additional magetic trap is used to confine the atoms at the center of the optical crystal. Furthermore, the Gaussian shape of the laser beams also leads to inhomogeneities in the optical lattice. These two potentials are in good approximation harmonic potentials with a minimum at the center of the optical lattice. But also more interesting topologies can be real-

ized. The interference between the generating laser of the optical lattice and a second laser beam of different wavelength leads to a whole set of possible spatial modulations of the optical lattice. This setup is called bichromatic superlattice or two-color superlattice.

The phase diagrams of bosonic atoms in such two-color superlattices were extensively explored theoretically [11, 12, 13, 14, 15, 16, 17, 18]. An example of such a phase diagram is depicted in Figure 1.4. We will not go into details here but point out that the intro-
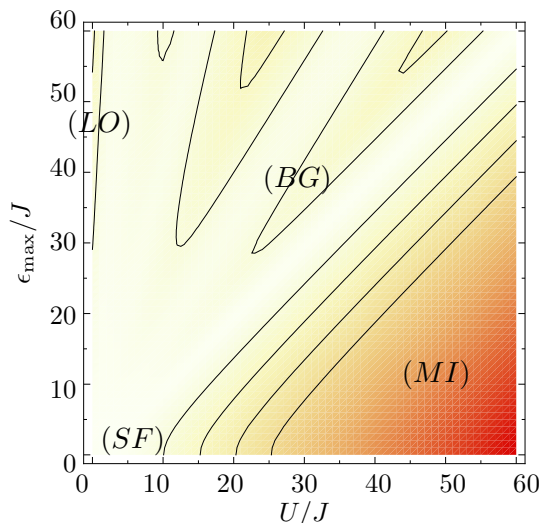
Figure 1.4: Phase diagram of bosonic atoms in a two-color superlattice with 30 lattice sites and 30 particles spanned by U/J and $\epsilon_{\max}/J = \max\{\epsilon_l\}/J$. The labels mark the domains of the superfluid (SF) phase, the homogeneous Mott-insulator (MI) phase, the quasi Bose-glass (BG) phase, and the localized (LO) phase. The picture shows our calculation of the energy gap between ground state and first excited state.

duction of the superlattice leads to a rich phase structure and gives rise to localized and quasi Bose-glass phases in addition to the superfluid and the Mott-insulating regimes.

The major aim of this work is an *ab-initio* calculation of the phase diagram of ultracold atomic gases in optical lattices. We start from a realistic experimental setup and directly express the phase diagrams with respect to the control parameters of the experiment. To this end, we explicitly calculate the Hubbard parameters from a given set of experimental parameters and employ powerful many-body methods like the Density-Matrix Renormalization Group (DMRG) algorithm to obtain the eigenstates of the Bose-Hubbard Hamiltonian for realistic system sizes.

This work is organized as follows. In Chapter 2 we discuss the important basics from solid-state physics and employ band structure calculations to provide a link between the experimental parameters, like the already mentioned laser intensities, and the generic parameters of the Hubbard model.

While three-dimensional optical lattices can be treated theoretically on a mean-field level, correlations play a significant role in one-dimensional systems and a mean-field description is no longer appropriate. Here, one has to resort to powerful exact many-body methods which take all correlations fully into account. In Chapter 3, we use large-scale diagonalization schemes in complete and truncated Hilbert spaces to study the physics of bosons and Bose-Fermi mixtures in two-color superlattices. These exact diagonalization schemes, however, are restricted to moderate system sizes, because the Hilbert space grows factorially with the length of the lattice and the number of atoms.

In order to approach experimentally realized system sizes, we introduce in Chapter 4 the DMRG method, which is currently the most powerful numerical tool for one-dimensional lattice systems.

In most previous studies, the phase diagrams were spanned using the generic Hubbard parameters U, J, and $\epsilon_{\max}$ directly. This is sufficient as long as the model itself is the focus of the research. Yet, these parameters depend non-trivially on the real experimental parameters. In Chapter 5 we establish a direct connection to the experiment and combine the computation of the Hubbard parameters for the experimental lattice with DMRG solutions of the many-body problem to provide the first *ab-initio* calculations of the phase diagram of ^{87}Rb atoms in a realistic experimental setup. We furthermore use this framework to directly compare findings from the experiment with our numerical calculations.

Finally, in Chapter 6 we leave the physics of ultracold atoms in optical lattices and study an experimental setup designed by the group of Gerhard Birkl from the TU Darmstadt [19]. In their experiment they have built an one-dimensional optical ring potential. This ring potential is used as a waveguide for a Bose-Einstein condensate of ^{87}Rb atoms. We describe the interacting Bose-Einstein condensate via the one-dimensional Gross-Pitaevskii equation. For the time evolution of the condensate we use the so-called Split-Operator Fast-Fourier Transformation (SOFFT) method. In this framework we

are able to provide a first insight into relevant time scales, geometries, and potential depths which could be helpful for the design of the experiment.

Chapter 2

Hubbard Model & Hubbard Parameters

2.1   Periodic Potentials, Bloch vs. Wannier Functions

Since the Hubbard model plays a key role in this work, we provide a brief introduction to the relevant fundamentals of solid-state physics. The natural basis for single particles in periodic potentials are delocalized quasi-momentum eigenfunctions—the so-called Bloch functions. However, the Hubbard model is formulated with respect to localized Wannier functions. We will show how the latter can be derived from Bloch functions, and motivate why they provide a convenient description of ultracold atoms in optical lattices. For a detailed discussion of the physics in periodic potentials the reader may refer to any solid-state textbook, e.g. [20].

The optical potentials used in experiments are realized via counter-propagating laser beams which form a standing wave. If the lasers are red-detuned with respect to an atomic resonance, the atoms feel an increasingly attractive potential with increasing intensity due to the AC-Stark effect [21]. The intensity maxima then mark the lattice sites. Three of those standing-wave laser fields, one from each spatial direction, cross and form a 3D crystal of light as illustrated in Figure 1.1. In order to realize a 1D setup, two of the beams are tuned to large intensities resulting in an array of onedimensional tubes between which tunneling is suppressed. The tubes are elongated along the x-direction and the potential along this direction is defined by the third pair of laser beams with wavelength λ and potential depth V_0:

$$V_{\mathrm{opt}}(x) = V_0 \sin^2\left(\frac{2\pi}{\lambda}x\right), \qquad V_0 = s \cdot E_r = s \cdot \frac{\hbar^2 4\pi^2}{2m\lambda^2}. \tag{2.1}$$

The optical potential is usually expressed in units of the *recoil energy* E_r which is the kinetic energy a particle of mass m obtains through absorption of a single photon of wavelength λ. The experimental control parameter is the dimensionless parameter s which sets the laser intensity that is proportional to the potential depth of the optical lattice.

The single-particle Hamiltonian including the periodic optical potential is of the form

$$\hat{H} = \frac{\hat{p}^2}{2m} + V_{\text{opt}}(\hat{x}), \tag{2.2}$$

which leads to the coordinate space representation

$$H_x = -\frac{\hbar^2}{2m}\frac{\partial^2}{\partial x^2} + V_{\text{opt}}(x). \tag{2.3}$$

We will now exploit the periodicity of the potential to derive the corresponding eigenfunctions. Due to the periodicity, a shift of half a wavelength leads to an identical point in the potential. To generate a shift we formally introduce the translation operator T_{ξ_l}, where $\xi_l = la$ shall be an integer multiple of the lattice constant $a = \lambda/2$ and l labels the different lattice sites

$$T_{\xi_l} V_{\text{opt}}(x) = V_{\text{opt}}(x + \xi_l) = V_{\text{opt}}(x). \tag{2.4}$$

For convenience, let us also assume periodic boundary conditions which connect both ends of the optical lattice via $V_{\text{opt}}(x + L) = V_{\text{opt}}(x)$. If there are I minima over the length $L = I \cdot a$, a shift of the form $(T_a)^I$ leads back to the starting point, i.e., $(T_a)^I = 1$. Therefore, the eigenvalues of the translation operator are complex roots

$$(T_a)^I = 1 \ \Rightarrow \ (T_a)^j = e^{\mathbf{i}\frac{2\pi}{Ia}ja} \qquad \text{with} \qquad j = 0, 1, 2, \ldots, I-1, \tag{2.5}$$

where in the exponent we define a momentum $\frac{2\pi}{Ia}j = \frac{2\pi}{L}j = k_j$.

Since the Hamiltonian commutes with the translation operator they share the same eigenbasis. An eigenfunction that reproduces the correct eigenvalues of the translation operator is of the form

$$\psi_{k_j}^{(i)}(x) = e^{\mathbf{i}k_j x} \cdot u_{k_j}^{(i)}(x), \qquad \text{with} \qquad u_{k_j}^{(i)}(x + \xi_l) = u_{k_j}^{(i)}(x), \tag{2.6}$$

and thus

$$T_{\xi_l}\psi_{k_j}^{(i)}(x) = \psi_{k_j}^{(i)}(x + \xi_l) = e^{\mathbf{i}k_j\xi_l}\psi_{k_j}^{(i)}(x). \tag{2.7}$$

Equation (2.6) is known as Bloch's theorem [20]. The plane-wave $e^{\mathbf{i}k_j x}$ reflects the generic part of the function determined by the allowed quantized momenta in a box of length L. The non-trivial part of $\psi_{k_j}^{(i)}(x)$ is given by the momentum-dependent function $u_{k_j}^{(i)}(x)$ which shares the periodicity of the potential. If no potential is present, $u_{k_j}^{(i)}(x)$ would be a constant.

In order to obtain Bloch functions for a given potential, we solve the eigenvalue problem numerically. The energy eigenvalues of the Hamiltonian are two-fold degenerate for $\pm k_j$ and exhibit a band structure. There are as many eigenvalues in a band as there are minima in the potential. The eigenfunctions defined by

$$\hat{H} \mid \phi_{k_j}^{(i)} \rangle = \epsilon_j^{(i)} \mid \phi_{k_j}^{(i)} \rangle \tag{2.8}$$

are not necessarily Bloch functions, but may be any superposition within the $\pm k_j$ subspace. Thus, we have to solve the 2×2 eigenvalue problem for the translation operator within the subspace of degenerate eigenfunctions to obtain Bloch functions which satisfy Eq. (2.7). For convenience, we formally define the translation operator in bra-ket notation as $\langle x \mid \hat{T}_{\xi_l} \mid \psi \rangle = \psi(x + \xi_l)$ and drop the index i for a moment. We expand the Bloch function in the degenerate subspace via

$$\mid \psi_{k_j} \rangle = c_{k_j}^+ \mid \phi_{k_j} \rangle + c_{k_j}^- \mid \phi_{-k_j} \rangle \,. \tag{2.9}$$

If we now we apply a shift

$$\hat{T}_a \mid \psi_{k_j} \rangle = \hat{T}_a \left(c_{k_j}^+ \mid \phi_{k_j} \rangle + c_{k_j}^- \mid \phi_{-k_j} \rangle \right) , \tag{2.10}$$

the translation operator has to reproduce the correct eigenvalue

$$\hat{T}_a \mid \psi_{k_j} \rangle = e^{\mathbf{i}k_j a} \mid \psi_{k_j} \rangle = e^{\mathbf{i}k_j a} \left(c_{k_j}^+ \mid \phi_{k_j} \rangle + c_{k_j}^- \mid \phi_{-k_j} \rangle \right) . \tag{2.11}$$

Multiplication with the bras leads to the matrix representation of the eigenproblem

$$\begin{pmatrix} \langle \phi_{k_j} \mid \hat{T}_a \mid \phi_{k_j} \rangle & \langle \phi_{k_j} \mid \hat{T}_a \mid \phi_{-k_j} \rangle \\ \langle \phi_{-k_j} \mid \hat{T}_a \mid \phi_{k_j} \rangle & \langle \phi_{-k_j} \mid \hat{T}_a \mid \phi_{-k_j} \rangle \end{pmatrix} \cdot \begin{pmatrix} c_{k_j}^+ \\ c_{k_j}^- \end{pmatrix} = e^{\mathbf{i}k_j a} \cdot \begin{pmatrix} c_{k_j}^+ \\ c_{k_j}^- \end{pmatrix} \tag{2.12}$$

that has to be solved.

The Bloch functions satisfy the completeness and the orthogonality relations

$$\sum_{j,i} \mid \psi_{k_j}^{(i)} \rangle \langle \psi_{k_j}^{(i)} \mid = \hat{1} \,, \tag{2.13}$$

$$\langle \psi_{k_j}^{(i)} \mid \psi_{k_{j'}}^{(i')} \rangle = \delta_{ii'} \delta_{jj'} \,. \tag{2.14}$$
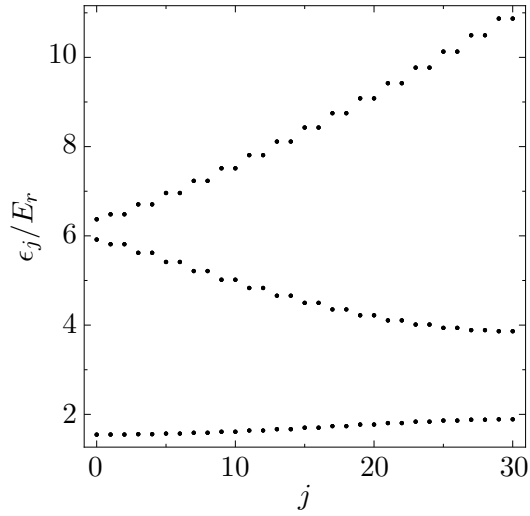
Figure 2.1: Dispersion relation of ^{87}Rb atoms in an optical lattice with $\lambda = 800$ nm and $s = V_0/E_r = 4$ obtained via a diagonalization of the discretized Hamiltonian. The plot shows the first three energy bands of an optical lattice with $I = 31$ minima in the reduced zone scheme.

The index i refers to an energy band and emerges because there is only a finite number of quasi-momenta k_j in a finite volume. However, the set of eigenfunctions of H_x in Equation (2.3) is infinite. In order to fullfill the completeness relation, there must be orthogonal Bloch functions with the same value of k_j. So, the index i refers to the energy band, $u_{k_j}^{(i)}(x)$ in Equation (2.6) is associated to. In the following, we will only consider Bloch functions within the first energy band and therefore drop the index i definitively.

Exemplarily, Figure 2.1 shows the dispersion relation for atomic ^{87}Rb in an optical lattice with a wavelength $\lambda = 800$ nm and a potential depth of four recoil energies. One can clearly see the emergence of band gaps in the eigenvalue spectrum.

An alternative set of orthogonal functions which are localized at individual lattice sites are the so-called Wannier functions [20]. They are defined by the Fourier series of the Bloch functions from the first energy band:

$$w_{\xi_l}(x) = \frac{1}{\sqrt{I}} \sum_{j=0}^{I-1} \psi_{k_j}(x) e^{-\mathbf{i}k_j \xi_l} e^{\mathbf{i}\varphi_{k_j}} . \tag{2.15}$$
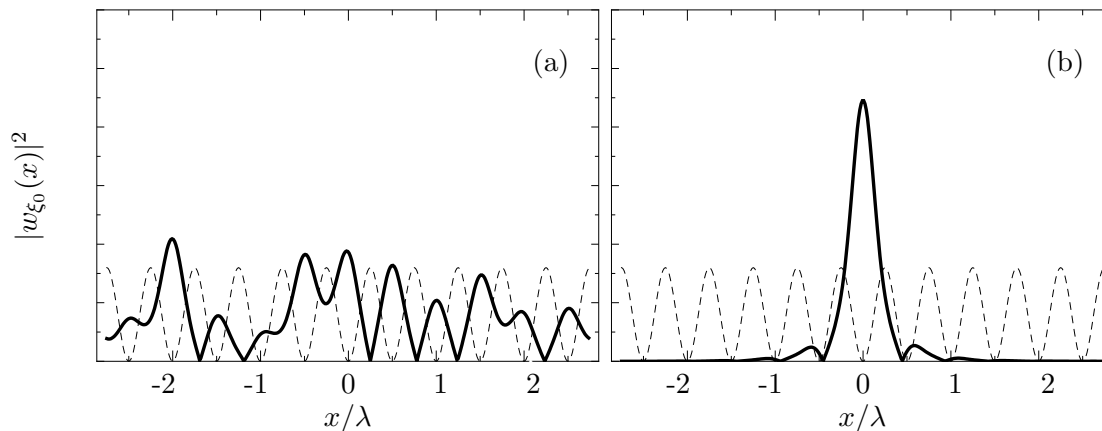
Figure 2.2: (a): probability density of a non-localized Wannier function. (b): probability density of a localized Wannier function. Both for the same set of parameters: $I = 11$, $s = V_0/E_r = 3$, $\lambda = 800$ nm. The dashed line shows the corresponding potential on an arbitrary scale.

The Wannier functions are not unique since we can multiply them by a momentum dependent phase factor φ_{k_j}. For reasons that will be discussed in Section 2.2, the Hubbard model requires the use of strongly localized Wannier functions. In order to obtain maximally localized Wannier functions, one can apply a localization criterion and minimize the spread $\langle x^2 \rangle - \langle x \rangle^2$ [22, 23]. We find a strong localization by choosing the phases φ_{k_j} such that the imaginary part of the Bloch functions vanishes at the same point, arbitrarily chosen to $x = 0$:

$$\mathrm{Im}\{\psi_{k_j}(0) \cdot e^{\mathbf{i}\varphi_{k_j}}\} = 0 \,. \tag{2.16}$$

We illustrate this issue in Figure 2.2. Both panels show Wannier functions $w_{\xi_0}(x)$ which differ only in the choice of the phases φ_{k_j}. In Figure 2.2(a) the Wannier function is delocalized whereas in Figure 2.2(b) the phases are chosen according to Equation (2.16), leading to localization. Note that both Wannier functions are eigenfunctions of the single-particle Hamiltonian (2.3) with the identical energy eigenvalue.

Since we do not have strict mathematical arguments to justify that choosing the phases according to Equation (2.16) leads to maximally localized Wannier functions, we compare the Wannier functions to Gaussian functions that minimize the energy expectation value of the Hamiltonian (2.3). The results are depicted in Figure 2.3. Due to the
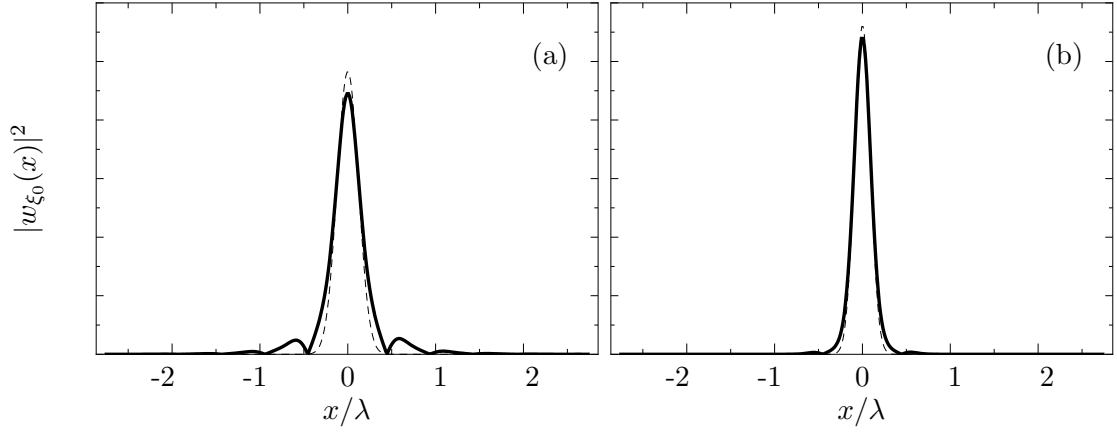
Figure 2.3: Probability density of a localized Wannier function (solid line) versus probability density of a Gaussian function that minimizes the single-particle energy (dashed line). (a): $s = V_0/E_r = 3$, $\langle$ Gauss $\mid w_{\xi_0} \rangle = 0.9858$. (b): $s = V_0/E_r = 10$, $\langle$ Gauss $\mid w_{\xi_0} \rangle = 0.9969$. Both for the parameter set $I = 11$, $\lambda = 800$ nm

"wings", a Wannier function is always broader than the corresponding Gaussian function, but even for shallow optical lattices the overlap of both functions is close to one. Therefore, we conclude that the localized Wannier functions we obtain are close to maximally localized Wannier functions, if not even identical, and provide a valid basis for our calculations of the Hubbard parameters in Section 2.3.

2.2 Bose-Hubbard Model

In 1963, John Hubbard proposed a basic model for the low-temperature physics of electrons in periodic potentials, the Hubbard model [7]. It is based on the assumption that only the lowest Bloch-band is occupied and no excitations to higher-lying energy bands can occur. The two dominant processes are a tunneling of electrons to adjacent potential minima, i.e. lattice sites, and a two-particle on-site interaction. Despite of its simple structure, the bosonic version of the model, the Bose-Hubbard model, exhibits a quantum phase-transition from a superfluid to a Mott-insulating phase [8]. In 1998, Jaksch et al. found out that ultracold atoms in optical lattices could be an experimental realization of the Bose-Hubbard model [24]. This conclusion was the starting point of a very fruitful exchange between experiment and theory, because as we will see later, optical lattices provide perfect experimental control over all relevant parameters of the Bose-Hubbard model. In 2001, Greiner et al. observed the superfluid to Mott-insulator transition in such an experiment [9]. In this section the Bose-Hubbard model is introduced and its validity for the description of ultracold atoms in optical lattices is discussed.

In terms of field operators, which create or annihilate a wave function of a particle in coordinate space, a Hamiltonian including the optical potential $V_{\text{opt}}(\vec{x})$, an optional trapping potential $V_T(\vec{x})$, and a two-particle interaction term $u_{3D}(\vec{x}, \vec{x}')$ has the form:

$$
\begin{aligned}
\hat{H} \;=\; & \int d^3x \; \hat{\Psi}^\dagger(\vec{x}) \left(-\frac{\hbar^2}{2m}\vec{\nabla}^2 + V_{\text{opt}}(\vec{x}) + V_T(\vec{x}) \right) \hat{\Psi}(\vec{x}) \\
& + \frac{1}{2} \int d^3x \int d^3x' \; \hat{\Psi}^\dagger(\vec{x})\, \hat{\Psi}^\dagger(\vec{x}')\, u_{3D}(\vec{x}, \vec{x}')\, \hat{\Psi}(\vec{x}')\hat{\Psi}(\vec{x}) \,.
\end{aligned}
\tag{2.17}
$$

The physical reason for the need of the trapping potential $V_T(\vec{x})$ will be discussed later on. The two-particle interaction is introduced via a contact potential in three dimensions,

$$
u_{3D}(\vec{x}, \vec{x}') = \frac{4\pi a_s \hbar^2}{m}\, \delta^{(3)}(\vec{x} - \vec{x}')\,.
\tag{2.18}
$$

The 1D case follows from the 3D interaction with the assumption that in the two remaining directions interaction is neglected and that the wavefunction can be parameterized with Gaussian functions, i.e., the potential is assumed to be harmonic in these transverse directions with trapping frequencies $\omega_\perp = \omega_y = \omega_z$. Using this, the integrals over the remaining directions can be calculated [25], leading to

$$
u_{1D}(x, x') = 2\,\omega_\perp \hbar\, a_s\, \delta(x - x')\,.
\tag{2.19}
$$

For more details see Appendix A.1. Using this explicit form of the interaction term, we can write down the one-dimensional Hamiltonian:

$$\hat{H} = \int dx\, \hat{\Psi}^\dagger(x) \left(-\frac{\hbar^2}{2m}\frac{\partial^2}{\partial x^2} + V_{\text{opt}}(x) + V_T(x) \right) \hat{\Psi}(x)$$
$$+ \frac{1}{2}\, 2\,\omega_\perp \hbar\, a_s \int dx\, \hat{\Psi}^\dagger(x)\, \hat{\Psi}^\dagger(x)\, \hat{\Psi}(x)\hat{\Psi}(x) . \tag{2.20}$$

In experiments the parameter $\omega_\perp$ has to be chosen large enough in order to guarantee the 1D geometry. A typical value from an experiment is $\omega_\perp = 2\pi\,42\text{kHz}$ [26]. Throughout this work, we use $\omega_\perp = 2\pi\,16\text{kHz}$ unless stated otherwise. With this frequency we are able to reproduce the Hubbard parameters shown in Fig. 5.16 from Ref. [10]. A comparison of the Hubbard parameters resulting from the different values of $\omega_\perp$ is given in Appendix A.4.

The use of a contact interaction in Eq. (2.17) is only valid if the scattering particles are not able to resolve the short-range details of the interaction. In this low-momentum limit the de-Broglie wavelength of a particle is large compared to the short-range structure of the interaction. In this case we can assume that the scattering particle does not resolve any short-range details at all, and use only the lowest order partial wave expansion which is described by the s-wave scattering length a_s. This s-wave scattering length can be interpreted as the radius of a hard sphere which has the same low-momentum scattering properties than the real interaction.

Already Figure 2.3 revealed that Wannier functions are of comparable width, even slightly broader, than the corresponding Gauss functions. Thus, in order to approximate the length scale of the wave function, we adopt the oscillator length b obtained from the quadratic term of a Taylor expansion of the optical potential:

$$b = \sqrt{\frac{\hbar}{m\omega}} = \frac{\lambda}{2\pi}\left(\frac{V_0}{E_r}\right)^{-1/4} . \tag{2.21}$$

For a detailed calculation see Appendix A.2. The ratio between the s-wave scattering length a_s for ^{87}Rb and the oscillator length b is depicted in Figure 2.4(a). Even for very deep optical lattices, i.e., strongly squeezed Gaussian or Wannier functions, the assumption of the contact interaction is still valid since the oscillator length is at least one order of magnitude larger than the scattering length for the parameter regime used in this work.

Localized Wannier functions offer a convenient way to construct the field operators in
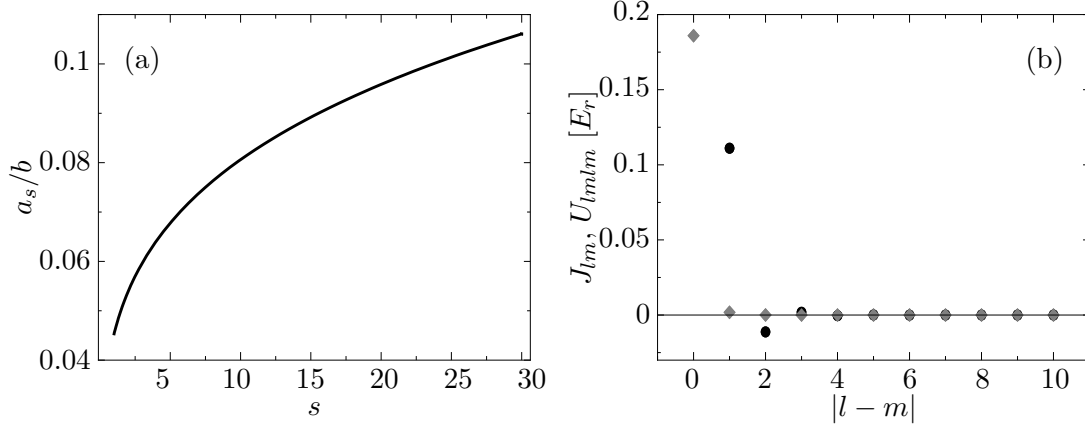
Figure 2.4: (a): The ratio of the scattering length a_s of ^{87}Rb and the oscillator length b with increasing depth of the optical potential $s = V_0/E_r$. (b): The tunneling matrix element J_{lm} (black circles) and the interaction matrix element U_{lmlm} (gray diamonds) with increasing distance, for a_s of ^{87}Rb, $\lambda = 800$ nm, and $s = V_0/E_r = 3$.

Eq. (2.17). We introduce the second quantized creation and annihilation operators $\hat{a}_l^\dagger$ and $\hat{a}_l$ that create or annihilate a localized single-particle Wannier function at site l. For the many-particle basis we use an occupation-number representation

$$\big| \{n_1, n_2, \ldots, n_l, \ldots, n_I\}_\alpha \big\rangle \tag{2.22}$$

where the individual states are denoted by α, and define an I-tuple of occupation numbers n_l for each lattice site l. The operators act on these states according to

$$\hat{a}_l \big| \{n_1, \ldots, n_l, \ldots, n_I\}_\alpha \big\rangle = \sqrt{n_l} \big| \{n_1, \ldots, n_l - 1, \ldots, n_I\}_\alpha \big\rangle, \tag{2.23}$$

$$\hat{a}_l^\dagger \big| \{n_1, \ldots, n_l, \ldots, n_I\}_\alpha \big\rangle = \sqrt{n_l + 1} \big| \{n_1, \ldots, n_l + 1, \ldots, n_I\}_\alpha \big\rangle, \tag{2.24}$$

$$\hat{n}_l \big| \{n_1, \ldots, n_l, \ldots, n_I\}_\alpha \big\rangle = n_l \big| \{n_1, \ldots, n_l, \ldots, n_I\}_\alpha \big\rangle, \tag{2.25}$$

where the occupation number operator is defined as $\hat{n}_l = \hat{a}_l^\dagger \hat{a}_l$. The complete set of occupation-number states, i.e., all possible distributions of the particles in the lattice, span the many-body Hilbert space:

$$\mathcal{H} = \text{span} \left\{ \big| \{n_1, n_2, \ldots, n_I\}_\alpha \big\rangle \right\}. \tag{2.26}$$

Following this notation, the field operators can be expressed by

$$\hat{\Psi}^\dagger(x) = \sum_{l=1}^{I} w^*_{\xi_l}(x)\, \hat{a}_l^\dagger \,, \tag{2.27}$$

$$\hat{\Psi}(x) = \sum_{l=1}^{I} w_{\xi_l}(x)\, \hat{a}_l \,, \tag{2.28}$$

with the Wannier functions $w_{\xi_l}(x)$ defined above. Again, the index $l = 1, \cdots, I$ runs over the individual lattice sites. Using this form of the field operators we can write down the Hamiltonian 2.20 in second quantization with respect to the occupation-number representation:

$$\hat{H} = \sum_{l,m=1}^{I} \int dx\, \hat{a}_l^\dagger w^*_{\xi_l}(x) \left(-\frac{\hbar^2}{2m}\frac{\partial^2}{\partial x^2} + V_{\text{opt}}(x) + V_T(x) \right) \hat{a}_m w_{\xi_m}(x) \tag{2.29}$$

$$+ \frac{1}{2}\, 2\,\omega_\perp \hbar a_s \sum_{\substack{l,m=1\\n,o=1}}^{I} \int dx\, \hat{a}_l^\dagger w^*_{\xi_l}(x)\, \hat{a}_m^\dagger w^*_{\xi_m}(x)\, \hat{a}_n w_{\xi_n}(x)\, \hat{a}_o w_{\xi_o}(x) \,. \tag{2.30}$$

We now introduce a parameterized form of the Hamiltonian where the integral terms are reduced to parameters – the so-called Hubbard parameters.

The first part (2.29) of the Hamiltonian is split into two terms, one with equal indices and one with unequal indices. For $l \neq m$ the integral defines the so-called "tunneling energy" or "Josephson energy"

$$-J_{lm} = \int dx\, w^*_{\xi_l}(x) \left(-\frac{\hbar^2}{2m}\frac{\partial^2}{\partial x^2} + V_{\text{opt}}(x) + V_T(x) \right) w_{\xi_m}(x) \,, \qquad l \neq m \,, \tag{2.31}$$

where the minus sign is convention. In case of equal indices $l = m$ in the integral corresponds to the local single-particle energy:

$$\epsilon_l = \int dx\, w^*_{\xi_l}(x) \left(-\frac{\hbar^2}{2m}\frac{\partial^2}{\partial x^2} + V_{\text{opt}}(x) + V_T(x) \right) w_{\xi_l}(x) \,. \tag{2.32}$$

The interaction term (2.30) of the Hamiltonian is written as

$$U_{lmno} = 2\,\omega_\perp \hbar a_s \int dx\, w^*_{\xi_l}(x)\, w^*_{\xi_m}(x)\, w_{\xi_n}(x)\, w_{\xi_o}(x) \,. \tag{2.33}$$

In the next section we will see that the single-particle matrix elements in Equation

(2.31) almost vanish for $|l - m| > 1$. Furthermore, if we assume localized Wannier functions, all off-diagonal terms in Equation (2.33) vanish as well. These statements will be confirmed explicitly in the next section. Using the Hubbard parameters together with these assumptions finally leads to the form of the Hamiltonian which is called the Hubbard Hamiltonian:

$$\hat{H} = \sum_{l=1}^{I} \left\{ -J_{l,l+1} \left(\hat{a}_l^\dagger \, \hat{a}_{l+1} + \hat{a}_{l+1}^\dagger \, \hat{a}_l \right) \, + \, \epsilon_l \, \hat{n}_l \, + \, \frac{1}{2} \, U_l \, \hat{n}_l (\hat{n}_l - 1) \right\} . \qquad (2.34)$$

2.3   Hubbard Parameters & Bandstructure Calculations

In the previous section we derived the Hubbard Hamiltonian in second quantization (2.34). When phase diagrams are calculated with respect to the Hubbard parameters, one usually assumes constant values for the tunneling energy $J \equiv J_{l,l+1}$ as well as for the interaction energy $U \equiv U_l$. The topology of the optical lattice is then considered approximately by using the on-site potential energy ϵ_l only. This ansatz avoids a consideration of real experimental parameters. We will follow this procedure in Section 3.1. Yet, in order to achieve a closer connection to experiments, we start directly from the optical potentials and calculate the Hubbard parameters explicitly. Thus, a full consideration of all relevant experimental parameters is taken into account. To get started with numerical calculations we have to evaluate the integrals in Eqs. (2.31), (2.32), and (2.33) defining the Hubbard parameters.

If we calculate a set of localized Wannier functions for a given optical potential depth, we are able to confirm the assumption of a vanishing tunneling energy J_{lm} (2.31) for $|l - m| > 1$. Figure 2.4(b) shows the tunneling matrix element as a function of the distance between the two localized Wannier functions for a fixed potential depth $s = V_0/E_r = 3$. Even in this regime, where we will later see that the particles are relatively delocalized, it is clearly visible that only nearest-neighbor tunneling, i.e., $|l - m| = 1$ has a significant contribution to the Hamiltonian, and the next-to-nearest-neighbor tunneling is already negligible. Therefore, the assumption of including only nearest-neighbor tunneling is valid. Note that the tunneling matrix element does not change if it is calculated with the non-localized Wannier function (see Fig. 2.2) since the phases φ_{k_j} in Equation (2.15) cancel when evaluating the integral (2.31) because the Bloch functions are eigenfunctions of the single particle Hamiltonian.

The quantitative behavior of the tunneling energy with increasing lattice amplitude

is depicted in Figure 2.5(a). One can observe an almost exponential decrease with increasing potential depth. For intensities above 15 recoil energies, tunneling is practically absent. There is also an analytic approximation for the tunneling energy which becomes exact in the regime $V_0 \gg E_r$ [25]:

$$J \approx \frac{4}{\pi} E_r \left(\frac{V_0}{E_r}\right)^{3/4} e^{-2\left(\frac{V_0}{E_r}\right)^{1/2}} . \tag{2.35}$$

Numerical values for this approximation are also shown in Figure 2.5(a). For shallow optical lattices the tunneling energy is clearly overestimated by this approximation.

The local single-particle energy ϵ_l defined by Equation (2.32) is equal for all lattice sites in case homogenous lattices and thus amounts to a global energy shift that is usually set to zero. However, in inhomogeneous lattice topologies, which arise in case of superlattices or additional trapping potentials ($V_T(x) \neq 0$), these terms will differ throughout the lattice. A closer inspection of the effect of superlattice potentials will be the subject of the next section.

We have assumed that the interaction part U_{lmno} (2.33) reduces to $l = m = n = o$ if localized Wannier functions are considered. In case of non-localized Wannier functions this is of course not the case. By taking a look at Figure 2.2(a) it is obvious that off-diagonal parts of the sums in Eq. (2.33) may contribute, whereas for the localized function shown in Figure 2.2(b) the off-diagonal parts are small. For illustration, the matrix elements $U_{lmlm} = 2\omega_\perp \hbar a_s \int dx \, |w_{\xi_l}(x)|^2 \cdot |w_{\xi_m}(x)|^2$ are shown in Figure 2.4(b). They are practically zero for $|l - m| > 0$. Hence, it is justified to consider the diagonal term $|l = m|$ only.

Increasing the optical potential s leads to a squeezing of the Wannier function and the integral over the fourth power of the function increases. Quantitatively this can be seen in Figure 2.5(a). With the parameterization of the Wannier function by a Gaussian function one can derive an approximate analytic expression for the interaction term:

$$U \approx 2\omega_\perp \hbar \frac{a_s}{\lambda} \left(4\pi^2 \frac{V_0}{E_r}\right)^{1/4} . \tag{2.36}$$

For details see Appendix A.2. Figure 2.5(a) reveals that the reduced width of the Gaussian compared to the Wannier function (see Fig. 2.3) leads to a systematic overestimation of the two-particle interaction energy by this approximation.
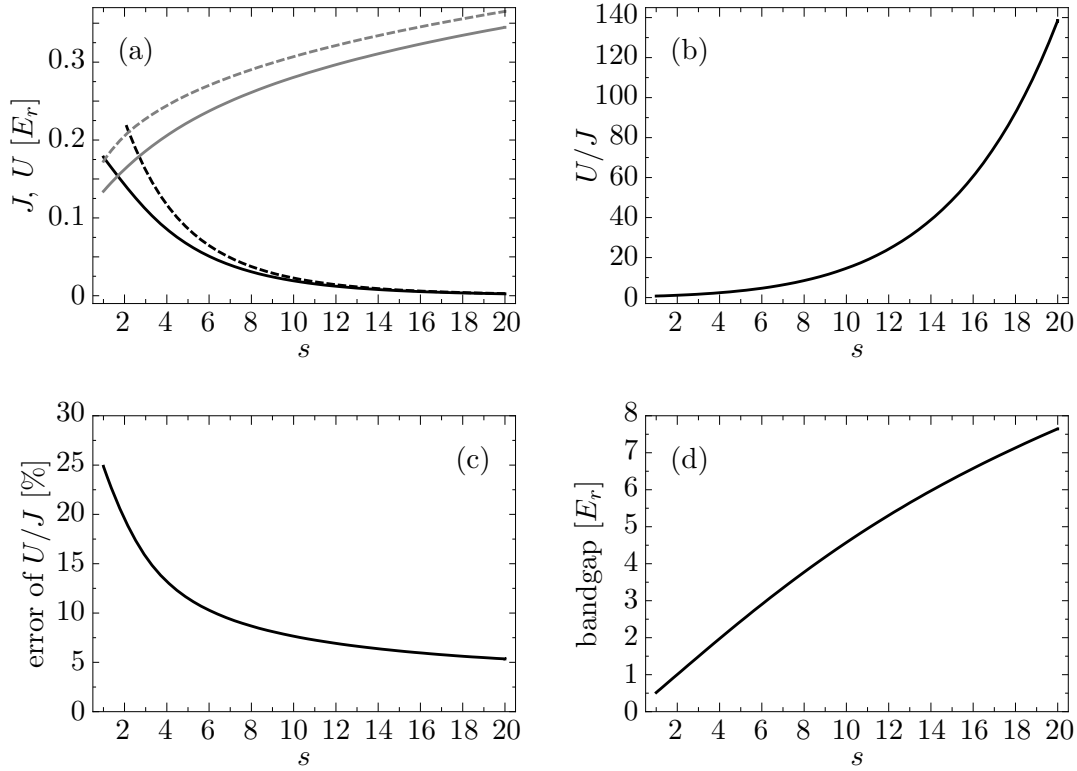
Figure 2.5: (a): Hubbard parameters J (black) and U (gray) as a function of the depth of the optical potential s=V_0/E_r. Solid lines are our calculations [Eqs. (2.31) and (2.33)], dashed lines are analytical approximations [Eqs. (2.35) and (2.36)]. (b): U/J as a function of the potential depth ($s = V_0/E_r$). (c): Relative error of the analytical approximations of U/J. (d): Energy gap between lowest band and first excited band.

If no inhomogeneity is present, i.e. the optical lattice is translationally invariant, the physics of the Bose-Hubbard model is completely characterized by the ratio of the two parameters U and J. Figure 2.5(c) shows the relative error if the approximated values for J and U are used. Even at rather large optical potential depth, i.e. large values of s, the relative error is above 5%. In the regime of smaller optical potential depth the approximations of the Hubbard parameters [Eqs. (2.35) and (2.36)] are rather crude.

2.4   Limits of the Model

In our motivation of the Bose-Hubbard model we assumed a single-band approximation, i.e., only states from the lowest energy band in Figure 2.1 are considered. Comparing the tunneling energy with the energy of the band gap [Figs. 2.5(a) and 2.5(d)] one can see that the tunneling energy is always smaller than the bandgap. However, for very shallow lattices, e.g. $s = 2$ and $U \approx 0.15\,E_r$, the on-site interaction of four particles on a lattice site is $4(4-1)/2 \cdot U \approx 0.9\,E_r$, which is close to the bandgap of about $1\,E_r$. Thus, the validity of the single-band approximation has to be carefully checked in the weakly interacting regime. Since this work focuses on the intermediate and strong interaction regime ($s > 5$), where the bandgap is much larger and occupation-number states with many particles at one site are practically irrelevant, the single-band approximation is sufficient.

Another important issue is our limitation to non-thermal excitations. In the single-particle picture this means we have to assure not to overcome the bandgap because this would violate our restriction to the lowest Bloch band. In order to roughly set a scale for the temperature, we employ Boltzmann's constant to express the recoil energy in terms of a temperature, obtaining $E_r/k_B \approx 10^{-7}$K. Since all relevant energies in the Bose-Hubbard model are smaller than $1\,E_r$ as shown in figure 2.5(a), experiments in the sub-μK regime should be well approximated by the single-band assumption.

A rather subtle approximation of this ansatz is the restriction to a single-particle model for the band-structure calculations. Hence, we assume that a multiple occupation of a lattice site does not change the shape of the Wannier function. Yet, already a double occupation of a lattice site would broaden the Wannier function due to the competition between the repulsive interaction and the lattice potential. This would not only lead to a smaller interaction energy, but also to a larger tunneling energy. However, it was found that sizable changes of the Hubbard parameters in one-dimensional lattices only occur for occupation numbers $n_l > 10$ and optical potential depth $V_0 > 20 E_r$ [27]. Both values are much larger than those used in this work, and thus the single-particle ansatz for the band-structure calculations is valid.

2.5   Two-Color Superlattice Potential

In Section 2.1 we have discussed the single-particle physics of cold atoms in a strictly periodic optical lattice generated by a monochromatic standing-wave laser-field. A sec-
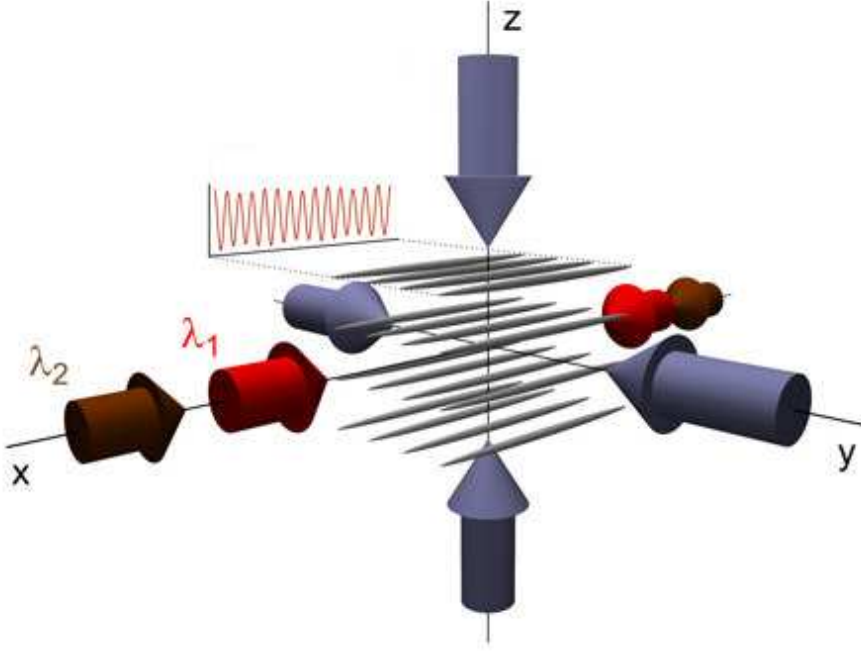
Figure 2.6: Illustration of the experimental laser setup. Two laser beams with large intensities in y- and z-direction provide an array of cigar-shaped tubes among which tunneling is almost completely suppressed. One laser beam in x-direction (λ_2) forms the primary 1D optical lattice, the other weaker one (λ_1) with a different wavelength imprints a spatial modulation. The resulting potential inside each of the tubes is depicted in Figure 2.7. The picture is taken from [26].

ond, orthogonal polarized laser with a different wavelength can be used to introduce additional complexity and form a two-color superlattice potential. In addition we allow for a longitudinal trapping potential $V_T(x) = 1/2 m \omega_x^2 x^2$ which represents the potential gradient due to the Gaussian shape of the laser focus and a magnetic trapping potential:

$$V_{\text{opt}}(x) = \underbrace{s_1 E_{r_1} \sin^2\left(\frac{2\pi}{\lambda_1}x + \phi\right)}_{V_1} + \underbrace{s_2 E_{r_2} \sin^2\left(\frac{2\pi}{\lambda_2}x\right)}_{V_2} + \frac{m\omega_x^2}{2}x^2 \,, \qquad (2.37)$$

where s_i, λ_i, and E_{r_i} are the optical potential depth, wavelength, and recoil energies of the two lasers which have a phase shift ϕ. In the following the stronger, primary laser is always defined by s_2 and λ_2. The experimental laser setup is illustrated in Figure 2.6 and the resulting one-dimensional optical potential with a typical parameter set used in experiment is depicted in Figure 2.7.

As explained in the previous section, the determination of the Hubbard parameters
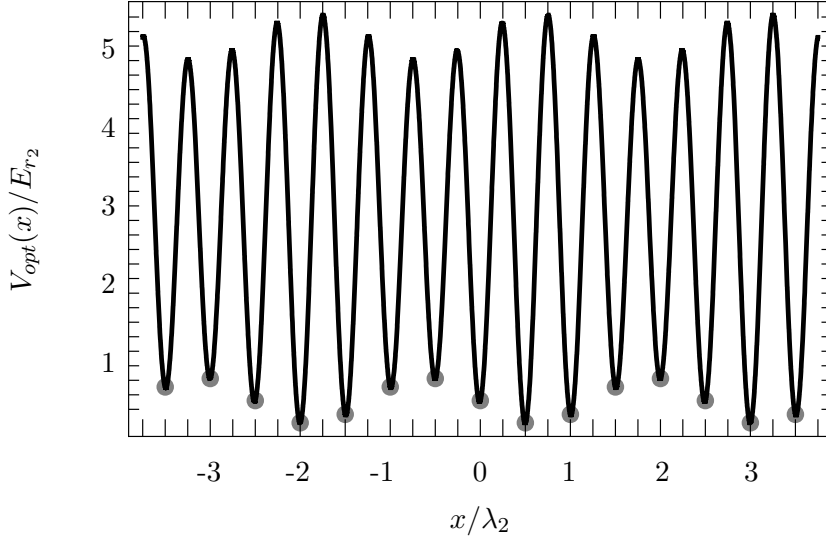
Figure 2.7: Two-color superlattice potential with $\lambda_2 = 800$ nm, $\lambda_1 = 1000$ nm, $\phi = \pi/4$, $s_2 = 5$, $s_1 = 1$, and $\omega_x = 0$. The gray dots show the location of the discrete lattice sites in the Hubbard model.

is based on a band-structure calculation from which the localized Wannier functions are obtained. However, in an inhomogeneous, non-periodic potential a band structure calculation is not straightforward. In order to extract site-dependent Hubbard parameters we are therefore limited to an approximate scheme to obtain localized Wannier functions for the superlattice geometry. We have used two different approaches to calculate the site-dependent Hubbard parameters, which will be discussed in the following paragraphs.

As a simple ansatz, we consider the weak laser field and the harmonic potential as a perturbation of the strong primary laser ($s_1 E_{r_1} \ll s_2 E_{r_2}$ and $1/2 m\omega_x^2 x^2 \ll s_2 E_{r_2}$) and the Wannier functions are extracted from a conventional band-structure calculation for the homogeneous lattice defined by the primary laser alone. In this approximation, the Wannier functions are identical for each lattice site. Using these Wannier functions, the Hubbard parameters of each site of the superlattice are computed using Eqs. (2.31), (2.32), and (2.33) and the full superlattice potential. The site-dependence of the parameters then only results from the superlattice potential $V_{\mathrm{opt}}(x)$ entering into the matrix elements and not from a site-dependence of the Wannier functions themselves. As a result, the parameter U_l characterizing the on-site interaction remains constant for all

lattice sites.

We also employed a more sophisticated ansatz. Here, the site-dependent Wannier functions are determined individually for each site of the inhomogeneous lattice using a standard band-structure calculation for a periodic lattice whose lattice amplitude is given by the local depth of the inhomogeneous potential at that particular site. In this way, the shape of the Wannier functions depends non-trivially on the local structure of the superlattice potential. The only reason why a set of Wannier functions determined in this way cannot be considered as an exact set of localized basis functions results from the minimal violation of the orthogonality of Wannier functions for neighboring sites. Their mutual overlap is non-zero but always below 1% in the parameter regime considered in all our calculations. Using these individual localized Wannier functions, all site-dependent Hubbard parameters are computed without further approximations.

The comparison of the site-dependent Hubbard parameters U_l, ϵ_l, and $J_{l,l+1}$ obtained in the two schemes exhibits very little difference, as shown in Figure 2.8. From this, we conclude that the second scheme provides a sufficiently accurate description of the Hubbard parameters in the parameter range under consideration, simply because the deviation from the first, much cruder approximation is small. Furthermore, the dominant effects introduced by the superlattice geometry are covered by the local on-site potential energy ϵ_l, which is practically independent of the choice of the method.

In this work we consider two different optical lattices. One with $\lambda_2 = 800$ nm, $\lambda_1 = 1000$ nm, $\phi = \pi/4$ which was used in previous studies of our group [15, 38] and a second setting motivated by experiments [29, 26] with $\lambda_2 = 830$ nm, $\lambda_1 = 1076$ nm, and $\phi = \pi/3$. Examples for the site-dependent Hubbard parameters for the commensurate as well as the incommensurate superlattice are depicted in Figure 2.9. Note that we always subtract a global constant from the Hamiltonian such that $\epsilon_{\min} = \min\{\epsilon_l\} = 0$. The dominant effect of the superlattice structure is the spatial modulation of the on-site energies ϵ_l, which is in-line with the approximation to introduce the superlattice through ϵ_l only. However, also the tunneling matrix element $J_{l,l+1}$, which essentially depends on the barrier height between the sites l and $l+1$, shows a sizable variation of $\pm 20\%$ around the average value $\bar{J}$. The interaction strength U_l shows only a weak site-dependence which is induced solely through the site-dependence of the Wannier functions. A comparison of the energy scales reveals that the weak secondary laser with $s_1 = s_2/10$ considered in this example is sufficient to create a superlattice with $\epsilon_{\max} > \bar{U}$.
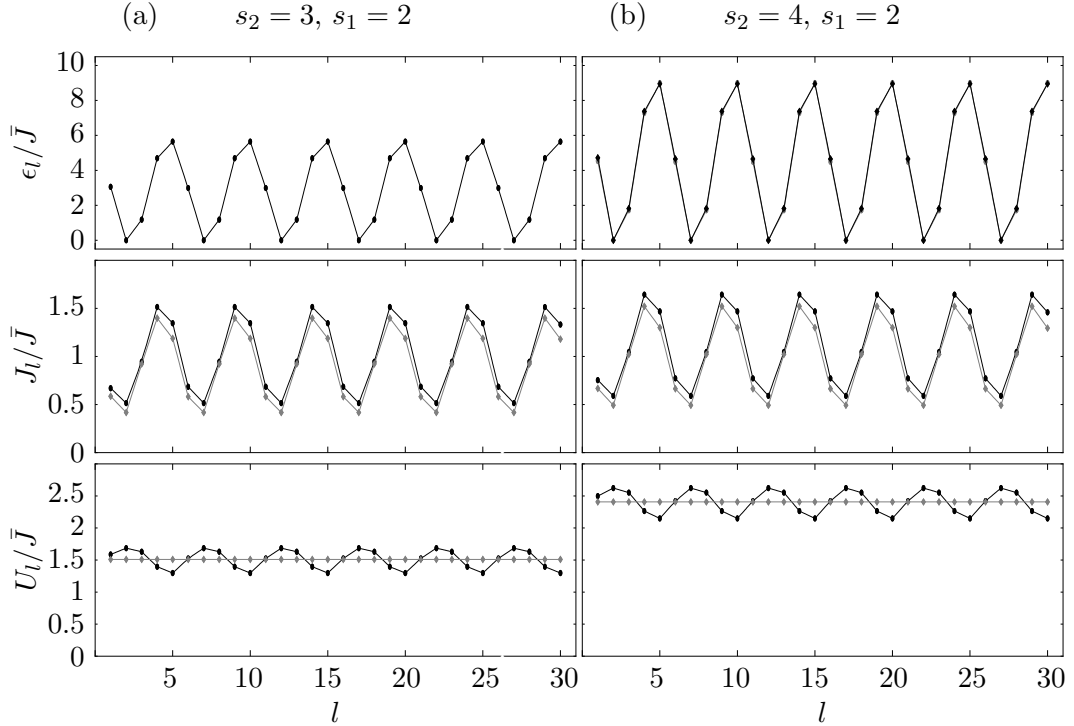
Figure 2.8: Site-dependent Hubbard parameters for the commensurate lattice calculated with individual Wannier functions (black symbols) and as a perturbation (gray symbols). Column (a): $s_2 = 3$, $s_1 = 2$, column (b): $s_2 = 4$, $s_1 = 2$ In both cases the parameters are: $\lambda_2 = 800$ nm, $\lambda_1 = 1000$ nm, $\omega_\perp = 30 E_{r_2}/(2\pi\hbar)$ and $a_s = 109\,a_{\text{Bohr}}$. Lines to guide the eye.

In order to point out the strength of the Hubbard parameters in the whole parameter region under consideration, we plot their mean values in the (s_2,s_1)-plane. Figure 2.10(a) shows the mean tunneling parameter in units of the recoil energy $\bar{J}/E_{r_2}$. One can see an exponential-like decrease with increasing s_2 almost independent of s_1. However, the contour lines are not straight lines along the s_1 direction but show a slight increase of the mean tunneling with increasing s_1. This is due to the enhanced tunneling between certain sites where the potential barriers are reduced by the superlattice topology. The complement effect can be seen for the mean interaction $\bar{U}/\bar{J}$ in Figure 2.10(b). It increases with increasing s_2 but now the contour lines bend in direction of increasing $\bar{U}/\bar{J}$. The mean on-site energies are shown in Figure 2.10(c) and exhibit an increase with increasing s_2 and s_1. For that reason we are not able to find a region for small values of s_2 where this parameter dominates over the interaction. This will result in a
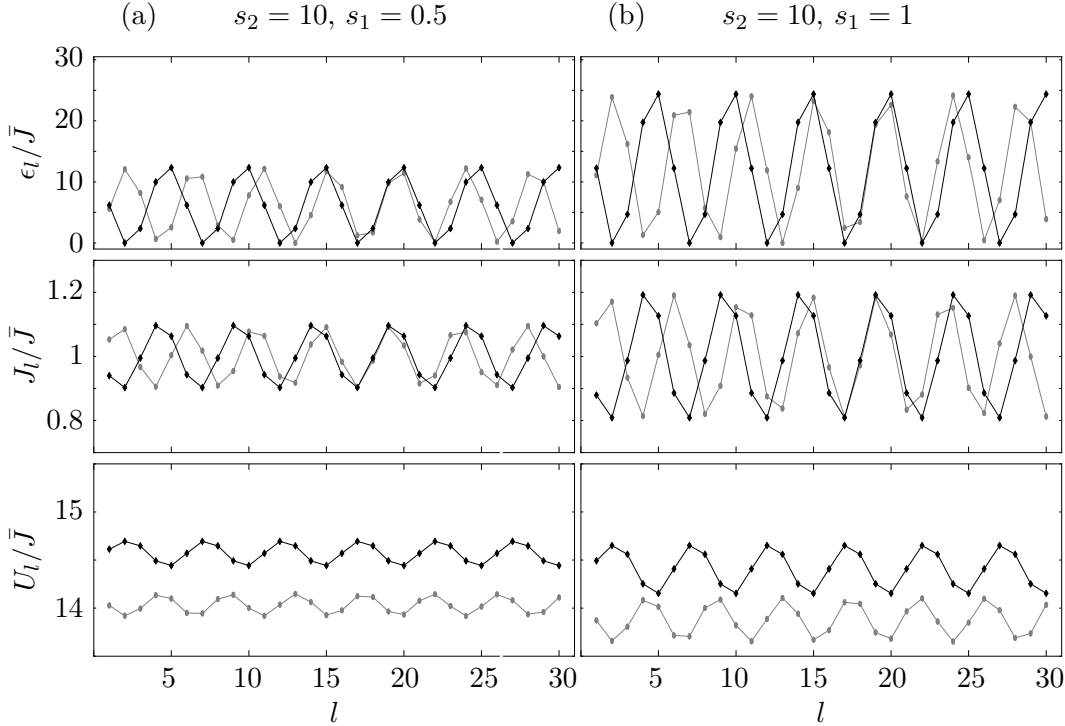
Figure 2.9: Site-dependent Hubbard parameters for the commensurate lattice $\lambda_1 = 800$ nm, $\lambda_2 = 1000$ nm, (black) and the incommensurate lattice $\lambda_1 = 830$ nm, $\lambda_2 = 1076$ nm (gray). Column (a): $s_2 = 10$, $s_1 = 0.5$, column (b): $s_2 = 10$, $s_1 = 1$. In both cases the transverse trapping frequency is $\omega_\perp = 30 E_{r_2}/(2\pi\hbar)$ and the scattering length $a_s = 109\, a_{\mathrm{Bohr}}$. Lines to guide the eye.

different structure of the phase diagrams spanned in the $(U/J,\epsilon_{\max}/J)$-plane compared to the phase diagrams spanned with respect to the (s_2,s_1)-plane. We will discussed this together with the phase diagrams in Section 5.4.

2.6   Harmonic Trapping Potential

Another source for inhomogeneities in the optical potential, apart from a second laser beam, are the additional magnetic trap, which used to confine the atoms [58], and the Gaussian beam profile of the primary laser [21]. In case of a red-detuned laser, with respect to the atomic resonance of ^{87}Rb, both potentials increase with increasing distance from the center of the trap. We account for this by introducing an additional a harmonic potential with frequency ω_x in the optical potential (2.37). Typical experimental fre-
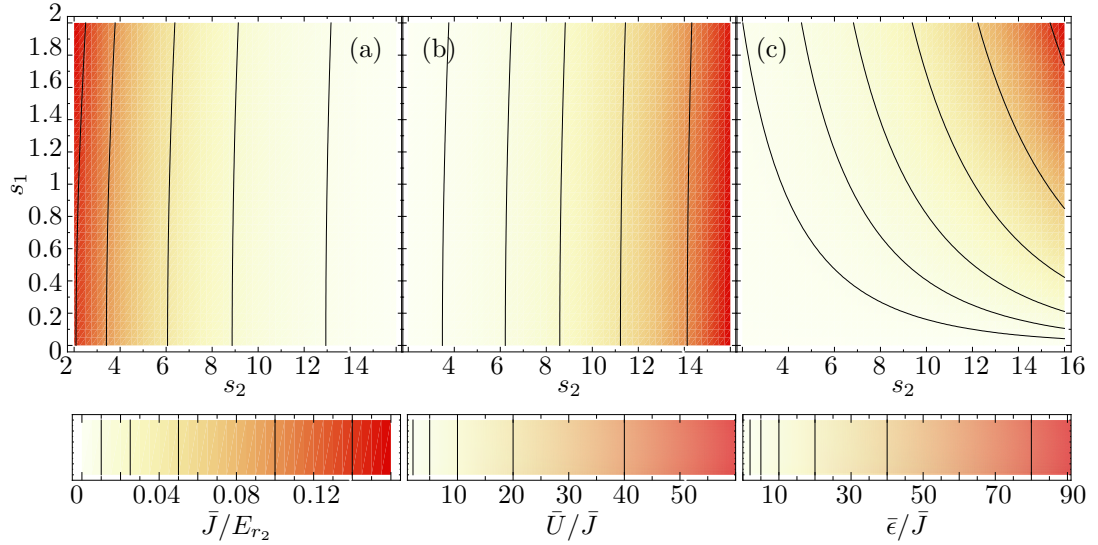
Figure 2.10: Density plot of the site-dependent Hubbard parameters for the commensurate lattice $\lambda_2 = 800$ nm, $\lambda_1 = 1000$ nm in the s_2-s_1 plane. Each point represents the maximum value of the parameters across the optical lattice. The transverse trapping frequency is $\omega_\perp = 30 E_{r_2}/(2\pi\hbar)$, $\omega_x = 0$, and the scattering length $a_s = 109\, a_{\text{Bohr}}$.

quencies range from $\omega_x = 2\pi\, 8.7$ Hz to $\omega_x = 2\pi\, 75$ Hz [10, 29, 26]. To get an impression of the energy scale, we show some values for the Hubbard parameters in Table 2.1, which are obtained through our band-structure approach. By setting $s_1 = 0$ the on-site the variation of the on-site energies results solely from the additional harmonic potential. At the outer rims they are given by $\epsilon_{\max}$. For trapping frequencies below $2\pi\, 25$Hz we do not expect a crucial impact because the resulting local potential energies ϵ_l are very small in comparison to U_l and J_l. However, for the larger frequency this changes dramatically. The energy scales of U_l and ϵ_l become comparable for $\omega_x = 2\pi\, 50$ Hz to $\omega_x = 2\pi\, 75$ Hz. In case of $\omega_x = 2\pi\, 100$ Hz the on-site energies clearly dominate the energy scale. A detailed discussion on the impact of ω_x will be provided together with the discussion of the phase diagrams in Section 5.4.

2.7   Observables

In the following we will introduce the observables we use to characterize the different phases of the atoms in the optical lattice [15].

s_2	2	10	12	16
$\bar{J}/E_{r_2}$	0.1428	0.0192	0.0123	0.0053
$\bar{U}/E_{r_2}$	0.1624	0.2505	0.2966	0.3232
$\bar{U}/\bar{J}$	1.1378	14.623	24.222	60.636
$\omega_x = 2\pi\,25$ Hz				
$\epsilon_{\max}/E_{r_2}$	0.02431	0.02431	0.02431	0.02431
$\epsilon_{\max}/\bar{J}$	0.17052	1.26739	1.98446	4.55600
$\omega_x = 2\pi\,50$ Hz				
$\epsilon_{\max}/E_{r_2}$	0.09737	0.09737	0.09737	0.09737
$\epsilon_{\max}/\bar{J}$	0.68196	5.06927	7.937412	18.2389
$\omega_x = 2\pi\,75$ Hz				
$\epsilon_{\max}/E_{r_2}$	0.21909	0.21909	0.21909	0.21909
$\epsilon_{\max}/\bar{J}$	1.53407	11.4048	17.8576	41.0344
$\omega_x = 2\pi\,100$ Hz				
$\epsilon_{\max}/E_{r_2}$	0.38950	0.38950	0.38950	0.38950
$\epsilon_{\max}/\bar{J}$	2.72634	20.27242	31.7430	72.9423

Table 2.1: Hubbard parameters for the commensurate setup ($\lambda_2 = 800$ nm, $\lambda_1 = 1000$ nm, $\phi = \pi/4$, $I = 30$) and the parameters for ^{87}Rb. For the sake of simplicity we set $s_1 = 0$, therefore $\epsilon_{\max}$ is the on-site energy at the boundaries (lattice sites 1 and 30) resulting from the additional harmonic potential.

Let us assume a many-body state can be written as a superposition of all possible occupation number-states (see Eq. 2.26). The dimension of the Hilbert space shall be D. The ν-th eigenstate of the Hubbard Hamiltonian for N particles and I lattice sites is defined by the coefficients $C_\alpha^{(\nu)}$ obtained by a numerical solution of the eigenvalue problem:

$$\big|\,\psi^{(\nu)}\,\big\rangle = \sum_{\alpha=1}^{D} C_\alpha^{(\nu)} \big|\,\{n_1, n_2, \ldots, n_I\}_\alpha\,\big\rangle \quad \text{with} \quad \sum_{l=1}^{I} n_l = N\,. \tag{2.38}$$

Since we are mostly interested in groundstate properties, the index ν is usually dropped if not referring to an excited state.

2.7.1   Mean Occupation-Number

The mean occupation-number at lattice site l is defined by

$$n_l = \big\langle\,\psi\,\big|\,\hat{n}_l\,\big|\,\psi\,\big\rangle\,. \tag{2.39}$$

In a homogenous optical lattice with periodic boundary conditions the mean occupation-numbers are the same for all sites and are given by the filling fraction N/I. In inhomogeneous systems the mean occupation-number can be utilized to probe the distribution of particles due to the potential generated by the optical superlattice and a harmonic confinement.

2.7.2   Number Fluctuation

The number fluctuation defined by

$$\sigma_l^2 = \big\langle\,\psi\,\big|\,\hat{n}_l^2\,\big|\,\psi\,\big\rangle - \big\langle\,\psi\,\big|\,\hat{n}_l\,\big|\,\psi\,\big\rangle^2\,, \tag{2.40}$$

provides insight to the mobility of the particles within the optical lattice. Whenever the mean occupation number at a particular site originates from a superposition of many occupation-number states with different occupation numbers, particles have at least locally a large mobility. The mobility is small if the main contribution to the mean occupation number comes from a single occupation-number state or a subset of states with the same occupation number at the particular site.

2.7.3   Condensate Fraction

An interesting question is whether the cloud of atoms on the optical lattice is a Bose-Einstein condensate or not. By definition, a Bose-Einstein condensate is present if most

of the particles share the same, usually the energetically lowest, single-particle state. The condensate fraction f_c is the ratio of condensed particles N_c to all particles N

$$f_c = \frac{N_c}{N} \,.$$
(2.41)

In order to obtain this quantity from a many-body state we follow the Onsager-Penrose criterion [20, 30] and calculate the so-called natural orbitals which correspond to Bloch functions for a homogenous lattice with periodic boundary conditions. If one of those natural orbitals is macroscopically occupied, the system under consideration is condensed to a certain single-particle state. If this is the single-particle state with the lowest energy, this condensate is called a Bose-Einstein condensate.

Technically we have to solve the eigenvalue problem of the one-body density-matrix defined by the matrix elements

$$\rho_{ll'}^{(1)} = \left\langle \, \psi \, \middle| \, \hat{a}_l^\dagger \hat{a}_{l'} \, \middle| \, \psi \, \right\rangle \,.$$
(2.42)

For homogeneous systems the eigenvalues λ_i are just the quasi-momentum occupation numbers. The largest eigenvalue defines the number of condensed particles N_c.

In the non-interacting limit, the Hubbard Hamiltonian is diagonal in momentum space and all particles occupy the zero quasi-momentum single-particle state. Thus, the condensate fraction becomes one in that case.

$$f_c = 1 \qquad \text{for} \qquad U \to 0 \quad \text{or} \quad J \to \infty$$
(2.43)

On the other hand, if all quasi-momentum single-particle states are equally occupied, the condensate fraction becomes zero in an infinite system. This would be the case for a spin-polarized and completely filled Fermi system, or for boson system with commensurable filling in the limit $U \to \infty$ or $J \to 0$.

Since the trace of the one-body density matrix is the sum of I diagonal elements and equals the total number of particles N, the length of the lattice I sets a lower bound for the condenstate fraction $f_c \geq 1/I$. This means that the condensate fraction might suffer from strong finite size effects.

For completeness we note that the occurrence of macroscopically occupied natural orbitals goes along with off-diagonal long-range order [31]. Formally this is the case if the

off-diagonal matrix-elements of the one-body density-matrix remain finite even for large distances

$$\rho_{ll'}^{(1)} \neq 0 \quad \text{for} \quad |l - l'| \to \infty \,. \tag{2.44}$$

This statement has to be handled with care in finite systems. There, the off-diagonal elements will only be exactly zero for vanishing tunneling $J \to 0$ or infinite interaction strength $U \to \infty$. In a perfect Bose-Einstein condensate all elements of the one-body density-matrix equal one because all particles are maximally delocalized. One can also regard equation (2.42) as the overlap between a state, where a particle is moved from site l to l' with the original state. In this sense, off-diagonal long-range order reflects the order of delocalization of particles in the lattice.

2.7.4   Interference Pattern and Fringe Visibility

The interference pattern and the fringe visibility are of particular interest as they are directly accessible to experiments, where one applies time-of-flight (TOF) imaging to probe the initial state of the atoms in the optical lattice. This is achieved by instantaneously switching off the lasers and the confining potentials. After a certain time of free expansion of the gas cloud in the gravitational field it is irradiated with resonant laser light and the absorption image is taken with a CCD camera. During the expansion the quasi-momentum structure imposed by the optical lattice is mapped to a spatial density distribution. If particles at different lattice sites are phase-coherent, the density distribution of the expanded cloud will exhibit interference patterns. If not, the image will show an incoherent superposition of the momentum distribution of the atoms from the individual lattice sites.

By formally introducing an amplitude operator $\hat{A}(x)$, the intensity of the matter wave $\mathcal{I}(x)$ at a point x is given by

$$\mathcal{I}(x) = \left\langle \, \psi \, \middle| \, \hat{A}^{\dagger}(x) \, \hat{A}(x) \, \middle| \, \psi \, \right\rangle. \tag{2.45}$$

Neglecting the spatial envelope of the interference pattern, the amplitude operator $\hat{A}(x)$ depends on the phase difference $\phi_l(x)$ between site l and the observation point x only,

$$\hat{A}(x) = \frac{1}{\sqrt{I}} \sum_{l=1}^{I} e^{\mathbf{i}\,\phi_l(x)} \, \hat{a}_l \,. \tag{2.46}$$

Considering microscopic distances between the lattice sites and a macroscopic distance from the lattice to the observation point, we assume a constant phase shift between

adjacent sites $\delta = \phi_{l+1}(x) - \phi_l(x)$. Using this far-field limit leads to the following expression for the matter-wave interference pattern:

$$\mathcal{I}(\delta) = \frac{1}{I} \sum_{l,l'=1}^{I} e^{\mathbf{i}(l-l')\delta} \left\langle \psi \mid \hat{a}_{l'}^{\dagger} \hat{a}_l \mid \psi \right\rangle = \frac{1}{I} \sum_{l,l'=1}^{I} e^{\mathbf{i}(l-l')\delta} \, \rho_{ll'}^{(1)} \,, \tag{2.47}$$

in which we have used the definition (2.42). This expression is closely related to the quasi-momentum distribution. If δ equals the possible quasi-momenta $q_k = 2\pi k/I$, $\quad k = 0, 1, \ldots, I-1$, we obtain the respective quasi-momentum occupation numbers. Note that in a homogeneous lattice the condensate wave function—the lowest natural orbital—is associated with the Bloch function with zero quasi-momentum. In this case, the fraction of the intensity of the central peak $\mathcal{I}(0)$ and the total intensity would also yield the condensate fraction f_c.

The visibility ν of the interfence fringes can be derived directly from the interference pattern via

$$\nu = \frac{\max\left\{\mathcal{I}(x)\right\} - \min\left\{\mathcal{I}(x)\right\}}{\max\left\{\mathcal{I}(x)\right\} + \min\left\{\mathcal{I}(x)\right\}} \,. \tag{2.48}$$

This is basically the intensity difference between the first order interference peaks and the incoherent background. A nice feature of this observable is that the discarded spatial envelope does not play a role here. For vanishing interaction energy all particles occupy the lowest natural orbital. Therefore, the incoherent background will vanish completely and the visibility of the interference fringes becomes one in this limit.

2.7.5 Energy Gap

Measuring the excitation spectrum of the atomic cloud provides also a sensitive tool to probe for different quantum phases. In the experiment one employs two-photon Bragg spectroscopy via an intensity modulation of the optical lattice. The width of the central interference peak is used as a measure of the energy transfer into the atomic cloud [10]. The detailed structure of the excitation spectrum has been also investigated theoretically by our group [32, 33].

A first qualitative information about these spectra is given by the energy gap ΔE. This is the difference between the energy of the first excited state and the ground state

$$\Delta E = E^{(1)} - E^{(0)} \,. \tag{2.49}$$

Basically this is the minimal amount of energy needed to excite the system. In the Mott-insulating phase of a homogeneous lattice the occupation-number state with one particle per site dominates the ground state. For a double occupancy of a single lattice site, the system has to pay the interaction energy. Since this is the minimal possible excitation, the energy gap becomes proportional to the interaction strength between two particles in the Mott-insulating phase. In the superfluid phase already the ground state is a superposition of many occupation-number states. Because a multi occupancy of a single lattice site is not associated with an energy increase, the energy gap is small and even zero in the limit of vanishing interaction energy.

2.7.6 Maximum Coefficient

Although the maximum coefficient

$$C_{\mathrm{max}}^2 = \max\left\{ C_\alpha^2 \right\} \tag{2.50}$$

in the occupation-number representation (2.38) is not an observable in the strict sense, it provides interesting information about the structure of the state. If many different occupation-number states contribute its value is small, whereas its value is close to one if there is a dominant occupation-number state.

Chapter 3

Diagonalization Techniques

3.1 Diagonalization in the Complete Hilbert Space

A straightforward approach to obtain non-trivial solutions for the Hubbard model at $U \neq 0$ and $J \neq 0$ is an exact diagonalization within a complete Hilbert space. If applicable, this is also the best method, since it is relatively easy to implement and, more importantly, we obtain the exact ground state from which all observables can be directly calculated. However, this method is restricted to small lattices of about 10 sites and 10 particles due to the factorial growth of the Hilbert space dimension.

3.1.1 Bosons in a Two-Color Superlattice

Together with the occupation-number representation (2.26), the Schrödinger equation for the Bose-Hubbard Hamiltonian

$$\hat{H} = \sum_{l=1}^{I} \left\{ -J \left(\hat{a}_l^{\dagger} \, \hat{a}_{l+1} + \hat{a}_{l+1}^{\dagger} \, \hat{a}_l \right) + \epsilon_l \, \hat{n}_l + \frac{1}{2} \, U \, \hat{n}_l(\hat{n}_l - 1) \right\}. \qquad (3.1)$$

with N particles and I lattice sites defines the matrix eigenvalue problem:

$$\sum_{\alpha=1}^{D} \left\langle \, \{n_1, n_2, \ldots, n_I\}_\beta \, \middle| \, \hat{H} \, \middle| \, \{n_1, n_2, \ldots, n_I\}_\alpha \, \right\rangle C_\alpha^{(\nu)} = E_\nu C_\beta^{(\nu)}. \qquad (3.2)$$

The dimension D of the Hilbert space grows factorially with the lattice size and the number of particles. By combinatorics we obtain the dimensions

$$D_a = \frac{(N + I - 1)!}{N!(I - 1)!} \quad \text{for bosons ,} \tag{3.3}$$

$$D_c = \frac{I!}{N!(I - N)!} \quad \text{for fermions .} \tag{3.4}$$

For $I = N = 8$, the dimension for the bosonic Hilbert space is $D_a = 6435$, but for $I = N = 12$ one already has $D_a = 1352078$. The latter can still be solved on an ordinary desktop computer if the sparseness of the Hamilton matrix is exploited. In this case Lanczos algorithms [34] are applied in order to calculate a few eigenstates from the lower end of the spectrum. However, going to larger lattices with more particles quickly becomes impracticable in this framework.

Usually, the Hubbard Hamiltonian is expressed in units of the tunneling energy J. Thus, the phase diagram is spanned by the dimensionless parameters U/J and $\epsilon_{\max}/J$ introduced in Chapter 2. A detailed analysis of the Bose-Hubbard model for moderate system sizes using an exact diagonalization in the complete Hilbert space can be found in references [15, 16].

An exemplary phase diagram for the superlattice topology depicted in Figure 3.1 was already shown in the introduction in Figure 1.4. Four different phases were identified: the superfluid phase in the regime of small U/J and small $\epsilon_{\max}/J$, the Mott-insulating phase at $5 \lesssim \epsilon_{\max}/J < U/J$, the quasi Bose-glass phase at $5 \lesssim U/J < \epsilon_{\max}/J$, and the localized phase at very small U/J and large $\epsilon_{\max}/J$. The characteristics of the different phases will be discussed in detail in Section 5.4.

3.1.2 *Boson-Fermion Mixture in a Two-Color Superlattice*

Recent developments in the sympathetic cooling of boson-fermion mixtures in optical lattices [35] paved the way to experimental studies of degenerate gases with mixed quantum statistics [36, 37]. Various aspects of boson-fermion mixtures in uniform lattices have been investigated theoretically [38, 39]. In this section, we study the effect of an additional superlattice potential on the phase diagram of such a mixture. All the following results from this chapter were published [40].

The Hamiltonian of a binary boson-fermion mixture in an optical lattice is given by
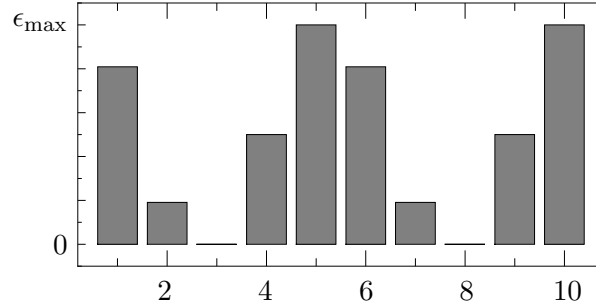
Figure 3.1: Topology of the two-color superlattice.

a straightforward generalization of the Bose-Hubbard Hamiltonian:

$$\hat{H} = \sum_{l=1}^{I} \quad \left\{ -J \left(\hat{a}_{l+1}^{\dagger} \hat{a}_l + \hat{c}_{l+1}^{\dagger} \hat{c}_l + h.a. \right) + \frac{1}{2} U_{aa} \hat{n}_l^{(a)} \left(\hat{n}_l^{(a)} - 1 \right) \right.$$
$$\left. + U_{ac} \, \hat{n}_l^{(a)} \, \hat{n}_l^{(c)} + \epsilon_l \left(\hat{n}_l^{(a)} + \hat{n}_l^{(c)} \right) \right\}. \tag{3.5}$$

where $\hat{a}_l^{\dagger}, \hat{a}_l, \hat{n}_l^{(a)}$ refer to the bosonic species and $\hat{c}_l^{\dagger}, \hat{c}_l, \hat{n}_l^{(c)}$ to the spin-polarized fermionic species. For the sake of simplicity, we assume equal tunneling matrix-elements J for both species. U_{aa} is the boson-boson interaction is energy. Due to Pauli's exclusion principle, there is no multiple occupancy of fermions on a single lattice site and therefore no on-site fermion-fermion interaction U_{cc}. The inter-species interaction is described by U_{ac}. The topology of the superlattice is given by ϵ_l. Again, we employ the two-color superlattice depicted in Figure 3.1.

The many-body states are written as the direct product of the occupation number bases for bosons and fermions. A general many-body state can then be represented as a superposition of all possible combinations of the occupation-number states:

$$| \psi \rangle = \sum_{\alpha=1}^{D_a} \sum_{\beta=1}^{D_c} C_{\alpha\beta} \, | \, \{n_1^{(a)}, ..., n_I^{(a)}\}_\alpha \, \rangle \otimes \, | \, \{n_1^{(c)}, ..., n_I^{(c)}\}_\beta \, \rangle \, . \tag{3.6}$$

The sets of occupation numbers $\{n_1^{(a)}, ..., n_I^{(a)}\}$ for the bosonic component comprise all possible distributions of the N_a atoms over the I lattice sites with $\sum_l n_l^{(a)} = N_a$. For the fermionic occupation numbers $\{n_1^{(c)}, ..., n_I^{(c)}\}$ the additional constraint $n_l^{(c)} \in \{0, 1\}$

reflects the Pauli principle.

The following calculations were performed for a system with $I = 10$ lattice sites and $N_a = N_c = 5$ particles of each species using the complete basis of $D_a \cdot D_c = 504504$ occupation-number states. The boson-boson interaction energy is fixed to $U_{aa}/J = 20$ in order to simplify the discussion. Other (non-zero) values would not change the basic structure of the phase diagram but only cause a rescaling.

Figure 3.2 shows the maximum coefficient $C^2_{\max}$ of the occupation-number states in the ground state as a function of the boson-fermion interaction strength U_{ac}/J and super-lattice amplitude $\epsilon_{\max}/J$. This quantity already reveals the rich structure of the phase diagram. We can identify several straight lines or valleys of minimal $C^2_{\max}$ that subdivide the phase diagram into different regions. There is a horizontal line at $\epsilon_{\max} = U_{aa}$ and a vertical line at $U_{ac} = U_{aa}$, whose locations are determined by the boson-boson interaction strength and which are independent of the details of the lattice topology. In contrast, the additional diagonal valleys are governed by these details of the lattice topology, i.e., the set of on-site energies ϵ_l.

Typical occupation number distributions for bosons and fermions in the different areas of the phase diagram separated by those valleys are also presented in Figure 3.2. They correspond to the values of the boson-fermion interaction strength and the super-lattice amplitude marked by the labels in the phase-diagram. The characteristics of the different regions can be summarized as follows:

(A) In this region, the atoms are uniformly distributed over the lattice because of the dominant repulsive interactions. All occupation-number states with few particles per site are favored since the strong boson-fermion repulsion suppresses states with different species occupying the same site. Because of the commensurate filling and the strongly repulsive interactions between bosons as well as between bosons and fermions this phase is closely related to the Mott-insulating phase in a purely bosonic system.

(B) The mean occupation numbers of both species follow the shape of the superlattice potential. In the upper-left corner of this region two bosons are able to share the deepest superlattice wells with one fermion. An increasing boson-fermion repulsion U_{ac} forces one boson to leave the deepest superlattice well and the mean occupation

numbers exhibit a profile as depicted in inset (B).

(C) Above $\epsilon_{\max}/J = 20 = U_{aa}/J$ the on-site energy of the deepest superlattice wells exceeds the boson-boson interaction energy and they are capable to hold 2 bosonic particles. This double occupation occurs if the boson-fermion interaction overcomes the boson-boson interaction and forces the fermion to leave the deepest well.

(D) Complete localization of the bosons at the deepest superlattice sites induced by the strong repulsive boson-fermion interaction in spite of the boson-boson repulsion. In a purely bosonic system with $U_{aa}/J = 20$, a full localization would occur only for extremely strong superlattice potentials with amplitudes[1] $\epsilon_{\max}J > 210$. The presence of the fermions and the strong boson-fermion repulsion cause a separation of bosons and fermions, promoting the localization. The borders of this region of separation induced localization depend not only on the interaction strengths and the superlattice amplitude, but also on the filling. The more particles per super-cell are available, the further the onset of localization is pushed to larger superlattice amplitudes.

(E) Transition region between (B) and (C). This area of subtle rearrangements is governed by the finite differences of the on-site energies ϵ_l of the superlattice potential.

(F) Transition region between (B) and (D). The panel with the occupation numbers in Figure 3.2 indicates that the fermions on sites $l = 2$ and 7 successively force the bosons to the state of complete localization. If the bosons were the only species this would happen at much larger superlattice amplitudes.

The phase diagram in terms of the condensate fraction f_c of the bosonic species is depicted in the left panel of Figure 3.3. Three areas with a significant condensate fraction are visible. In the lower left corner at small boson-fermion interaction strengths and superlattice amplitudes, large condensate fractions occur in spite of the strongly repulsive boson-boson interaction ($U_{aa}/J = 20$), since the incommensurate boson filling averts a Mott-insulator phase. The condensate is depleted as soon as either the increasing boson-fermion interaction leads to a Mott-like phase, or the superlattice tends to localize the particles. The large condensate fractions in an extended region in the upper right part

---

[1] Consider a transition from a state with 1 boson at site 2 and 2 bosons at site 3 to a state with 3 particles at site 3. The reduction of the total energy due to the reduced on-site energy of the new state is compensated by an increase in interaction energy (see Fig. 3.1). For a superlattice amplitude $\epsilon_{\max}/J = 210$ these two competing energies are equal.
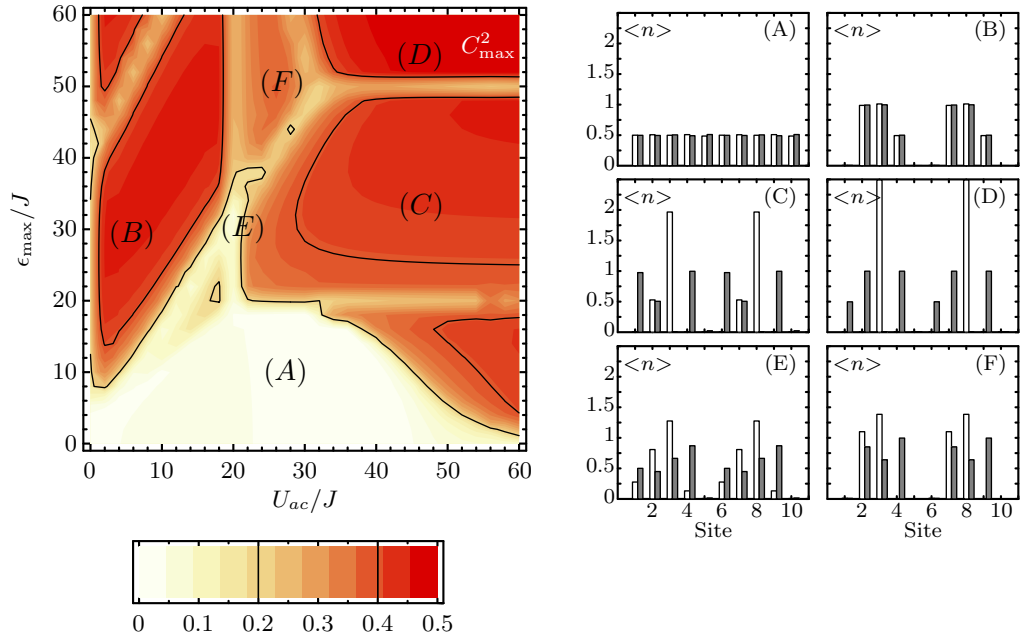
Figure 3.2: Right panel: $C_{\max}^2$ of a binary boson fermion system with $N_a = N_c = 5$ particles on $I = 10$ lattice sites. Left panel: The mean occupation numbers (white Bosons and gray Fermions) for the selected points in the phase diagram. The boson-boson interaction energy is a parameter in this plot and fixed at $U_{aa}/J = 20$.

and along the upper part of the $U_{ac}/J = 0$ axis have to be treated with care for they are "localized condensates" [41]. The almost complete localization of the bosonic particles at the deepest lattice sites $l = 3$ and 8 manifests in the corresponding diagonal matrix elements, i.e., the occupation numbers, of the one-body density matrix $\rho_{33}^{(1)}$ and $\rho_{88}^{(1)}$. In comparison, the other matrix elements are small except for the off-diagonal elements $\rho_{38}^{(1)}$ and $\rho_{83}^{(1)}$. This results in two large eigenvalues of the one-body density matrix and, therefore, in our description, in a large condensate fraction. Note, however, that this condensate is completely different from the condensate associated with the superfluid phase in a homogeneous lattice, where all particles are delocalized and exhibit long-range phase coherence. This characterization of the condensate is closely related to the existence of off-diagonal long-range order (see Section 2.7.3) in the one-body density matrix, which is absent in the case of the localized condensates. This interpretation is also supported by the behavior of the fringe visibility ν shown in the right panel of Figure 3.3. Clearly, the visibility is large at small boson-fermion interaction strengths and superlattice amplitudes (lower left corner) as expected for a conventional condensate. In contrast to this, there is no sizable fringe visibility in the upper-right region, indicating that the localized phase is incoherent and has to be distinguished from a genuine Bose-Einstein condensate. This also applies to the narrow stripe along the $U_{ac}/J = 0$ axis, where the fringe visibility exhibits an intermediate value. Again, the ground state is dominated by occupation-number states that have many bosonic particles at the deepest superlattice wells. In contrast to the area at the top right, not all of the particles are localized and thus many more occupation-number states contribute. The more occupation-number states contribute to the ground state, the more the phase coherence is restored, leading to more pronounced interference patterns.
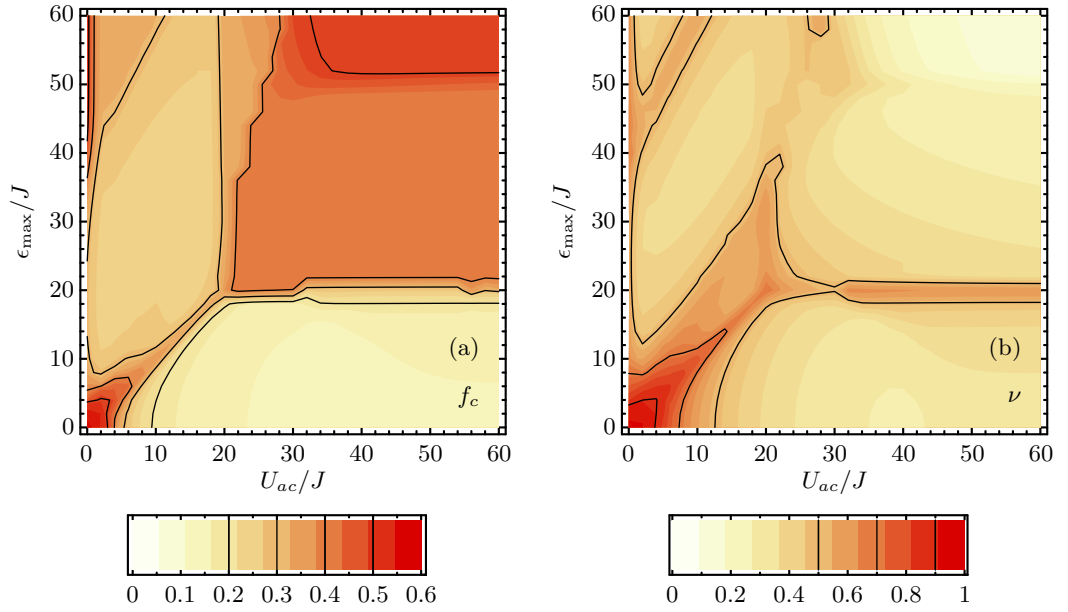
Figure 3.3: Binary boson-fermion mixture with $N_a = N_c = 5$ particles on $I = 10$ lattice sites at fixed boson-boson interaction energy $U_{aa}/J = 20$. (a): condensate fraction f_c of the bosonic species. (b): fringe visibility ν of the bosonic species. Although the condensate fraction at the top right is large, the fringe visibility vanishes there. This is due to the different nature of the localized condensates (see text).

3.2   Diagonalization in Truncated Hilbert spaces

One possible way to reduce the computational effort for exact-diagonalization techniques in order to extend these direct solutions of the eigenproblem to larger lattices and more particles is to decrease the size of the Hilbert space in a controlled and physically motivated manner. The challenge is to decide which occupation-number states are important and which can be discarded from the outset. Our ansatz for a basis truncation scheme is introduced in the following.

3.2.1   Importance Truncation

We are interested in a criterion that determines a subspace of the Hilbert space that is still able to provide a good approximate solution to the problem. As an example, consider a system deep within the Mott-insulating phase. Occupation-number states with many particles at one particular lattice site are associated with large interaction energies, which is why they are energetically unfavorable and therefore are not important for a proper description of the ground state, i.e. their overlaps with the ground state are very small meaning their coefficient C_α^2 is very small. Our ansatz is based on an exclusion of these less important occupation-number states from the beginning, leading to a significant reduction of the basis dimension. An application of our truncation scheme to a time-dependent Hubbard Hamiltonian – aiming at response under modulations of the optical lattice – can be found in Refs. [32, 33]. Furthermore, a similar importance-truncation scheme was also successfully applied in nuclear physics in the framework of the no-core shell model [42].

A simple but efficient a priori measure for the importance of individual occupation-number states is the expectation value e_α of the Hamiltonian (3.1). The following inequality is used to select the relevant basis states:

$$e_\alpha = \big\langle\, \{n_1, n_2, \ldots, n_I\}_\alpha \,\big|\, \hat{H} \,\big|\, \{n_1, n_2, \ldots, n_I\}_\alpha \,\big\rangle \le E_{\text{trunc}} \,. \tag{3.7}$$

Hence, occupation-number states associated with interaction or on-site energy contributions above a specific truncation energy E_{trunc} are discarded. By varying the parameters U and $\epsilon_{\max}$ in the Hamiltonian, one can optimize the basis for a particular region of the phase diagram. By varying the truncation energy E_{trunc} one can adjust the size of the truncated basis and at the same time assess the truncation errors. In a homogeneous lattice the energies e_α are grouped according to particle hole (*ph*) excitations with respect to the occupation-number state with exactly one particle per lattice site.

An occupation-number state from the $1p1h$ subspace, e.g., has $e_\alpha = U$ since it has one doubly occupied site.

The truncation scheme works particularly well in regions where the ground state is composed of a few dominant basis states, i.e., in regions of large $C_{\max}^2$. However, in regions where almost all occupation-number states contribute significantly, e.g., in the superfluid phase, the truncation scheme will be less effective. In order to confirm this, we have performed a diagonalization in the complete Hilbert space for $I = N = 7$ for a homogeneous system ($\epsilon_{\max} = 0$) and checked the correlations between e_α and $|C_\alpha|$. Figure 3.4 shows the individual energies e_α of the occupation-number states over their corresponding coefficients $|C_\alpha|$ in the superfluid as well as in the Mott-insulating regime. The dashed line marks the $2p2h$ subspace of the Hilbert space with dimension $D_{2p2h} = 358$. For $U/J = 2$ this means $E_{\mathrm{trunc}}/J = 2U/J \cdot 3(3-1)/2 = 6U/J$ and for $U/J = 10$, $E_{trunc}/J = 10U/J \cdot 3(3-1)/2 = 30U/J$. All basis states above the dashed line would be omitted by the truncation scheme. In the superfluid phase, a significant number of basis states with $|C_\alpha| \geq 0.01$ would be excluded which would result in a rather poor approximation of the ground state. In the Mott-insulating phase, however, all basis states with $|C_\alpha| \geq 0.005$ are included. Whether reliable results can be obtained from this approximate ground state has to be checked carefully by successively increasing the basis size, i.e., by using larger values for E_{trunc}, and testing the convergence of the observables. In the following section we will see that the approximate ground state reproduces all the relevant physics in the Mott-insulating phase very well.

3.2.2   Benchmark of the Truncation Scheme – Bosons

As a first benchmark, we study the effect of the basis truncation for the single-component Bose gas including the Mott-insulator to quasi Bose-glass transition. We employ the same superlattice topology as in the previous sections. The interaction energy is fixed at $U/J = 30$. The calculations performed with the complete basis are compared to calculations with two different truncation levels.

The generation of the truncated basis starts from a reference occupation-number state that is obtained by a minimization of the expectation value of the Hamiltonian within the manifold of Fock states for a given particle number. Multiple particle-hole excitations are generated from this reference state until the inequality (3.7) is no longer satisfied. If the truncation energy E_{trunc} is chosen large enough so that none of the new occupation-
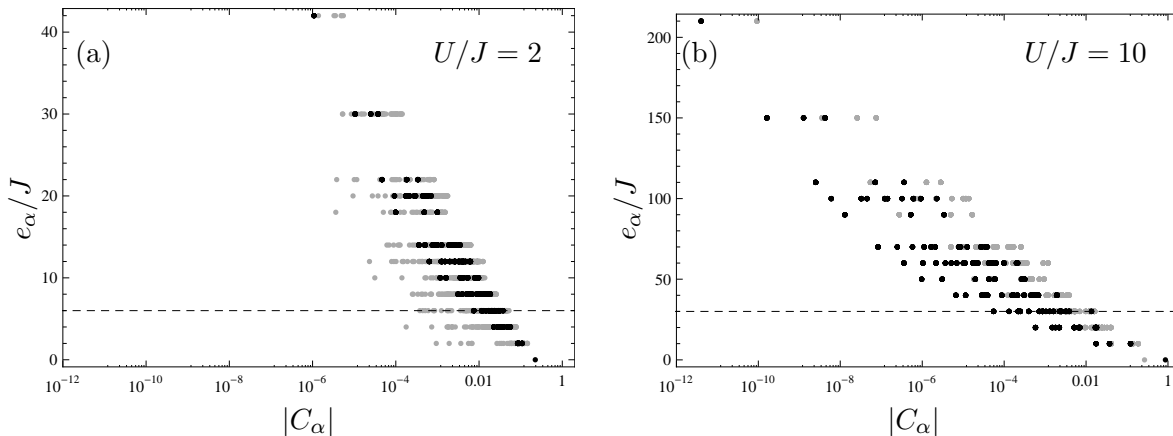
Figure 3.4: Individual energy expectation values e_α of the occupation-number basis states over their coefficients for the ground state (black) and the first excited state (gray). The homogeneous system under consideration is $I = N = 7$ and has a dimension of $D = 1716$. (a): superfluid phase $U/J = 2$, (b): Mott-insulating phase $U/J = 10$. The dashed line marks the $2p2h$ subspace ($e_\alpha/J = 6$ for $U/J = 2$ and $e_\alpha/J = 30$ for $U/J = 10$) that has a dimension of $D_{2p2h} = 358$.

number states can violate the inequality, this process would generate the complete set of occupation-number states. In principle, one could calculate an adapted basis for each point in the phase diagram, but for the sake of simplicity the phase diagram is split into three parts with different optimized basis. Table 3.1 lists the different ranges in $\epsilon_{\max}/J$, together with the corresponding basis dimensions and reference states. Since the importance-truncation approach satisfies the variational principle, we allow for overlaps at the borders of different sections of $\epsilon_{\max}/J$ and select the basis that yields the lowest ground state energy. The strong truncation includes $1p1h$ and some energetically favorable $2p2h$ excitations with respect to an appropriate reference state chosen for the particular region in the phase diagram. The dimension of the truncated basis is about 0.3% of the complete basis. For the basis with moderate truncation, some higher-order $npnh$ excitations are also included. Nevertheless, the dimension of the moderately truncated basis is still reduced to a mere 4% of the complete basis.

The dependence of the maximum coefficient $C_{\max}^2$ on the amplitude of the superlattice $\epsilon_{\max}/J$ at fixed interaction strength is depicted in Figure 3.5(a). If the amplitude $\epsilon_{\max}/J$ is smaller than the interaction strength U/J, the system is in the homogeneous

system	section (ϵ_{max}/J)	dimension	reference number state
strong truncation $\approx 0.3\%$ of complete basis	1-28	91	$\big| \{1,1,1,1,1,1,1,1,1,1\} \big\rangle$
	29-50	288	$\big| \{1,1,2,1,0,1,1,2,1,0\} \big\rangle$
	51-150	199	$\big| \{0,2,2,1,0,0,2,2,1,0\} \big\rangle$
moderate truncation $\approx 4\%$ of complete basis	1-29	3743	$\big| \{1,1,1,1,1,1,1,1,1,1\} \big\rangle$
	30-50	1866	$\big| \{1,1,2,1,0,1,1,2,1,0\} \big\rangle$
	51-150	2737	$\big| \{0,2,2,1,0,0,2,2,1,0\} \big\rangle$
complete basis	1-150	92378	–

Table 3.1: Basis dimensions and reference states for different truncation levels and different ranges of ϵ_{max}/J. In principle, an optimized basis for each value of ϵ_{max}/J could be chosen in order to improve the approximate ground state.

Mott-insulator phase and the number state with one particle per lattice site dominates. Further increase of the superlattice amplitude leads to the onset of the quasi Bose-glass phase, where a pattern of regions with small values of C^2_{max} and large number fluctuations σ_{max} and regions with large values of C^2_{max} and small σ_{max} emerges. For both C^2_{max} and σ_{max} the differences between the calculations with the complete and the truncated basis are barely visible. Only for the strongly truncated basis with 0.3% of the complete basis dimension, noticeable deviations occur. The basis using a moderate truncation to 4% yields results which are practically identical to calculations done in the complete Hilbert space.

Figure 3.5(c) illustrates the dependence of the condensate fraction f_c on the superlattice amplitude ϵ_{max}/J for fixed $U/J = 30$. Leaving the homogeneous Mott-insulator phase, the condensate fraction increases rapidly, reaching a local maximum at the transition point to the quasi Bose-glass phase at $\epsilon_{max}/J = 30$. After a slight decrease within the first lobe of the Bose-glass phase it increases again with ϵ_{max}/J. It seems that in the limit of large superlattice amplitudes ϵ_{max}/J, two separate localized condensates form at the deepest lattice wells. The term condensate has to be used with caution in this context – we already discussed the issue of localized condensates in Section 3.1.2. The deviations between calculations using the truncated and the complete basis for the condensate fraction are generally small. At the local maximum at $\epsilon_{max}/J = 30$ the exact calculation yields $f_c = 0.278$, the moderate truncation $f_c = 0.276$ and the strong truncation $f_c = 0.258$. It is an intrinsic feature of the truncation to underestimate the
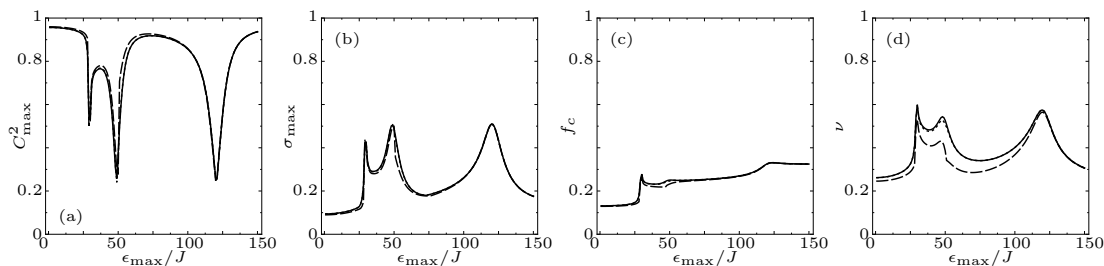
Figure 3.5: . From left to right: maximum coefficient $C_{\max}^2$, maximum number-fluctuation $\sigma_{\max}$, condensate fraction f_c, and visibility of the interference patterns ν, all plotted over the amplitude of the superlattice $\epsilon_{\max}/J$ at fixed interaction strength $U/J = 30$. Calculations within the complete basis (solid line), truncated to 4% of the complete basis (dotted line), and truncated to 0.3% of the complete basis (dashed line). The results of the complete basis and the truncated basis with 4 % of the full dimension coincide almost everywhere.

condensate fraction because of the occupation-number states that are excluded during the calculation of the one-body density-matrix. The kink at $\epsilon_{\max}/J = 50$ (dashed line) is due to the change of the basis at this point (see Tab. 3.1). In principle one could adopt another optimized basis in this region in order to improve the description and avoid this effect.

Figure 3.5(d) shows the fringe visibility as a function of $\epsilon_{\max}/J$ for fixed $U/J = 30$. In accord with the maxima of $\sigma_{\max}$ and the kinks of the condensate fraction, the visibility of the interference pattern shows local maxima each time the particles are rearranged due to the increasing superlattice amplitude. The strongly truncated basis is not able to give correct quantitative results, although the locations maxima are reproduced qualitatively. The moderately truncated basis shows only minor deviations and yields almost the exact visibilities.

The matter-wave interference pattern after the release of the atoms from the lattice and a free expansion is also investigated. Figure 3.6 shows three values of the superlattice amplitude $\epsilon_{\max}/J$ in the vicinity of the transition point from the homogenous Mott-insulator to the quasi Bose-glass phase. From the sequence of interference patterns one can see that the height of the peak at quasi-momentum zero reaches a maximum at $\epsilon_{\max} = U$, with an absolute value below the condensate occupation number. Note that in a homogeneous lattice the condensate wave function – the lowest natural orbital – is identical to the quasi-momentum zero Bloch function. Hence, in that case the occupa-
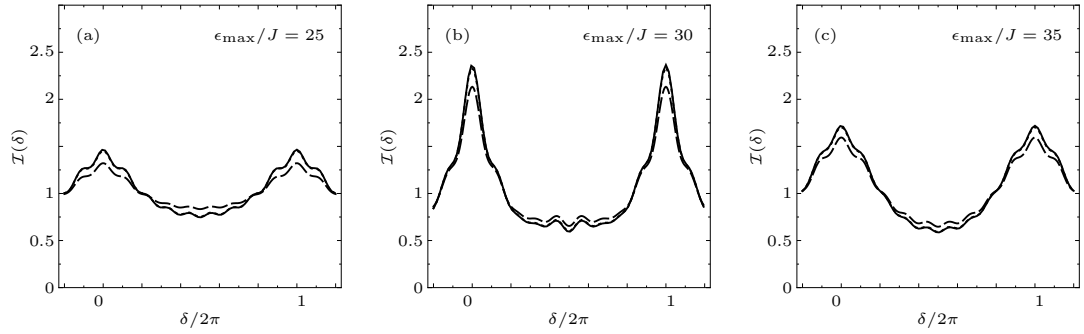
Figure 3.6: Matter-wave interference pattern in the vicinity of the Mott-insulator to the quasi Bose-glass transition point at fixed interaction strength $U/J = 30$. Calculations within the complete basis (solid line), the basis truncated to 4% of the complete basis (dotted line), and the basis truncated to 0.3% of the complete basis (dashed line). The dotted line almost perfectly covered by the solid line because of the good reproduction of the calculations using the complete basis.

tion of the quasi-momentum zero mode is equal to the lowest eigenvalue of the one-body density matrix. However, this relation does not hold for irregular lattice potentials.

As already mentioned, we expect the largest deviations between calculations using the truncation scheme and calculations using a complete basis, if a large number of basis states is necessary to represent the ground state. But even in the transition region, where this occurs, less than 1% of the complete set of occupation-number states is sufficient to reproduce the properties of the system qualitatively. The basis including 4% of the complete set of occupation-number states included shows virtually no deviation from the exact calculation. It seems that the estimate (3.7) is a suitable *a-priori* measure to select the physically relevant occupation-number states.
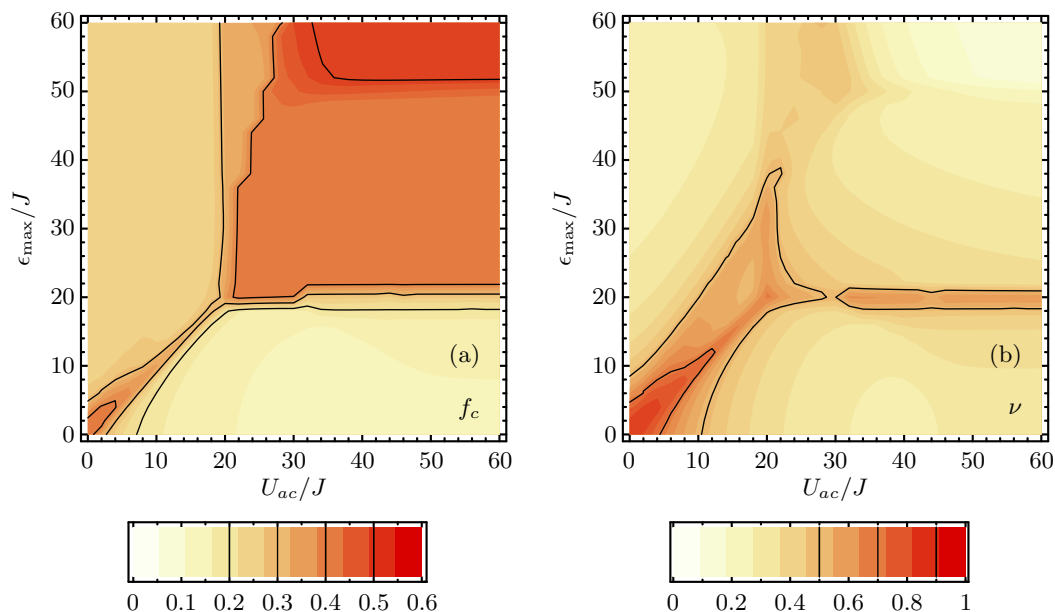
Figure 3.7: Binary boson-fermion mixture with $N_a = N_c = 5$ and $I = 10$ for fixed $V_{aa}/J = 20$ calculated with a truncated basis of roughly 15% of the full dimension. Left panel: condensate fraction f_c of the bosonic species, right panel: fringe visibility ν of the bosonic species. The comparison with Figure 3.3 illustrates the quality of the truncated calculation.

3.2.3   Benchmark of the Truncation Scheme – Boson-Fermion Mixtures

We now apply the basis truncation scheme to a binary boson-fermion mixture and repeat the calculations of section 3.1.2 for $I = 10$ and $N_a = N_c = 5$. The truncation of the basis again makes use of the importance criterion (3.7).

For the present example the basis dimension is reduced to $D_a \cdot D_c = 72762$, i.e., about 15% of the occupation-number states of the complete basis. For the sake of simplicity we use this rather large set because the phase diagram is not partitioned into several areas with different optimized bases. Only one basis, optimized for $\epsilon_{\max} = U_{aa} = U_{ac}$ is employed. Again, we could also work with an optimized basis for each point or for particular regions of the phase diagram to improve the quality of the results.

We consider the condensate fraction and the fringe visibility, as shown in Figure 3.7, for the truncated calculations. The general structure of the phase diagram of Figure

3.3 is reproduced well by the approximate ground states. The absolute value of the condensate fraction is underestimated in the truncated calculation, as discussed earlier. In close connection to this, the narrow stripe at the top left of right panel of Figure 3.7 shows a significantly smaller visibility ν than in the complete calculation. This is because occupation-number states with many particles at the same lattice site are discarded by the truncation scheme due to the optimization to a region where the boson-fermion interaction plays a significant role. Although the coefficients $C_{\alpha\beta}$ of the missing number states would have been small, their contribution to the off-diagonal elements of the one-body density matrix is sizable. Their omission causes a reduction of coherence and thereby reduces the visibility of the interference pattern.

Despite the quantitative deviations in certain regions of the phase diagram, its global structure can be fully described by the truncated basis. Naturally, the use of adapted bases in the different characteristic regions of the phase diagram would improve the quantitative agreement.

3.3 Applications of the Importance Truncation

3.3.1 Larger Systems and Finite-Size Effects – Bosons

As a first application of the truncation scheme in a regime where calculations with the complete basis are not feasible any longer, we study the impact of finite size effects for a single-component Bose gas in superlattice. To this end, we extend the two-color lattice (see Fig. 3.1) to three and four super-cells, corresponding to a problem of 15 bosons with 15 lattice sites ($N = I = 15$) with a full basis dimension $D = 77\,558\,760$ and 20 bosons with 20 lattice sites ($N_a = I = 20$) with a full basis dimension $D = 68\,923\,264\,410$, respectively. We employ truncations to 1% and 0.001% of the respective full basis dimensions.

Since we are now considering one bosonic species only, we omit the indices at the interaction parameter: $U_{aa} \rightarrow U$. Figure 3.8 demonstrates the dependence of the condensate fraction on $\epsilon_{\max}/J$ at fixed $U/J = 30$ for the truncated three- and four-super-cell system. The comparison with the complete calculation for the two-super-cell system displayed in Figure 3.5 reveals that the condensate fraction is generally reduced. The reason for this is two-fold: First, the basis truncation leads to an underestimation of the condensate fraction as discussed in Section 3.2.2. Second, finite size effects are relevant for the condensate fraction. The simplest indication for this results from the existence of
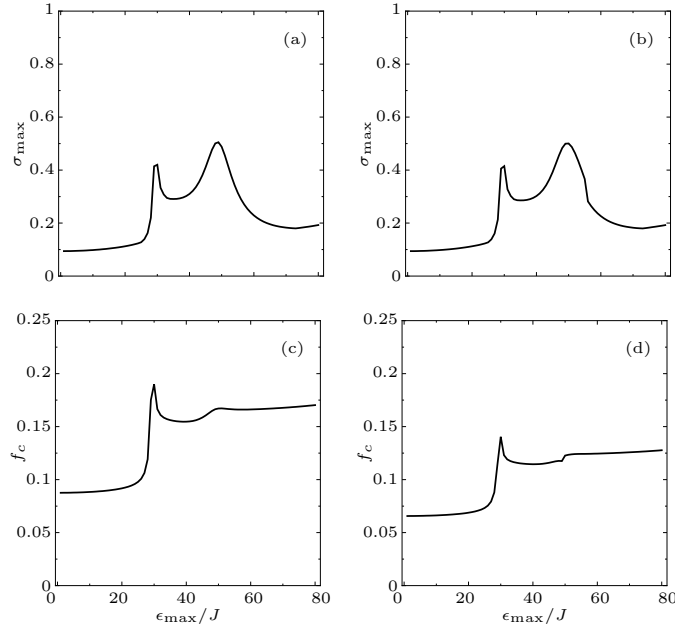
Figure 3.8: Upper row: Maximum number-fluctuation, lower row: condensate fraction. (a)+(c): $N = I = 15$ with a truncated basis of dimension $D = 546589$, (b)+(d): $N = I = 20$ with a truncated basis of dimension $D = 797232$. In all plots, the interaction energy is fixed at $U/J = 30$.

a lower bound for f_c, which is proportional to $1/I$, as shown in Section 2.7.3. Hence, the smallest possible value for the condensate fraction is given by $f_c^{\min} = 1/I$. For the genuine Mott-insulating phase in a regular lattice of increasing size, the condensate fraction would approach zero like $1/I$. In agreement with this intrinsic size dependence, the condensate fraction within the Mott-insulating phase ($\epsilon_{\max}/U$) shown in Figure 3.8 tends to smaller values.

The resulting matter wave interference patterns for $U/J = \epsilon_{\max}/J = 30$, i.e., at the transition from homogeneous Mott-insulator to the quasi Bose-glass phase, are depicted in Figure 3.9. They can be compared to the result using the complete basis for a system of two super cells shown in Figure 3.6. The matter-wave interference patterns seem to be barely affected by the truncation and are of the same general shape for all system sizes. Only the increasing number of possible quasimomenta $k_j = 2\pi/(Ia)j$ with $j = 0, 1, 2, \ldots I - 1$ is reflected in the substructure of the interference peaks.
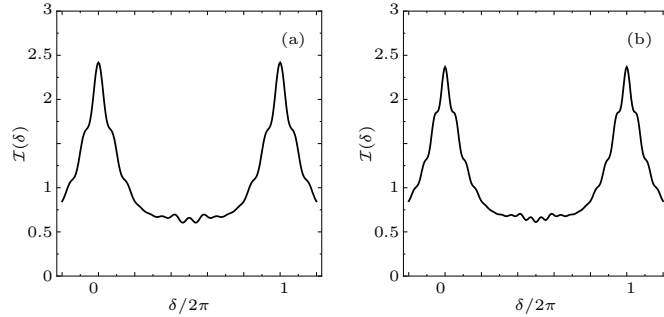
Figure 3.9: Interference pattern at $\epsilon_{\max}/J = U/J = 30$. (a): $N = I = 15$ with a truncated basis of dimension $D = 546589$. (b): $N = I = 20$ with a truncated basis of dimension $D = 797232$.

From these investigations we can conclude that finite-size effects are under control for the global observables like the condensate fraction and the interference pattern, thus calculations performed in small systems are well suited for qualitative and even semi-quantitative predictions for larger systems. Local observables like the maximum number-fluctuation depicted in Figure 3.8 are practically size-independent. These findings are also confirmed by more sophisticated calculations presented in Section 5.3.

3.3.2   Two-Color Superlattice beyond Half-Filling – Boson-Fermion Mixtures

In order to investigate the influence of the filling factor on the phase diagram, we consider a system with $N_a = N_c = 7$ particles on $I = 10$ lattice sites. The complete basis for this system consists of $D_a \cdot D_c = 1372800$ occupation-number states. For the present calculations a truncation to 22% of the complete basis was used.

The maximum coefficient $C_{\max}^2$ as a function of U_{ac}/J and $\epsilon_{\max}/J$ for fixed $U_{aa}/J = 20$, depicted in Figure 3.10, reveals a phase diagram with a structure different from the half-filling case shown in Figure 3.2. The most significant difference is the absence of a genuine Mott-insulator phase in the lower part of the phase diagram. Even in the limit of very strong repulsive interactions, a homogeneous Mott-insulator phase cannot be realized since there are always lattice sites occupied with more than one particle due to the incommensurate filling. For this reason pairs of bosons and fermions occupy the lattice with a distribution following the topology of the superlattice in region (A), where the boson-fermion interaction is negligible compared to the boson-boson repul-
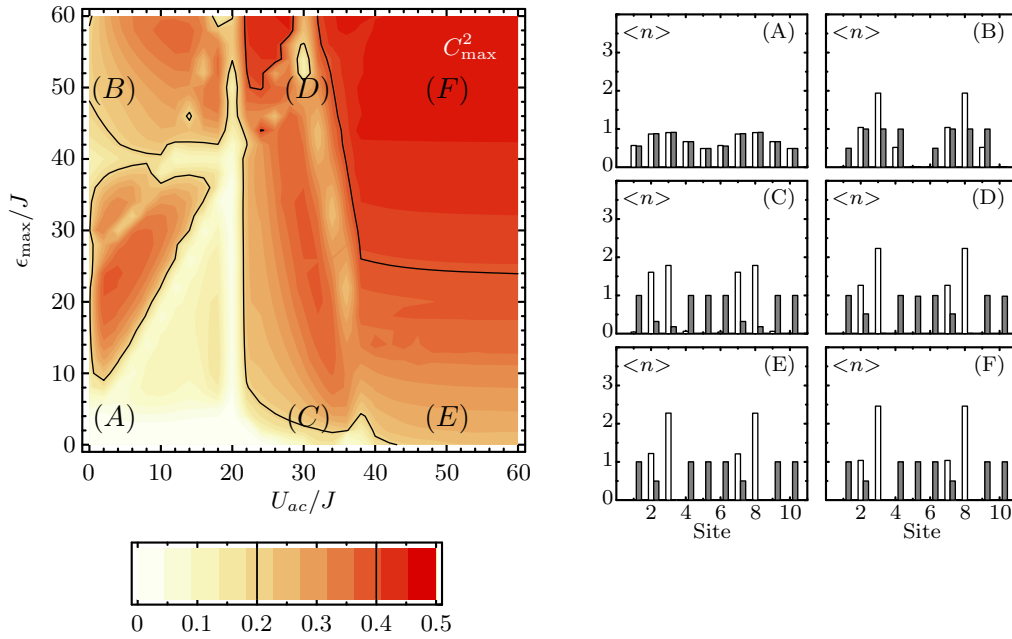
Figure 3.10: Binary boson-fermion mixture with $I = 10$, $N_a = N_c = 7$. Left panel: maximum coefficient C^2_{max} in the expansion of occupation-number states, right panel: mean occupation numbers (white Bosons, gray Fermions) $n_l^{(a)}$ ($n_l^{(c)}$) of the bosonic (fermionic) species. The boson-boson interaction energy is fixed at $U_{aa}/J = 20$.

sion. An increase of the superlattice amplitude [region (B)] leads to a bosonic double occupancy of the deepest superlattice wells, whereas the fermions are forced to spread over several sites with mean occupation numbers less than or equal to one. The horizontal line, which appeared in the half-filling case for superlattice amplitudes ϵ_{max} equal to the boson-boson interaction strength U_{aa}, vanishes because of the incommensurability. For strong boson-fermion repulsion, any slight irregularity of the lattice, i.e., a small nonzero superlattice amplitude, leads to multiple boson occupancies at the deeper lattice sites. A comparison of the mean occupation numbers at (C) and (D) or at (E) and (F) shows that if the boson-fermion interaction exceeds the boson-boson interaction, the mean occupation numbers are stable against increasing superlattice amplitude. At the same time, however, the increasing value of C^2_{max} indicates that the number fluctuations decrease successively.

The phase diagram of a boson-fermion mixture beyond half-filling is less structured, since the homogeneous Mott-insulator phase at small superlattice amplitudes is absent.

In the region of strong boson-fermion interaction any slight irregularity within the lattice immediately leads to double occupancies of the deeper site. For increasing superlattice amplitude, the mean occupation numbers are almost unaltered, only the number fluctuations decrease.

Chapter 4

Density-Matrix Renormalization Group (DMRG)

4.1 Reduced Density-Matrix

Because the density-matrix formalism is crucial for the understanding of the Density-Matrix Renormalization Group (DMRG) algorithm, it is worthwhile to briefly summarize some important features we will use during the introduction of DMRG. The discussion follows Feynman's textbook on Statistical Mechanics [43].

When solving a physical problem one usually considers either a closed system or an open system that is coupled to an environment. Although we are only interested in properties of the system, we will derive how observables inside the system change if we allow for a coupling to an environment. Let $\mid \phi_i \rangle$ and $\mid \theta_i \rangle$ be complete and orthonormal sets of basis states for the system and for the environment, respectively. A general state $\mid \psi \rangle$ can be expanded in a tensor-product basis of system and environment $\mathcal{H} = \mathcal{H}_{\mathrm{sys}} \otimes \mathcal{H}_{\mathrm{env}}$:

$$\mid \psi \rangle = \sum_{ij} C_{ij} \mid \phi_i \rangle \otimes \mid \theta_j \rangle = \sum_{ij} C_{ij} \mid \phi_i \, \theta_j \rangle. \qquad (4.1)$$

If an operator acts on the system only, i.e., $\hat{A} = \hat{a} \otimes \hat{1}$, its expectation value is given by

$$
\begin{aligned}
\langle \hat{A} \rangle = \langle \psi \mid \hat{A} \mid \psi \rangle &= \sum_{ii'jj'} C^*_{i'j'} C_{ij} \langle \phi_{i'} \theta_{j'} \mid \hat{a} \otimes \hat{1} \mid \phi_i \theta_j \rangle \\
&= \sum_{ii'jj'} C^*_{i'j'} C_{ij} \langle \phi_{i'} \mid \hat{a} \mid \phi_i \rangle \cdot \delta_{j'j} \\
&= \sum_{ii'} \langle \phi_{i'} \mid \hat{a} \mid \phi_i \rangle \cdot \rho^{\text{red}}_{ii'}
\end{aligned}
\tag{4.2}
$$

where we have introduced the *reduced density matrix*

$$
\rho^{\text{red}}_{ii'} = \sum_j C^*_{i'j} C_{ij} .
\tag{4.3}
$$

The diagonal elements of ρ^{red}_{ii} are the probabilities to find a specific state $\mid \psi \rangle$ in the basis state $\mid \phi_i \rangle$ of the system without resolving the basis state of the environment $\mid \theta_i \rangle$. Even if an operator acts within the system only, the reduced density-matrix provides an implicit coupling to the enviroment. The operator form of the reduced density-matrix can be obtained by taking the complete density-matrix and tracing out the environment

$$
\begin{aligned}
\text{Tr}_{\text{env}} \left(\mid \psi \rangle\!\langle \psi \mid \right) &= \sum_{j''} \sum_{ii'} C^*_{i'j''} C_{ij''} \mid \phi_i \rangle\!\langle \phi_{i'} \mid \\
&= \hat{\rho}^{\text{red}} .
\end{aligned}
\tag{4.4}
$$

Note that $\hat{\rho}^{\text{red}}$ acts in the Hilbert space of the system only. Whenever it acts in the combined Hilbert space of system and environment, we have to write:

$$
\hat{\rho}^{\text{red}} = \sum_{j''} \sum_{ii'} C^*_{i'j''} C_{ij''} \mid \phi_i \theta_{j''} \rangle\!\langle \phi_{i'} \theta_{j''} \mid .
\tag{4.5}
$$

Using this operator form of the reduced density-matrix, the expectation value of $\hat{A}$ in Eq. (4.2) can be calculated via

$$
\langle \hat{A} \rangle = \langle \psi \mid \hat{A} \mid \psi \rangle = \text{Tr} \left(\mid \psi \rangle\!\langle \psi \mid \hat{A} \right) = \text{Tr}_{\text{sys}} \left(\hat{\rho}^{\text{red}} \hat{a} \right) .
\tag{4.6}
$$

Since $\hat{\rho}^{\text{red}}$ is hermitian it can be diagonalized, resulting in a complete set of orthogonal eigenvectors $\mid w^{(\alpha)} \rangle$ and real eigenvalues $w^{(\alpha)}$:

$$
\hat{\rho}^{\text{red}} \mid w^{(\alpha)} \rangle = w^{(\alpha)} \mid w^{(\alpha)} \rangle , \qquad w^{(\alpha)} \geq w^{(\alpha+1)} ,
\tag{4.7}
$$

where we assume an odering of the eigensystem with respect to the eigenvalues. Using Eq. (4.6) one can show that the eigenvalues obey the relations

$$
\begin{aligned}
w^{(\alpha)} = \left\langle \mid w^{(\alpha)} \middle\rangle\!\!\middle\langle w^{(\alpha)} \mid \right\rangle &= \mathrm{Tr}_{\mathrm{sys}} \left(\hat{\rho}^{\mathrm{red}} \mid w^{(\alpha)} \middle\rangle\!\!\middle\langle w^{(\alpha)} \mid \right) \\
&= \mathrm{Tr} \left(\mid \psi \middle\rangle\!\!\middle\langle \psi \mid \sum_j \mid w^{(\alpha)}\, \theta_j \middle\rangle \middle\langle w^{(\alpha)}\, \theta_j \mid \right) \\
&= \left\langle \psi \mid \left(\sum_j \mid w^{(\alpha)}\, \theta_j \middle\rangle \middle\langle w^{(\alpha)}\, \theta_j \mid \right) \mid \psi \right\rangle \\
&= \sum_j \left| \left\langle \psi \mid w^{(\alpha)}\, \theta_j \right\rangle \right|^2 \\
&\geq 0
\end{aligned}
\tag{4.8}
$$

and

$$
\sum_\alpha w^{(\alpha)} = \mathrm{Tr}_{\mathrm{sys}} \left(\hat{\rho}^{\mathrm{red}} \cdot \hat{\mathbf{1}} \right) = \left\langle \psi \mid \hat{\mathbf{1}} \mid \psi \right\rangle = 1.
\tag{4.9}
$$

To obtain a good approximation of the expectation value of an operator acting on the system, i.e., $\hat{A} = \hat{a} \otimes \hat{1}$, by referring to a subspace of dimension D_{sub} only, it is reasonable to neglect those states with small eigenvalues $w^{(\alpha)}$:

$$
\left\langle \psi \mid \hat{A} \mid \psi \right\rangle = \mathrm{Tr}_{\mathrm{sys}} \left(\hat{\rho}^{\mathrm{red}}\, \hat{a} \right) = \sum_{\alpha=1}^{D} w^{(\alpha)} \left\langle w^{(\alpha)} \mid \hat{a} \mid w^{(\alpha)} \right\rangle \approx \sum_{\alpha=1}^{D_{\mathrm{sub}}} w^{(\alpha)} \left\langle w^{(\alpha)} \mid \hat{a} \mid w^{(\alpha)} \right\rangle.
\tag{4.10}
$$

One can even show that this approximation of the expectation values is optimal in a sense that the truncation error is minimal [44, 45]. This is closely related to the so-called Rayleigh-Ritz method. The truncated weight

$$
\Delta = 1 - \sum_{\alpha=1}^{D_{\mathrm{sub}}} w^{(\alpha)}
\tag{4.11}
$$

can furthermore serve as an estimate for the truncation error.

This optimized approximation of the expectation values in a truncated basis along with the additional, information from the environment mimicking a physically larger system, is the primary mechanism that is responsible for the success of the density-matrix renormalization-group algorithm introduced in Section 4.5.

4.2   Concept of the Renormalization-Group Scheme

The renormalization group (RG) was originally developed by K. G. Wilson in 1975 [47].
In 1982 he received the Nobel prize "for his theory for critical phenomena in connection
with phase transitions"[1]. Initially formulated in quantum field theory, RG can also be
applied to real space systems [48].

Most often, the huge amount of degrees of freedom is a problem when treating realistic
quantum system numerically. In quantum mechanics a state can be a linear superposition of all elements of the underlying Hilbert space. Usually, one has to store many
numbers to represent and manipulate such a state. The Hilbert space of the single-band
Hubbard model, for instance, grows factorially with the length of the optical lattice and
the total particle number [see Eq. (3.3)]. In Chapter 3 we have introduced a basis truncation scheme that allows a physically motivated selection of subspaces of the complete
Hilbert space including relevant degrees of freedom for a particular problem. However,
if the resulting space is still too big or ill-suited to describe certain features to a desired
accuracy, we have to resort to other methods.

In contrast to the *a-priori* approach of the basis truncation scheme, we now apply an
in-situ method to truncate the Hilbert space. Consider the problem of N bosons on I
lattice sites. If we construct the basis of a Hilbert space by successively adding more and
more degrees of freedom, this basis will grow factorially with respect to the length of the
lattice and the number of particles. RG methods offer a solution for this size-explosion
problem. During the growing procedure one keeps the size of the Hilbert space constant
by projecting onto a new basis and by "integrating out" certain subspaces of the Hilbert
space. Naturally, one wants to drop those subspaces that are least relevant to describe
a desired *target state*, usually the ground state or one of the low-lying excited states.

The numerical renormalization group (NRG) and the density-matrix renormalization
group (DMRG) follow different approaches to decide which subspaces to keep and which
subspaces to drop. Both algorithms require a convenient way to add degrees of freedom
successively. Those degrees of freedom that are coupled by the Hamiltonian have to
be grouped with respect to their mutual correlation. The easier this grouping can be
achieved, the better the algorithms work. Finding an appropriate ordering is hard work
in general, even in one-dimensional systems. From this point of view NRG and DMRG

---

[1]text from *nobelprize.org*

algorithms are less universal than a much simpler *a-priori* truncation of the Hilbert space. However, in Hubbard-type models the new degrees of freedom are the newly attached lattice sites. Since the Hubbard Hamiltonian connects adjacent lattice sites only, a natural grouping is obvious and these algorithms can fully unveil their potential.

4.3   Partitioning of the Hilbert Space

In this section we will discuss the conceptual and technical issues related to the partitioning of the Hilbert space with the aim of adding degrees of freedom to a system. For the sake of simplicity we consider homogeneous systems only; the procedure for inhomogeneous systems is absolutely identical. We consider bosonic particles in an optical lattice of length L, which we will call *block*. The aim is to enlarge the block to length $L+1$ via a direct product of Hilbert spaces.

The Bose-Hubbard Hamiltonian with L lattice sites reads in occupation-number representation:

$$\hat{H}_{b\,(L)} = \sum_{i=1}^{L} \Big(- J\big(\hat{a}_i^\dagger \hat{a}_{i+1} + \hat{a}_{i+1}^\dagger \hat{a}_i\big) + \frac{1}{2}U\,\hat{a}_i^\dagger \hat{a}_i^\dagger \hat{a}_i \hat{a}_i \Big). \tag{4.12}$$

In order to switch to a matrix representation of the Hamiltonian, we consider a complete set of D_b occupation-number states with a finite, yet not constrained total particle number. We can obtain a matrix representation of the creation and annihilation operators for each lattice site. For instance, the matrix elements of the operators at site i are given by

$$a_i^{nm} = \big\langle \{n_1, ..., n_L\}_n \,\big|\hat{a}_i\,\big|\, \{n_1, ..., n_L\}_m \big\rangle, \tag{4.13}$$

$$a_i^{\dagger\,nm} = \big\langle \{n_1, ..., n_L\}_n \,\big|\hat{a}_i^\dagger\,\big|\, \{n_1, ..., n_L\}_m \big\rangle. \tag{4.14}$$

Note that bras and kets belong to subspaces of the Fock space with different total particle numbers. The Hamiltonian can be expressed by the product of creation and annihilation operators for the individual sites, yielding the matrix representation

$$H_{b\,(L)} = \sum_{i=1}^{L} \Big(- J\big(a_i^\dagger a_{i+1} + a_{i+1}^\dagger a_i\big) + \frac{1}{2}U\,a_i^\dagger a_i^\dagger a_i a_i \Big), \tag{4.15}$$

where $H_{b\,(L)}, a_i, a_i^\dagger, n_i \in \mathbb{C}^{D_b \times D_b}$. Assuming that the number basis is complete and the boundary conditions are defined, the diagonalization of the Hamilton matrix would yield the exact solution of the problem for all included particle numbers. Because the
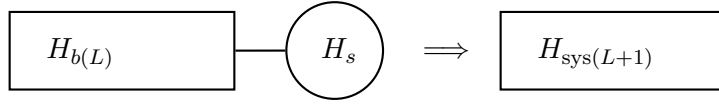
Figure 4.1: Building the system by combining block and site.

Hamiltonian matrix contains more than one total particle number, it can be cast into a block-diagonal form because the Hubbard Hamiltonian conserves the particle number.

Since RG algorithms are based on a successively growing system, we now have to specify degrees of freedom we can attach. In general, this could be a similar system of any size, e.g. a second block of size L. In practice, however, the attachment of a single site leads to much better convergence.

The Hamilton matrix of a single site has no tunneling term and reads

$$H_s = U/2 \left(a^\dagger a^\dagger a a \right). \tag{4.16}$$

Its dimension is given by the dimension D_s of the Fock space of the new site, i.e., $H_s, a, a^\dagger \in \mathbb{C}^{D_s D_s}$.

In order to describe a *system* of size $L + 1$, we have to combine block and site as illustrated in Figure 4.1. The resulting Hamilton matrix $H_{\text{sys}(L+1)} \in \mathbb{C}^{D_b D_s \times D_b D_s}$ represents the block Hamiltonian with an additional site. Its basis is defined via the tensor product of the Fock spaces of block and site

$$\mathcal{F}_{\text{sys}(L+1)} = \mathcal{F}_{b(L)} \otimes \mathcal{F}_s. \tag{4.17}$$

For the elements of the Fock spaces we use the following notation:

$$\begin{aligned}
\big| \{m_L\}_k \big\rangle &\in \mathcal{F}_{b(L)}, & \dim \mathcal{F}_{b(L)} &= D_b, \\
\big| \{\sigma\}_k \big\rangle &\in \mathcal{F}_s, & \dim \mathcal{F}_s &= D_s, \\
\big| \{m_L\}_k \big\rangle \otimes \big| \{\sigma\}_l \big\rangle \equiv \big| \{m_L\sigma\}_m \big\rangle &\in \mathcal{F}_{\text{sys}(L+1)}, & \dim \mathcal{F}_{\text{sys}(L+1)} &= D_b D_s.
\end{aligned} \tag{4.18}$$

The system Hamiltonian is composed of block and site parts, and a coupling term

$$\hat{H}_{\text{sys}(L+1)} = \hat{H}_{b(L)} \otimes \hat{1} + \hat{1} \otimes \hat{H}_s + \hat{H}_{b(L)-s}. \tag{4.19}$$

The explicit form of a matrix element $\big\langle \{m_L\}_k \big| \big\langle \{\sigma\}_l \big| \hat{H}_{\text{sys}(L+1)} \big| \{m_L\}_{k'} \big\rangle \big| \{\sigma\}_{l'} \big\rangle$ reads

$$H_{\text{sys}(L+1)}^{kk'll'} = H_{b(L)}^{kk'} \delta_{ll'} + H_{b(L)-s}^{ll'kk'} + H_s^{ll'} \delta_{kk'}. \tag{4.20}$$
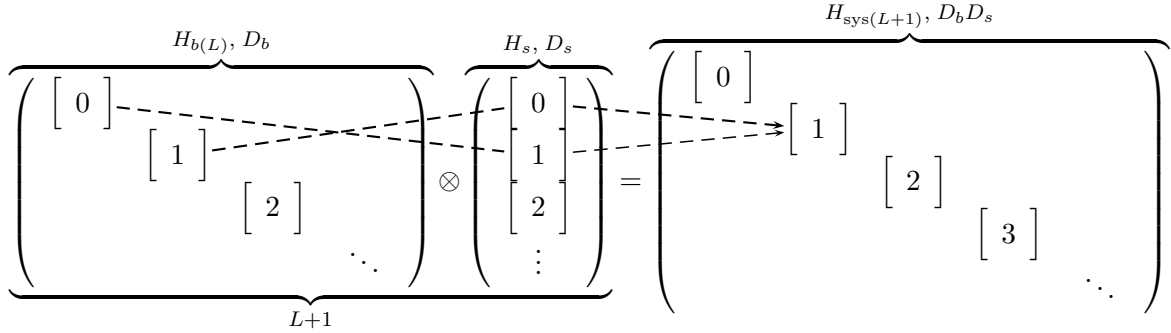
Figure 4.2: Illustration of the tensor product in terms of matrices. The numbers in square brackets denote a block matrix for the respective particle number, e.g., the new subspace for 1 particle within the system can be build up from either one particle from the block and zero from the site or vice versa. In general, the dimensions of the subspaces are not equal.

The coupling term $H_{b(L)-s}^{ll'kk'}$ is defined via the tunneling of particles between the block and the new site

$$\hat{H}_{b(L)-s} = -J\Big(\underbrace{\hat{a}_L^\dagger}_{\text{block}} \cdot \underbrace{\hat{a}}_{\text{site}} + \underbrace{\hat{a}^\dagger}_{\text{site}} \cdot \underbrace{\hat{a}_L}_{\text{block}} \Big), \tag{4.21}$$

where the additional site is attached to the block at the rightmost site. The operator structure is defined by

$$\underbrace{\hat{a}_L}_{\text{block}} = \hat{a}_L \otimes \hat{1}, \tag{4.22}$$

$$\underbrace{\hat{a}}_{\text{site}} = \hat{1} \otimes \hat{a}. \tag{4.23}$$

The tensor product of block and site is sketched in Figure 4.2. As already mentioned, the Hubbard Hamiltonian conserves the total particle number, hence the matrices H_b, H_s, and H_{sys} are block-diagonal and we always assume a sorting with respect to increasing total particle number starting from the upper left.

So far, we have started with a block of size L and dimension D_b and added an additional site of length 1 and dimension D_s. We end up with a system of length $L+1$ and dimension $D_b \cdot D_s$. If we would continue this procedure n times, the Fock space would grow like $D_b \cdot (D_s)^n$. In order to keep the basis size constant during the growing process, we have to truncate the Fock space of the system before the next lattice site is added. One possibility how to do this will be introduced in the next section.

4.4 NRG

Although the numerical renormalization group (NRG) algorithm is supposed to be obsolete due to its rather bad convergence, it nicely illustrates the basic idea of the renormalization step, namely a non-unitary transformation to a new, truncated basis. We will not present actual calculations performed with NRG, but it is helpful to understand the more powerful density-matrix renormalization group (DMRG) method and to underline its advantages. An application of the NRG algorithm to the Hubbard model was the subject of a Bachelor thesis [49] in our group.

Our aim is to calculate the ground state of N particles on I lattice sites, at a defined filling fraction N/I. Furthermore, we want to resort to a procedure that requires only a fixed number of basis states for any system size I under consideration. Since it is not obvious from the beginning, which basis describes the problem best, we use an iterative procedure that successively determines an appropriate basis after each growing step.

After having built block, site and system according to Section 4.3, we solve the eigenvalue problem for the system:

$$\hat{H}_{\text{sys}(L+1)} \left| \psi^{(\nu)} \right\rangle = E^{(\nu)} \left| \psi^{(\nu)} \right\rangle, \qquad E^{(\nu)} \leq E^{(\nu+1)}, \tag{4.24}$$

$$\left| \psi^{(\nu)} \right\rangle = \sum_{k=1}^{D_b D_s} c_k^{(\nu)} \left| \{m_L \sigma\}_k \right\rangle. \tag{4.25}$$

Note that the ordering of the eigenstates with respect to increasing eingenvalues is crucial. Due to the block structure of the Hamiltonian, resulting from particle-number conservation, the eigenvalue problem can be solved for each subspace separately. Keeping in mind Eq. (4.18), we look for a suitable *lossy* projection of the Hamiltonian and the operators expressed in the $D_b D_s$-dimensional basis of the system to a new basis which has the dimension D_b of the block only. Since we are interested in the ground state, a first ansatz is a projection onto the D_b eigenstates from the lower end of the eigenspectrum of the Hamilton matrix of the system $H_{\text{sys}(L+1)}$.

$$\left| \{m_L \sigma\}_k \right\rangle \to \sum_{\nu}^{D_b} \left| \psi^{(\nu)} \right\rangle\!\!\left\langle \psi^{(\nu)} \right| \cdot \left| \{m_L \sigma\}_k \right\rangle, \tag{4.26}$$

If the sum would run over $D_b D_s$ instead, the transformation would be unitary and both sides would equal. The Fock space of the system is rotated to a smaller Fock space which

becomes the new Fock space of the enlarged block

$$\mathcal{F}_{\mathrm{sys}(L+1)} = \mathrm{span}\left\{ \left| \{m_L\sigma\}_k \right\rangle \right\} \quad \rightarrow \quad \mathcal{F}_{b(L+1)} = \mathrm{span}\left\{ \left| \{m_{L+1}\}_{k'} \right\rangle \right\}, \quad (4.27)$$

$$\dim \mathcal{F}_{\mathrm{sys}(L+1)} = D_b \cdot D_s \quad \rightarrow \quad \dim F_{b(L+1)} = D_b. \quad (4.28)$$

Formally, Eqs. (4.26) to (4.28) define a non-unitary basis transformation. Obviously some information is lost during the transformation. In the NRG algorithm, the transformation matrices are built from the D_b eigenstates of the system Hamiltonian with the smallest energy eigenvalues, if we target the lower end of the spectrum. There are different possibilities to run through the index ν in Eq. (4.26). Either, strictly the first D_b eigenvectors are used for the basis transformation, or the first eigenvectors with respect to each subspace of total particle numbers are used for the basis transformation. We will discuss this issue in detail in Section 4.6.

For the sake of clarity, the renormalization procedure is illustrated in Figure 4.3. The transformation matrix $\mathcal{O}$ is defined via the coefficients $c_k^{(\nu)}$ from Eq. (4.25)

$$\mathcal{O}^{\nu k} = \left\langle \{m_L\sigma\}_k \mid \{m_{L+1}\}_\nu \right\rangle = \left\langle \{m_L\sigma\}_k \mid \psi^{(\nu)} \right\rangle = c_k^{(\nu)} \quad (4.29)$$

and has also a block structure. Again, each block corresponds to a subspace of a fixed total particle number.

The Hamilton matrix of the system becomes the new Hamilton matrix of the block which is now enlarged by one site

$$\mathcal{O}^T H_{\mathrm{sys}(L+1)} \mathcal{O} = H_{b(L+1)}, \quad (4.30)$$

$$H_{\mathrm{sys}(L+1)} \in \mathbb{C}^{D_b D_s \times D_b D_s} \quad \rightarrow \quad H_{b(L+1)} \in \mathbb{C}^{D_b \times D_b}. \quad (4.31)$$

The same applies to the creation and annihilation matrices of the newly attached site which now become the creation and annihilation matrices of rightmost end of the block:

$$\mathcal{O}^T \underbrace{a}_{\mathrm{site}} \mathcal{O} = \underbrace{a_{(L+1)}}_{\mathrm{block}}, \quad (4.32)$$

$$\mathcal{O}^T \underbrace{a^\dagger}_{\mathrm{site}} \mathcal{O} = \underbrace{a^\dagger_{(L+1)}}_{\mathrm{block}}, \quad (4.33)$$

$$a, a^\dagger \in \mathbb{C}^{D_b D_s \times D_b D_s} \quad \rightarrow \quad a_{(L+1)}, a^\dagger_{(L+1)} \in \mathbb{C}^{D_b \times D_b}. \quad (4.34)$$

The other creation and annihilation matrices of the block are no longer necessary, because the Hamiltonain couples to adjacent sites only. Using Eq. (4.29) the matrix elements of

Figure 4.3: Illustration of a renormalization step. The square brackets denote a subspace with conserved particle number. The dotted lines correspond to the non-unitary basis transformation for each subspace via the corresponding blocks of the matrix $\mathcal{O}$. In order to keep the filling factor constant, the subspaces have to be shifted accordingly. Note that the corresponding subspaces in the block and the system have different dimensions.

the new block are given by:

$$H_{b(L+1)}^{kk'} \;=\; \sum_{ll'=1}^{D_b D_s} (c_l^{(k')})^* \, H_{\text{sys}(L+1)}^{ll'} \, c_{l'}^{(k)} \,, \tag{4.35}$$

$$a_{(L+1)}^{kk'} \;=\; \sum_{ll'=1}^{D_b D_s} (c_l^{(k')})^* \, a^{ll'} \, c_{l'}^{(k)} \,, \tag{4.36}$$

$$\left(a_{(L+1)}^\dagger\right)^{kk'} \;=\; \sum_{ll'=1}^{D_b D_s} (c_{l'}^{(k)})^* \, (a^\dagger)^{ll'} \, c_l^{(k')} \,, \tag{4.37}$$

Now we have a block extended by one additional site, and start over attaching the next site to form the new system until we reach the final, desired length I of the lattice.

In summary, the recipe for the iterative NRG growing procedure reads:

(*i*) Initial step: Calculate and store $H_{b(L)}, a_L, a_L^\dagger$ and $H_s, a, a^\dagger$ for a moderate length L of the block and N_{max} particles per site. Store the dimensions of the subspaces for the different particle numbers in a vector $\vec{n}$.

(*ii*) Combine block and site to build $H_{\text{sys}(L+1)}$ for all subspaces of total particle numbers ranging from $N = N_{\text{min}}$ to $N = N_{\text{max}}$.

(*iii*) Diagonalize $H_{\text{sys}(L+1)}$ for each subspace of total particle numbers N

$$H_{\text{sys}(L+1)} \, \vec{c}^{(\nu)} = E^{(\nu)} \, \vec{c}, \quad \text{and} \quad E^{(\nu)} \le E^{(\nu+1)} \,, \tag{4.38}$$

and store the eigenvectors $\vec{c}^{(\nu)} = \sum_k \langle \, \{m_L \sigma\}_k \mid \psi^{(\nu)} \, \rangle \in \mathbb{C}^{D_b D_s}$.

(*iv*) For each subspace of total particle numbers from $H_{\text{sys}(L+1)}$, take n_k eigenvectors and form the rectangular transformation matrix $\mathcal{O} \in \mathbb{C}^{D_b \times D_b D_s}$.

(*v*) Rotate and truncate the system Hamilton matrix and the matrices $a, a^\dagger$ of the new site in order to build the new block Hamilton matrix and the matrices $a_L, a_L^\dagger$ of the block via the transformation matrix $\mathcal{O}$:

$$\mathcal{O}^T \, H_{\text{sys}(L+1)} \, \mathcal{O} \;=\; H_{b(L+1)} \,, \tag{4.39}$$

$$\mathcal{O}^T \underbrace{a}_{\text{site}} \mathcal{O} \;=\; \underbrace{a_{(L+1)}}_{\text{block}} \,, \tag{4.40}$$

$$\mathcal{O}^T \underbrace{a^\dagger}_{\text{site}} \mathcal{O} \;=\; \underbrace{a_{(L+1)}^\dagger}_{\text{block}} \,, \tag{4.41}$$

$$H_{\text{sys}(L+1)}, a, a^\dagger \in \mathbb{C}^{D_b D_s \times D_b D_s} \;\rightarrow\; H_{b(L+1)}, a_{(L+1)}, a_{(L+1)}^\dagger \in \mathbb{C}^{D_b \times D_b} \tag{4.42}$$

increase L by one, and start over with (*ii*).

The question, whether the choice of the new basis for the enlarged block, i.e. the eigenvectors of H_{sys}, is reasonable has not yet been answered. Intuitively, one may be tempted to agree and assume that an eigenbasis for a system of size L could be also a good eigenbasis for a system of size $L + 1$. But this can be easily disproven [50]. Consider a single particle in a box. After the diagonalization of the system Hamiltonian, the wavefunction has a specific value at the (right) boundary. It has to tend continuously to zero and vanish at the boundary. The addition of a new site beyond the right boundary of the system is in contradiction to the previous behavior of the wavefunction, because a finite value of the wavefunction at this point is now required. When periodic boundary conditions are applied this problem emerges on both boundaries of the system. In most cases this, problem leads to poor convergence of the NRG algorithm. Convergence can be dramatically improved by using a combination of boundary conditions [50], but the provisionary character of this solution is unsatisfying. Fortunately, the infinite-size density-matrix renormalization group algorithm can do much better.

4.5   Infinite-Size DMRG

The infinite-size density-matrix renormalization-group (DMRG) algorithm was developed as a successor of the NRG algorithm. The boundary problem of the wavefunction in the NRG algorithm, discussed in the previous section, reveals a more fundamental issue. Taking states from the lower end spectrum of the Hamiltonian as a transformation matrix lacks a formal motivation. It would be much more satisfying to have strict mathematical arguments at hand. White showed that the eigensystem of the reduced density-matrix defines an optimal basis that provides the best approximation to the wavefunction as well as to expectation values of observables [51, 44]. To this end, DMRG introduces some intermediate steps which will be introduced in the following. For a comprehensive introduction to DMRG and its applications we recommend Ref. [45, 46].

In contrast to the NRG method, we add a new step prior to the non-unitary basis transformation and embed the system in an auxiliary *environment* in order to mimic the thermodynamic limit. As an immediate improvement compared to NRG, the wavefunction of the system does not have to readjust to changes of the boundaries when the next lattice site is appended.
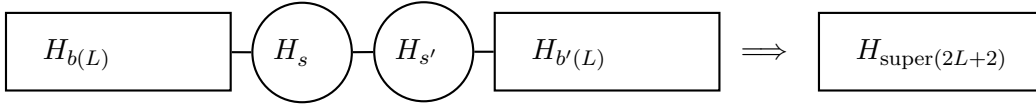
Figure 4.4: Combining system and environment to form the superblock.

We start by appending an additional site and an additional block to the system according to Section 4.3 to form the so-called *superblock*, as illustrated in Figure 4.4. This new superblock of length $2L + 2$ is described by the tensor product of four Fock spaces:

$$\mathcal{H}_{\text{super}(2L+2)} = \underbrace{\mathcal{F}_{b(L)} \otimes \mathcal{F}_s}_{\mathcal{F}_{\text{sys}(L+1)}} \otimes \underbrace{\mathcal{F}_{s'} \otimes \mathcal{F}_{b'(L)}}_{\mathcal{F}_{\text{env}(L+1)}} . \tag{4.43}$$

Furthermore, we project onto a fixed total particle number N which in our case is chosen to guarantee commensurate filling $N/(2L + 2) = 1$. Due to the projection, the basis of the superblock is smaller than the product of the basis dimensions of system and environment, $D_{\text{super}} < (D_b D_s)^2$.

In terms of Fock-states we describe the system via

$$\big| \{m_L\}_k \big\rangle \in \mathcal{F}_{b(L)} , \tag{4.44}$$

$$\big| \{\sigma\}_k \big\rangle \in \mathcal{F}_s , \tag{4.45}$$

$$\big| \{m_L\}_k \big\rangle \otimes \big| \{\sigma\}_l \big\rangle \equiv \big| \{m_L\sigma\}_n \big\rangle \in \mathcal{F}_{\text{sys}(L+1)} . \tag{4.46}$$

The respective dimensions are $\dim \mathcal{F}_{b(L)} = D_b$, $\dim \mathcal{F}_s = D_s$, and $\dim \mathcal{F}_{\text{sys}(L+1)} = D_b D_s$. For the environment we use

$$\big| \{\tilde{m}_L\}_k \big\rangle \in \mathcal{F}_{b'(L)} , \tag{4.47}$$

$$\big| \{\tilde{\sigma}\}_k \big\rangle \in \mathcal{F}_{s'} , \tag{4.48}$$

$$\big| \{\tilde{m}_L\}_k \big\rangle \otimes \big| \{\tilde{\sigma}\}_l \big\rangle \equiv \big| \{\tilde{m}_L\tilde{\sigma}\}_n \big\rangle \in \mathcal{F}_{\text{env}(L+1)} , \tag{4.49}$$

with dimensions $\dim \mathcal{F}_{b'(L)} = D_{b'}$, $\dim \mathcal{F}_{s'} = D_{s'}$, and $\dim \mathcal{F}_{\text{env}(L+1)} = D_{b'} D_{s'}$. The Hilbert space of the superblock is given by

$$\big| \{m_L\sigma\}_k \big\rangle \otimes \big| \{\tilde{m}_L\tilde{\sigma}\}_l \big\rangle \equiv \big| \{m_L\sigma\,\tilde{m}_L\tilde{\sigma}\}_n \big\rangle \in \mathcal{H}_{\text{super}(2L+2)} \tag{4.50}$$

and has a dimension $\dim \mathcal{H}_{\text{super}(2L+2)} = D_{\text{super}}$

In analogy to Eq. (4.20), a matrix element of the superblock

$$\langle \{m_L\}_k \mid \langle \{\sigma\}_l \mid \langle \{\tilde{m}_L\}_n \mid \langle \{\tilde{\sigma}\}_o \mid \hat{H}_{\text{super}(2L+2)} \mid \{m_L\}_{k'} \rangle \mid \{\sigma\}_{l'} \rangle \mid \{\tilde{m}_L\}_{n'} \rangle \mid \{\tilde{\sigma}\}_{o'} \rangle$$

reads

$$
\begin{aligned}
H^{kk'll'nn'oo'}_{\text{super}(2L+2)} &= H^{kk'}_{b(L)} \cdot \delta_{ll'}\delta_{nn'}\delta_{oo'} + H^{kk'll'}_{b(L)-s} \cdot \delta_{nn'}\delta_{oo'} \\
&\quad + H^{ll'nn'}_{s-s'} \cdot \delta_{kk'}\delta_{oo'} \\
&\quad + H^{nn'oo'}_{s'-b'(L)} \cdot \delta_{kk'}\delta_{ll'} + H^{oo'}_{b'(L)} \cdot \delta_{kk'}\delta_{ll'}\delta_{nn'}
\end{aligned}
\tag{4.51}
$$

After the Hamilton matrix is evaluated, one has to solve the eigenvalueproblem yielding the groundstate of the superblock of length $2L + 2$ with N particles:

$$
\begin{aligned}
\hat{H}_{\text{super}(2L+2)} \mid \psi^{(0)} \rangle &= E^{(0)} \mid \psi^{(0)} \rangle, \tag{4.52} \\
&= \sum_{kl} C^{(0)}_{kl} \mid \{m_L\sigma\}_k \rangle \otimes \mid \{\tilde{m}_L\tilde{\sigma}\}_l \rangle. \tag{4.53}
\end{aligned}
$$

Typically, the dimensions of the eigenvalue problems are about $D_{\text{super}} \approx 10^3 - 10^4$ for all calculations done in this work. We deal with sparse matrices and usually need the ground state or the first excited state only, therefore, we can employ efficient Lanczos-type algorithms [34]. Instead of using the eigensystem of H_{sys} as a new basis for the block like we did in NRG, we take advantage of the additional environment. By tracing out the environment we obtain the reduced density-matrix and information from beyond the boundary of the system is included:

$$
\begin{aligned}
\hat{\rho}^{\text{red}} &= \text{Tr}_{\text{env}} \left(\mid \psi^{(0)} \rangle\langle \psi^{(0)} \mid \right), \\
&= \sum_{l''} \langle \{\tilde{m}_L\tilde{\sigma}\}_{l''} \mid \left(\mid \psi^{(0)} \rangle\langle \psi^{(0)} \mid \right) \mid \{\tilde{m}_L\tilde{\sigma}\}_{l''} \rangle, \tag{4.54} \\
&= \sum_{l''} \sum_{kk'} \left(C^{(0)}_{kl''} \right)^* C^{(0)}_{k'l''} \mid \{m_L\sigma\}_k \rangle\langle \{m_L\sigma\}_{k'} \mid.
\end{aligned}
$$

Note that due to the trace, $\hat{\rho}^{\text{red}}$ is again element of the Fock space with a block diagonal form resulting from the different total particle numbers. For more information about the density matrix and its important features for the DMRG algorithm we refer to Section 4.1. In order to preserve a maximum amount of information from the system, we use the eigensystem of the reduced density matrix

$$
\begin{aligned}
\hat{\rho}^{\text{red}} \mid w^{(\alpha)} \rangle &= w^{(\alpha)} \mid w^{(\alpha)} \rangle, \qquad w^{(\alpha)} \geq w^{(\alpha+1)}, \tag{4.55} \\
\mid w^{(\alpha)} \rangle &= \sum_{i=1}^{D_b D_s} W^{(\alpha)}_i \mid \{m_L\sigma\}_i \rangle. \tag{4.56}
\end{aligned}
$$

as a new basis for the new block. Note, that the ordering of the eigenstates with respect to the eigenvalues is necessary in the following. In analogy to Eq. (4.26) we transform the system to the new block via a non-unitary transformation:

$$
\big|\,\{m_L\sigma\}_k\,\big\rangle \;\;\rightarrow\;\; \sum_\alpha^{D_b} \big|\,w^{(\alpha)}\,\big\rangle\!\big\langle\,w^{(\alpha)}\,\big|\cdot\big|\,\{m_L\sigma\}_k\,\big\rangle\;, \quad (4.57)
$$

$$
\mathrm{span}\,\big\{\,\big|\,\{m_L\sigma\}_k\,\big\rangle\big\} = \mathcal{F}_{\mathrm{sys}(L+1)} \;\;\rightarrow\;\; \mathrm{span}\,\big\{\,\big|\,\{m_{L+1}\}_{k'}\,\big\rangle\big\} = \mathcal{F}_{b(L+1)}\;, \quad (4.58)
$$

$$
\dim \mathcal{F}_{\mathrm{sys}(L+1)} = D_b\cdot D_s \;\;\rightarrow\;\; \dim F_{b(L+1)} = D_b\;. \quad (4.59)
$$

The basis transformation would be unitary if the sum in (4.57) ran up to $D_b D_s$. Again, there are different possibilities to run through the index ν in Eq. (4.57). Either, strictly the first D_b eigenvectors are used for the basis transformation, or the first eigenvectors with respect to each subspace of total particle numbers are used for the basis transformation. We will discuss this issue in detail in Section 4.6.

The matrix elements of the transformation matrix $\mathcal{O}$ are the expansion coefficients in Eq. (4.56)

$$
\mathcal{O}^{\alpha k} = \big\langle\,\{m_L\sigma\}_k\,\big|\,\{m_{L+1}\}_\alpha\,\big\rangle = \big\langle\,\{m_L\sigma\}_k\,\big|\,w^{(\alpha)}\,\big\rangle = W_k^{(\alpha)}\;. \quad (4.60)
$$

We use the transformation matrix $\mathcal{O}$ to calculate the Hamilton matrix of the new block from the Hamilton matrix of the system

$$
\mathcal{O}^T\,H_{\mathrm{sys}(L+1)}\,\mathcal{O} \;\;=\;\; H_{b(L+1)}\;, \quad (4.61)
$$

$$
H_{\mathrm{sys}(L+1)}\in\mathbb{C}^{D_bD_s\times D_bD_s} \;\;\rightarrow\;\; H_{b(L+1)}\in\mathbb{C}^{D_b\times D_b}\;. \quad (4.62)
$$

Accordingly we obtain for the matrices for the rightmost site of the new block from the matrices from the site

$$
\mathcal{O}^T\,\underbrace{a}_{\text{site}}\,\mathcal{O} \;\;=\;\; \underbrace{a_{(L+1)}}_{\text{block}}\;, \quad (4.63)
$$

$$
\mathcal{O}^T\,\underbrace{a^\dagger}_{\text{site}}\,\mathcal{O} \;\;=\;\; \underbrace{a^\dagger_{(L+1)}}_{\text{block}}\;, \quad (4.64)
$$

$$
a,a^\dagger\in\mathbb{C}^{D_bD_s\times D_bD_s} \;\;\rightarrow\;\; a_{(L+1)},a^\dagger_{(L+1)}\in\mathbb{C}^{D_b\times D_b}\;. \quad (4.65)
$$

The explicit expressions for the matrix elements are

$$H_{b(L+1)}^{kk'} = \sum_{ll'=1}^{D_b D_s} (W_l^{(k')})^* H_{\mathrm{sys}(L+1)}^{ll'} W_{l'}^{(k)}, \tag{4.66}$$

$$a_{(L+1)}^{kk'} = \sum_{ll'=1}^{D_b D_s} (W_l^{(k')})^* a^{ll'} W_{l'}^{(k)}, \tag{4.67}$$

$$\left(a_{(L+1)}^{\dagger}\right)^{kk'} = \sum_{ll'=1}^{D_b D_s} (W_{l'}^{(k)})^* (a^{\dagger})^{ll'} W_l^{(k')}, \tag{4.68}$$

where k, k' run over the block basis and l, l' over the system basis.

Now we are able to summarize the infinite-size DMRG algorithm. The individual steps are schematically depicted in Figure 4.5.

(*i*) Initial step: Calculate $H_{b(L)}, a_L, a_L^{\dagger}$ and $H_s, a, a^{\dagger}$ for a moderate size L of the block and N_{max} particles per site (typically $N_{\mathrm{max}} = 4$ to 6). Store the dimensions of the subspaces for the different total particle numbers (more generally, for conserved quantum numbers) in a vector $\vec{n}$.

(*ii*) Combine block and site to build $H_{\mathrm{sys}(L)}$ for all subspaces of total particle numbers ranging from $N = N_{\mathrm{min}}$ to $N = N_{\mathrm{max}}$.

(*iii*) Proceed in the same manner to build the auxiliary environment $H_{\mathrm{env}(L)}$. Use the mirrored system for the environment, if the Hamiltonian is translation invariant.

(*iv*) Build the superblock $H_{\mathrm{super}(2L+2)}$ from system and environment and project onto a fixed total particle number N.

(*v*) Diagonalize $H_{\mathrm{super}(2L+2)}$ (usually only the ground state is needed).

$$H_{\mathrm{super}(2L+2)} \, \vec{C}^{(0)} = E^{(0)} \, \vec{C}^{(0)} \tag{4.69}$$

$$C_{kl}^{(0)} = \left(\langle \, \{m_L \sigma\}_k \, | \otimes \langle \, \{\tilde{m}_L \tilde{\sigma}\}_l \, | \right) | \, \psi^{(0)} \, \rangle \tag{4.70}$$

(*vi*) Construct the reduced density-matrix

$$\rho_{kk'}^{\mathrm{red}} = \sum_l \left(C_{kl}^{(0)} \right)^* C_{k'l}^{(0)}. \tag{4.71}$$

Note that the density matrix is block diagonal within each subspace of particle numbers N. Calculate its eigensystem for each subspace.

$$\rho^{\mathrm{red}} \vec{W}^{(\alpha)} = w^{(\alpha)} \vec{W}^{(\alpha)} \quad \text{with} \quad w^{(\alpha)} \geq w^{(\alpha+1)}. \tag{4.72}$$
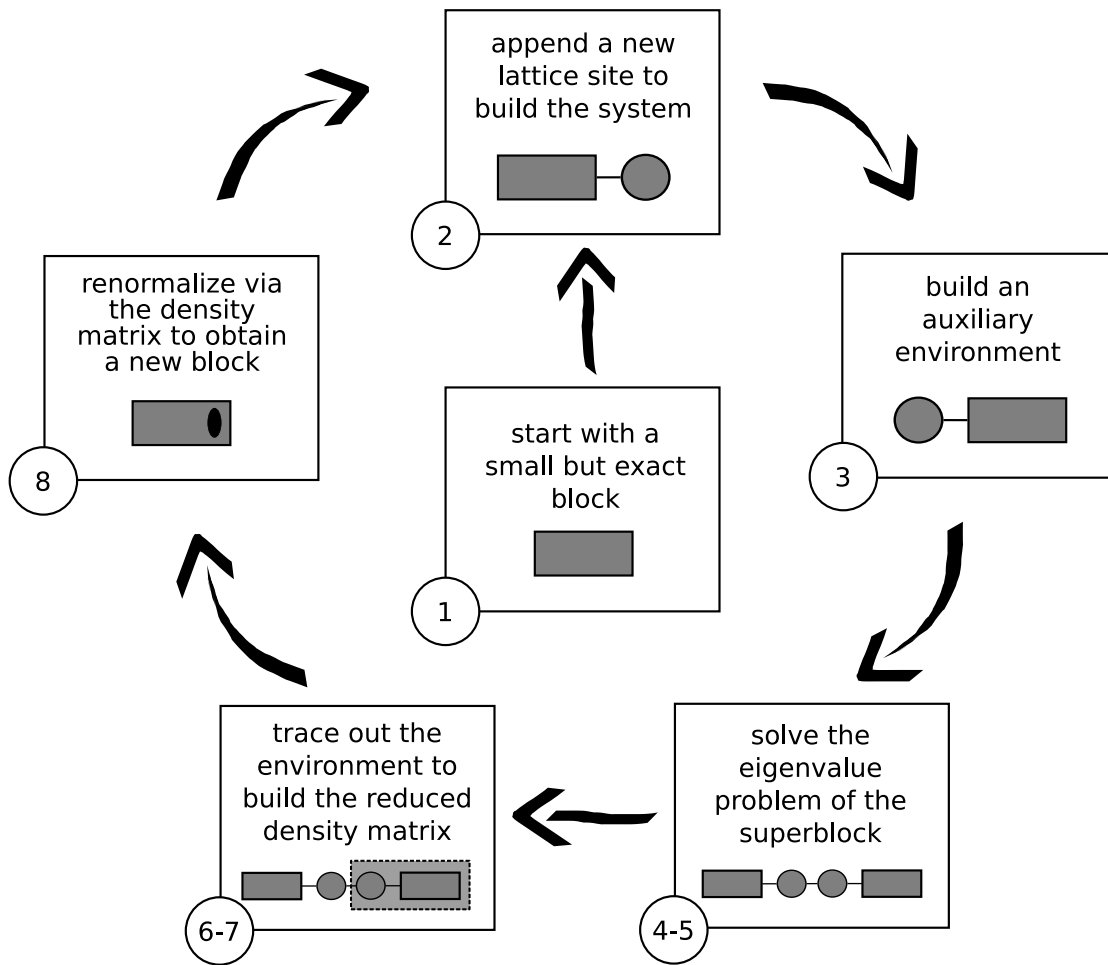
Figure 4.5: Sketch of the DMRG algorithm. The cycle is repeated until the desired length of the lattice is reached. The black dot in step 8 depicts a block that is enlarged by one site but whose basis has the same dimension as before the enlargement.

(*vii*) For each subspace j take n_j eigenvectors and form the rectangular transformation matrix $\mathcal{O} \in \mathbb{C}^{D_b \times D_b D_s}$ via

$$\mathcal{O}^{\alpha k} = \left\langle \, \{m_L \sigma\}_k \mid w^{(\alpha)} \, \right\rangle = W_k^{(\alpha)} \,. \tag{4.73}$$

(*viii*) Transform and truncate the system Hamiltonian and the matrices $a, a^\dagger$ of the new site in order to build the new block Hamiltonian and the new exit-entry-terms of the block via the rectangular transformation matrix $\mathcal{O}$

$$\mathcal{O}^T \, H_{\text{sys(L+1)}} \, \mathcal{O} \;=\; H_{b(L+1)} \tag{4.74}$$

$$\mathcal{O}^T \underbrace{a}_{\text{site}} \mathcal{O} \;=\; \underbrace{a_L}_{\text{block}} \tag{4.75}$$

$$\mathcal{O}^T \underbrace{a^\dagger}_{\text{site}} \mathcal{O} \;=\; \underbrace{a_L^\dagger}_{\text{block}} \tag{4.76}$$

$$(H_{\text{sys(L+1)}}, a, a^\dagger) \in \mathbb{C}^{D_b D_s \times D_b D_s} \;\;\rightarrow\;\; (H_{b(L)}, a_L, a_L^\dagger) \in \mathbb{C}^{D_b \times D_s} \,. \tag{4.77}$$

Increase L and step by one and start over with (*ii*).

Although the infinite-size DMRG algorithm gives much better approximations to the exact ground state than the NRG algorithm does, there is still room for improvement as we will see in the next section.

4.6 Finite-Size DMRG

For homogeneous lattices the infinite-size DMRG algorithm already yields very accurate results, but we are mostly interested in inhomogeneous lattices. As soon as the translational invariance is broken, the reliability of the infinite-size DMRG algorithm deteriorate rapidly because the Hamiltonian does not know about the complete topology of the lattice until the very last step of the algorithm, when the final length of the lattice is reached. Fortunately, we can overcome this problem by applying the finite-size DMRG algorithm [44] introduced in the following.

The starting point is a preceding run from the infinite-size algorithm until the desired length I of the lattice is reached. During this run, one has to store the block matrices $(H_{b(L)}, a_L, a_L^\dagger)$ for each intermediate length L of the system and the environment. The finite-size algorithm keeps the size of the lattice fixed and continues the DMRG cycle while the system grows on the expense of the environment and vice versa. Basis rotations are only performed for the currently growing part. Starting at the center, we first
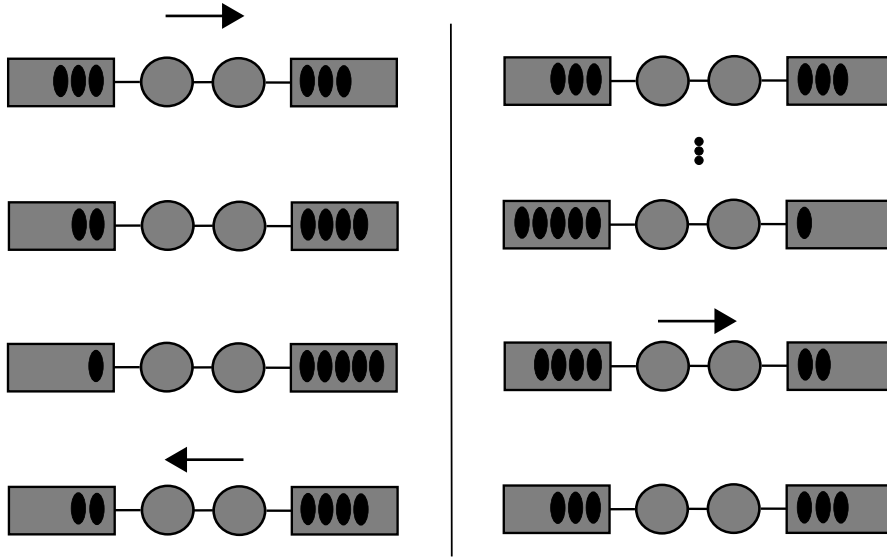
Figure 4.6: Sketch of one sweep in the finite-size DMRG algorithm. The dimension of the block stays constant, while the number of included sites varies. The point of return may also be reached earlier when more sites are left in the block. This depends on the sites included in the block at the very first step of the infinite-size algorithm where it was represented in the occupation-number basis.

approach the right boundary of the lattice, rebound and go back to the left boundary, rebound again and end at the center where we started. This whole process is called a *sweep* and is illustrated in Figure 4.6. Thereby, the Hamiltonian always accounts for the whole lattice and can successively sample the topology of the lattice during the sweeps. This is done until the ground-state energy and the observables converge.

As a final remark, we would like to mention that the way the reduced density-matrix is constructed is not strictly defined by the DMRG algorithm [see Eq. (4.57)]. One can either use the eigenvectors from the largest eigenvalues in each subspace of the system with conserved particle number. In this case, the subspaces in the square brackets in Figure 4.3 keep their dimension. Or one can strictly use the first D_b eigenvectors of the reduced density-matrix with the largest eigenvalues which may change the dimensions of the subspaces in Figure 4.3. In the first case it is possible to discard eigenvectors with sizeable eigenvalues if the dimension of the respective subspace is already reached. In the second case one could possibly discard a complete subspace if it has no eigenvectors with an eigenvalue among the largest D_b eigenvalues. If in a subsequent step this

subspace becomes important again, the algorithm might convergence to a metastable state. Lost subspaces can be regained by adding noise to the transformation matrices $\mathcal{O}$ during the first few sweeps of the finite-size algorithm [52]. A third strategy is a hybrid of the two others. Here, one keeps at least one or a few states from each subspace. This preserves more relevant information without the risk of loosing a complete subspace.

For all calculations presented in this work, we choose the first strategy for it is technically very convenient. We have randomly checked eigenspectra of ρ^{red} for discarded eigenvectors with sizable eigenvalues. This was never the case for the bases we used in our calculations of the phase diagrams.

4.7   Observables

So far, we have only discussed how the ground-state energy is obtained from the DMRG calculations. Although the approximate ground state is a result of the DMRG algorithm, the calculation of observables is not straight forward. After the first basis rotation in the beginning of the infinite-size algorithm, we loose access to the individual lattice sites within the block. The Hilbert space of the block is no longer spanned by the occupation-number representation, but by a truncated eigenbasis of the reduced density-matrix. This results in a rather complicated process of calculating observables in the DMRG framework.

Our gateway to the calculation of observables are the newly attached sites within the system and the environment because they are always expressed in the occupation-number representation. All observables are evaluated in the final sweep of the finite-size algorithm. For the sake of clarity we consider a concrete example in the following. Let us assume we just reached the left boundary of the lattice. This situation corresponds to the picture with the arrow, on the right panel of Figure 4.6. Furthermore, we assume to be interested in an element of the onebody density-matrix $\rho_{ij}^{(1)} = \left\langle a_j^\dagger a_i \right\rangle$ and $i < j < L/2$, i.e. both matrices $a_j^\dagger$ and a_i are in the system which now starts growing on the expense of the environment. We evaluate the matrix representation of the operator $\hat{a}_i$ as soon as it is lives in the subspace of the newly attached site:

$$a_i^{mn} = \left\langle \, \{m_{i-1}\sigma\}_m \, \big| \, \hat{a}_i \, \big| \, \{m_{i-1}\sigma\}_n \, \right\rangle. \qquad (4.78)$$

Since we have to label the same operator in different bases in the following, we introduce a notation for the full matrix of the operator expressed in a particular basis: when the

indices are left away, we mean the full matrix representation in the system basis where the system has the length i

$$\left\langle \, \{m_{i-1}\sigma\} \, \middle| \, \hat{a}_i \, \middle| \, \{m_{i-1}\sigma\} \, \right\rangle \equiv \left(\, \left\langle \, \{m_{i-1}\sigma\}_m \, \middle| \, \hat{a}_i \, \middle| \, \{m_{i-1}\sigma\}_n \, \right\rangle \right)_{nm}. \tag{4.79}$$

The matrix representation of the operator has to be transformed from the system basis to the new block basis via the transformation matrix $\mathcal{O}$. To keep track of further transformations, we index the transformation matrices $\mathcal{O} \rightarrow \mathcal{O}_i$ for the individual growing steps. This leads to

$$\left\langle \, \{m_i\} \, \middle| \, \hat{a}_i \, \middle| \, \{m_i\} \, \right\rangle = \mathcal{O}_i^T \left\langle \, \{m_{i-1}\sigma\} \, \middle| \, \hat{a}_i \, \middle| \, \{m_{i-1}\sigma\} \, \right\rangle \mathcal{O}_i \tag{4.80}$$

Note, if there is a σ inside the curly brackets, we are in the system basis, else we are in the smaller block basis. After the next growing step we have to update the operator matrix

$$\left\langle \, \{m_{i+1}\} \, \middle| \, \hat{a}_i \, \middle| \, \{m_{i+1}\} \, \right\rangle = \mathcal{O}_{i+1}^T \left\langle \, \{m_i\sigma\} \, \middle| \, \hat{a}_i \, \middle| \, \{m_i\sigma\} \right\} \mathcal{O}_{i+1}. \tag{4.81}$$

We would like to emphasize that we still deal with the same operator, only the basis in which it is expressend has changed.

The update procedure is continued until $\hat{a}_j^\dagger$ can act on the newly attached site and we obtain

$$\left\langle \, \{m_j\} \, \middle| \, \hat{a}_j^\dagger \hat{a}_i \, \middle| \, \{m_j\} \, \right\rangle = \tag{4.82}$$
$$\mathcal{O}_j^T \left(\, \left\langle \, \{m_{j-1}\sigma\} \, \middle| \, \hat{a}_j^\dagger \, \middle| \, \{m_{j-1}\sigma\} \, \right\rangle \times \left\langle \, \{m_{j-1}\sigma\} \, \middle| \, \hat{a}_i \, \middle| \, \{m_{j-1}\sigma\} \, \right\rangle \right) \mathcal{O}_j.$$

Only in this growing step, $a_j^\dagger$ and a_i are represented in the same basis and the matrix multiplication can be evaluated. The compound object then has to be rotated

$$\left\langle \, \{m_{j+1}\} \, \middle| \, \hat{a}_i^\dagger \hat{a}_j \, \middle| \, \{m_{j+1}\} \, \right\rangle = \mathcal{O}_{j+1}^T \left(\, \left\langle \, \{m_j\sigma\} \, \middle| \, \hat{a}_i^\dagger \hat{a}_j \, \middle| \, \{m_j\sigma\} \, \right\rangle \right) \mathcal{O}_{j+1} \tag{4.83}$$

and updated further. In the very last step, the expectation value is evaluated with the final eigenstate $\left| \, \psi \, \right\rangle$ of the superblock

$$\left\langle \hat{a}_j^\dagger \hat{a}_i \, \right\rangle = \tag{4.84}$$
$$\left\langle \, \psi \, \middle| \, \{m_{L-1}\sigma \tilde{m}_{L-1}\tilde{\sigma}\} \, \right\rangle \left\langle \, \{m_{L-1}\sigma \tilde{m}_{L-1}\tilde{\sigma}\} \, \middle| \, \hat{a}_j^\dagger \hat{a}_i \, \middle| \, \{m_{L-1}\sigma \tilde{m}_{L-1}\tilde{\sigma}\} \, \right\rangle \left\langle \, \{m_{L-1}\sigma \tilde{m}_{L-1}\tilde{\sigma}\} \, \middle| \, \psi \, \right\rangle$$

If both operators are not in the same half of the lattice, e.g. $i < I/2$ and $j > L/2$ both are calculated according to Eq. (4.80) and then updated according to Eq. (4.81) when their part of the superblock is growing. The compound object is calculated not until the very last step of the infinite-size algorithm when the expectation value is evaluated.

If the operators act on the same site, e.g., $\hat{n}_i = \hat{a}_i^\dagger \hat{a}_i$, the compound object is calculated right in Eq. (4.80) and the procedure continues without Eq. (4.82).

In summary, we have to account for the basis rotations explicitly when calculating expectation values in the DMRG framework. In the very last sweep of the finite-size algorithm, we evaluate the matrices $(a_l^\dagger, a_l, n_l, n_l^2)$ at the step of the sweep in which site l is given in the occupation-number representation. These matrices have to be rotated in accordance with the basis of their block in each growing step. This means that all the multiplications with the transformation matrices $\mathcal{O}$ in Eq. (4.80) have to be performed. At the very last step of the finite-size algorithm, the expectation values are evaluated with the obtained ground state. In practice, this procedure is numerically very involved since all matrices for each observable have to be processed in the final sweep and undergo all basis rotations.

There is a second strategy for the local observables, e.g., n_i and n_i^2. The expectation values of these observables can be evaluated directly when their matrix representation is calculated. In this case, observables at different sites are evaluated with slightly different ground states, but one saves the effort of carrying on the additional non-unitary transformations. If one assumes the ground state has already converged when the expectation values are calculated, there should be no difference between the two methods. We have always compared both methods in all our calculations and found very small deviations between the results.

4.8 Excited States

The DMRG algorithm uses the eigenstates of the reduced density-matrix as a new, truncated basis for the Hamiltonian and all operators of the system. Usually, the reduced density matrix is built from the ground state of the superblock. Therefore, the algorithm *targets* the groundstate of the physical system under consideration [see Eq. (4.54)]. Although the eigensystem solver can provide excited states, they might be poorly approximated. To improve on this, we have to target an excited state of interest explicitly

in a new individual DMRG run. If one is interested in several excited states, one can also use an equal weighted superposition the corresponding states from the lower end of the eigenspectrum to built the density matrix and perform a single DMRG run only. This provides a balance between computational effort and quality of the calculation and is the common procedure proposed in most publications, e.g., Ref. [45].

To obtain the energy gap, we need the energy expectation value of the first excited state. If we employ larger DMRG bases (e.g., DMRG-D or DMRG-E defined in Tab. 5.2) we found practically no difference of the energy gap when targeting explicitly the excited state and, therefore, spared the additional DMRG run for the calculations of the phase diagrams in Section 5.4.

4.9   Filling Factor N/I

In the present work we have only investigated DMRG calculations for systems with commensurate filling factor $N/I = 1$, where N is the number of particles and I the final length of the optical lattice. If other filling factors are of interest, one can calculate them with a slight modification of the DMRG algorithm. In Figure 4.3, where the renormalization step is depicted, one can see that the sub-matrices of the block are shifted by one to the direction of larger N when going from length L to $L+1$. So, the subspace corresponding to the smallest total particle number is dropped while a subspace with the largest total particle number is included. This procedure preserves the filling factor while the length of the lattice grows. Naturally, one can only project the superblock to an integer total particle number. For instance, in the case of the filling factor $1/2$ the total particle number of the superblock would be incremented in every second step of the algorithm. This scheme will eventually lead to a filling factor of $N/I = 1/2$. For other filling factors, one has to devise an appropriate scheme for shifting of the sub-matrices of the block and projection of the superblock to total particle numbers.

Chapter 5

DMRG Results

5.1   DMRG – Benchmark

At present, the density-matrix renormalization group (DMRG) algorithm is among the most powerful numerical methods to study low-dimensional and strongly correlated lattice systems. During the introduction of the DMRG algorithm, we emphasized that the renormalization step of the DMRG algorithm preserves a maximum on information about a state after the truncation of the many-body basis. However, the DMRG is still an approximative method. To get an impression about the quality of the approximation we can expect from DMRG calculations, we investigate how the DMRG algorithm behaves in different transition regimes of the phase diagram spanned by the generic Hubbard parameters. The physics of the different phases and their characteristics will be discussed in detail in Section 5.4.

We restrict ourselves to a small system of $I = N = 10$ lattice sites and particles, where benchmark calculations from exact diagonalization schemes, as introduced in Section 3, are available. DMRG calculations using three different truncated Hilbert spaces are compared to these exact results. Therefore, we will show results for observables obtained by the exact diagonalization scheme in the complete Hilbert space as well as the deviations from the corresponding DMRG calculations.

For an expectation value of an observable $\langle A \rangle$ the error of the DMRG result is de-

fined as:

$$\left\langle A \right\rangle^{err} = \left\langle A \right\rangle^{ex} - \left\langle A \right\rangle^{\mathrm{DMRG}} . \tag{5.1}$$

In order to emphasize the truncation error of the DMRG algorithm in this rather small lattice, we had to choose very small bases for the DMRG calculations. We employ three different basis sizes, each with a different maximum number of particles per lattice site $\max\{n_i\} = N_{\mathrm{b}} = N_{\mathrm{s}}$. In the complete Hilbert space $\max\{n_i\}$ equals the length of the lattice. The basis specifications are listed in Table 5.1.

We start with a run of the infinite-size DMRG algorithm which already takes the topology of the superlattice is into account. Then, we use three to six sweeps in the finite-size DMRG algorithm until all observables do not change any more and the calculations are converged.

Superfluid to homogeneous Mott-insulator transition ($\epsilon_{\mathrm{max}} = 0$):
We have already pointed out that in case of a homogeneous lattice, i.e., $\epsilon_{\mathrm{max}} = 0$, the Bose-Hubbard model exhibits a quantum phase transition from the superfluid to the Mott-insulating phase around $U/J \approx 5$. From the outset, we expect the DMRG to encounter significant errors in the weakly interacting superfluid phase. Here, even the basis states (2.26) with many of particles occupying the same site may contribute significantly to the ground state. In the DMRG calculations, however, we restrict the maximum occupation number $\max\{n_i\}$ as shown in Table 5.1. Furthermore, in the superfluid regime almost all of the basis states are important and thus the reduced density-matrix is not able to determine a distinct subspace of most important basis states of the system. Technically, this is reflected in a slow decrease of the eigenvalues of the reduced density-matrix and therefore, also important information is discarded by the non-unitray basis

	D_{b}	D_{s}	$\max\{n_i\}$	D_{super}
DMRG-A	10	40	3	258
DMRG-B	15	75	4	338
DMRG-C	21	126	5	446
			$\max\{n_i\}$	D
diagonalization			10	92378

Table 5.1: Basis specifications for the different DMRG calculations and for the exact diagonalization in the complete Hilbert space.

transformation in the renormalization step.

The results for the exact calculations are shown in the upper row of Figure 5.1. In the regime $U/J < 5$ the energy gap $\Delta E/J$ is almost zero and then increases linearly with U/J after the phase transition. The maximum number-fluctuation $\sigma_{\max}$, the condensate fraction f_c, and the visibility ν are all about one for very small U/J and decrease monotonically with increasing U/J.

The errors of the DMRG calculations are depicted in the lower row of Figure 5.1. For interaction energies $U/J < 3$, all three DMRG calculations show significant deviations for all observables. Calculations using the DMRG-B and DMRG-C basis provide an excellent approximation for values $U/J \geq 5$, where DMRG-A still yield poor results. Comparing the results of $\sigma_{\max}$, f_c, and ν obtained with the bases DMRG-A, DMRG-B, and DMRG-C we find that the DMRG calculations systematically underestimate these observables for $U/J < 5$. This feature is most prominent for the condensate fraction f_c because it relies most on a good description of the delocalization of particles that occurs in the superfluid regime. The delocalization is maximal if all particles occupy one single quasi-momentum eigenstate. Since we work in a localized Wannier basis, it would require the complete Hilbert space to describe maximal delocalization. The relative error of the visibility ν is surprisingly small, even for small interaction energies and the small DMRG-A basis. In homogeneous systems, the maximum of the interference pattern is in principle given by the occupation number of the Bloch function with quasi-momentum zero and the minimum corresponds to the occupation number of the highest quasi-momentum. If the occupation number for the highest quasi-momentum tends to zero, the visibility becomes one. Thus, although the DMRG cannot put all particles into the quasi-momentum zero state—this would require the complete, untruncated Hilbert space—it distributes them among the lowest quasi-momentum states, leaving the highest one almost empty, resulting in a good approximation of the visibility even in the superfluid regime.

For $U/J \geq 5$ we find a very small error for the two larger DMRG bases. In the smallest DMRG-A basis we only allow for $\max\{n_i\} = 3$. This seems to be too small to approximate the weakly interacting regime.

Homogeneous Mott-insulator to quasi Bose-glass transition $(U/J = 30)$:
In order to study the quality of DMRG calculations in irregular lattices, we fix the
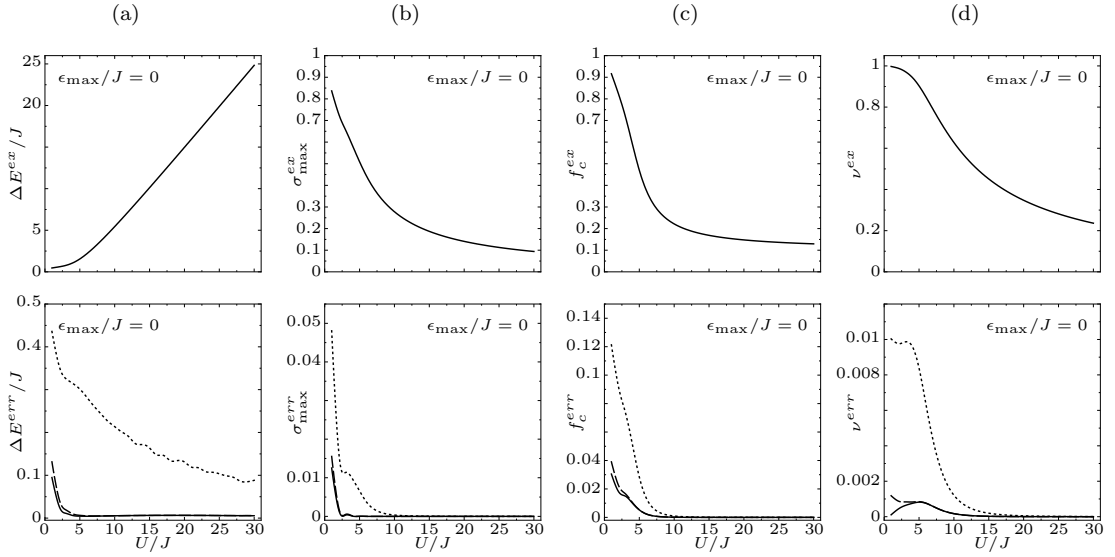
Figure 5.1: Observables for an $I = N = 10$ system along the superfluid to Mott-Insulator phase transition. Upper row: Results from exact diagonalization in a complete Hilbert space. Lower row: Absolute errors of DMRG calculations using the DMRG-A (dotted), DMRG-B (dashed), and DMRG-C (solid) bases. (a) energy gap ΔE, (b) maximum number fluctuation σ_{max}, (c) condensate fraction f_c, (d) visibility ν.

interaction strength at $U/J = 30$, and vary the strength of the superlattice potential ϵ_{max}/J. If both energies become about equal, the transition from the homogeneous Mott-insulator to the quasi Bose-glass phase occurs. The strong localization breaks down and particles are rearranged with respect to the topology of the superlattice. This leads to an increase of the number fluctuations and a vanishing energy gap at the point $U = \epsilon_{max}$ as shown in the upper row of Figure 5.2.

The corresponding results for the errors of the DMRG calculations are shown in Figure 5.2 as well. The energy gap exhibits a very small error for the whole range of ϵ_{max}/J. However, DMRG-B and DMRG-C show a larger error at $\epsilon_{max} = 0$ than at $\epsilon_{max}/J = 1$. This reveals a subtle feature of the DMRG algorithm. In the pure Mott-insulating phase ($\epsilon_{max} = 0$, $U/J > 5$), the first excited state is a superposition of multiple degenerate particle-hole excitations with respect to the number state with exactly one particle per site. An irregularity ($\epsilon_{max}/J > 0$) lifts this degeneracy and double occupancies in the deepest superlattice wells become favorable. This enables the reduced density-matrix to *select* a subspace of most important states from the system as the new basis of the block
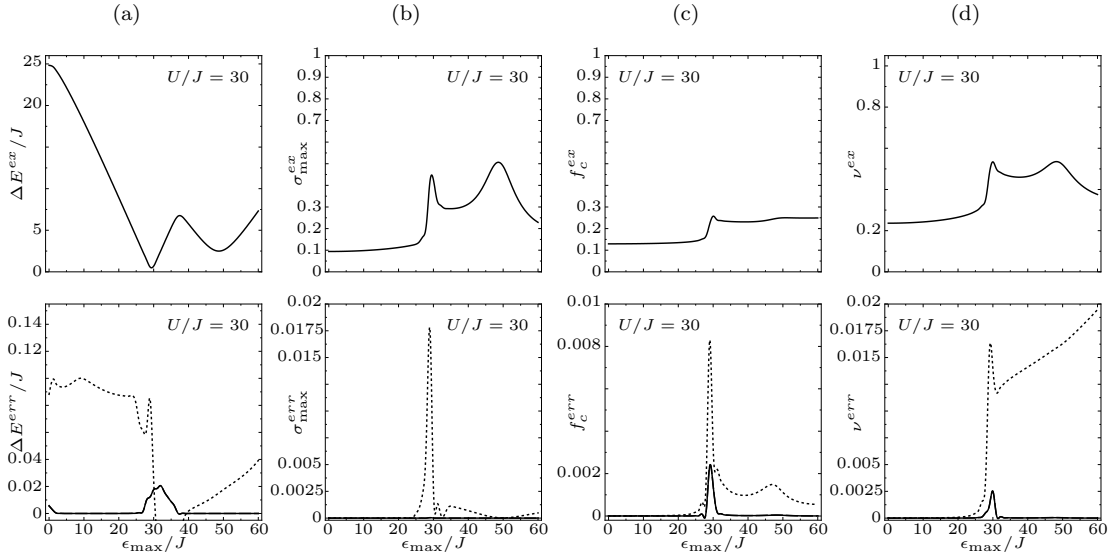
Figure 5.2: Observables for an $I = N = 10$ system along the Mott-insulator to quasi Bose-glass phase transition. Upper row: Results from exact diagonalization in a complete Hilbert space. Lower row: Absolute errors of DMRG calculations using the DMRG-A (dotted), DMRG-B (dashed), and DMRG-C (solid) bases. (a) energy gap ΔE, (b) maximum number fluctuation $\sigma_{\max}$, (c) condensate fraction f_c, (d) visibility ν.

leading to an improvement of the DMRG results. However, as soon as $\epsilon_{\max}$ roughly equals U more basis states become energetically degenerate in the first excited state and the error of $\Delta E/J$ increases again. For the other observables, DMRG-B and DMRG-C give very good approximations to the exact results for all superlattice strengths, even in the vicinity of the phase transition $U \approx \epsilon_{\max}$. Again, the small DMRG-A basis is not capable to give reliable results for all values of $\epsilon_{\max}$.

Localized to quasi Bose-glass phase transition ($\epsilon_{\max}/J = 50$):
Although we found that the localized phase is not accessible via a tuning of the intensities of the two lasers generating the optical superlattice, we examine the quality of the DMRG calculations in this regime to complete the discussion. In the limit of very small interaction energies $U/J \lesssim 3$, all particles in the optical lattice settle in the deepest wells. An increase of U/J quickly leads to an escape of one particle to the second deepest lattice well in order to reduce the rapidly growing interaction energy. A further increase leads to an escape of the next particle and so forth. This is accompanied by increases and decreases in ΔE, $\sigma_{\max}$, and ν as shown in the upper row of Figure 5.3.
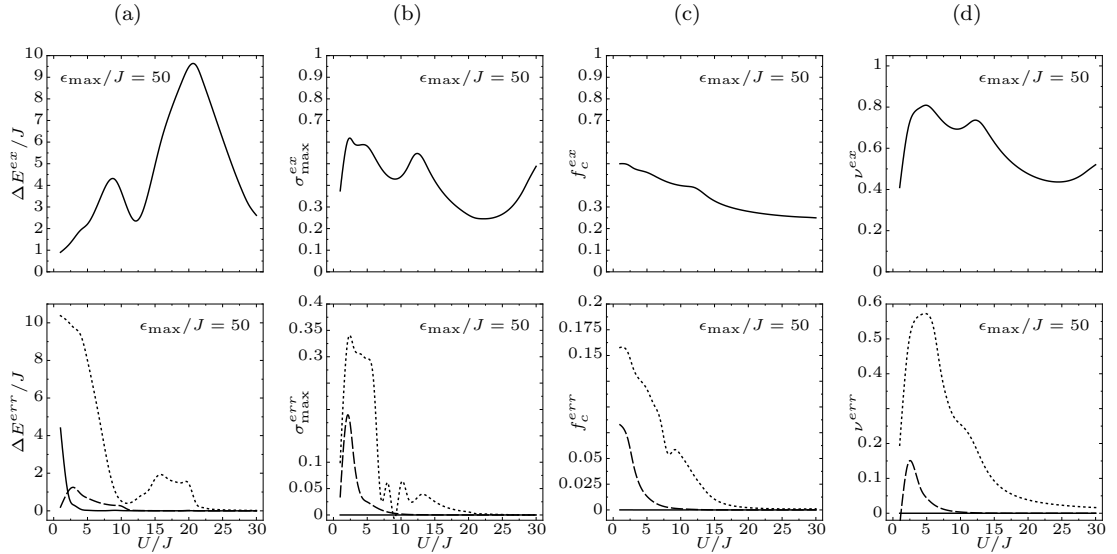
Figure 5.3: Observables for an $I = N = 10$ system along the localized to quasi Bose-glass phase transition. Upper row: Results from exact diagonalization in a complete Hilbert space. Lower row: Absolute errors of DMRG calculations using the DMRG-A (dotted), DMRG-B (dashed), and DMRG-C (solid) bases. (a) energy gap ΔE, (b) maximum number fluctuation $\sigma_{\max}$, (c) condensate fraction f_c, (d) visibility ν.

In our topology of the superlattice (see Fig. 3.1) there are two supercells and, thus, five particles in each of the deepest wells. In order to give reasonable approximations, the DMRG basis must at least allow for that maximum number of particles per lattice site $\max\{n_i\}$. The DMRG-A and DMRG-B bases are, therefore, not appropriate to describe this regime and produce large errors, as visible in the lower row of Figure 5.3. The DMRG-C basis fails only for the energy gap ΔE in the region $U/J < 3$. A reasonable explanation for this poor approximation in comparison to the smaller DMRG-B basis has yet to be found.

To conclude, the relevant transition regimes are very well described by DMRG calculations if the bases are chosen not to be too small. We observe that an increase of the DMRG bases dimensions leads to better results for all observables. We would like to emphasize again, that we chose very small DMRG bases on purpose, in order to see any deviations from the exact calculations in the first place.

In order to describe properties of the localized phase, it is necessary to provide the DMRG basis with a $\max\{n_i\}$ that at least equals the average number of particles per supercell to correctly describe a completely localized state. This is of course not feasible for incommensurate lattices or truly random lattices because the supercells are much larger in these cases, if they can be defined at all.

5.2   DMRG – Convergence

In order to check the results of our DMRG calculations for larger lattices, here $I = N = 30$, where no exact calculations in the complete Hilbert space are available, we follow the common procedure [45]. For a fixed set of parameters, DMRG calculations are performed with bases of increasing size. If the results for all observables do not change while the basis size is increased, the calculation is assumed to be converged to the exact result. The different basis sets we employ are summarized in Table 5.2. In all calculations we apply three to six sweeps in the finite-size algorithm until we achieve convergence.

Superfluid to homogeneous Mott-insulator transition ($\epsilon_{\max} = 0$):
The upper row in Figure 5.4 shows the observables for the superfluid to Mott-insulator transition. The energy gap is slightly larger in the calculations using the DMRG-C basis, while curves for DMRG-D and DMRG-E match perfectly. In comparison to the other observables, where all curves match perfectly for $U/J > 3$, this is again an indication of the difficulties the DMRG algorithm has as soon as many degenerate basis states become important, which is the case for the first excited state in this regime. For smaller values $U/J < 3$, the only sizable difference occurs for the condensate fraction f_c at $U/J \approx 1$ due to the delocalization of particles as already discussed in the previous section.

Localized to quasi Bose-Glass phase transition ($\epsilon_{\max}/J = 50$):
In the previous section, we have found that in the regime of the localized phase DMRG calculations yield rather poor results, which is basically caused by the restriction of the maximum number of particles per lattice site. In particular for the energy gap the DMRG algorithm is not able to provide good results for $U/J < 3$ (see Figure 5.3). This is in-line with the results for the DMRG convergence analysis depicted in the lower row of Figure 5.4. Here, in the regime $U/J < 3$ the DMRG-C and DMRG-D bases, which both have $\max\{n_i\} = 5$, yield the same results ($\Delta E/J \approx 5.5$ at $U/J = 1$), whereas the DMRG-E basis that has $\max\{n_i\} = 6$ yields a smaller energy gap ($\Delta E/J \approx 2.5$ at

	D_b	D_s	$\max\{n_i\}$	D_{super}
DMRG-C	21	126	5	446
DMRG-D	56	336	5	5073
DMRG-E	210	1470	6	68356

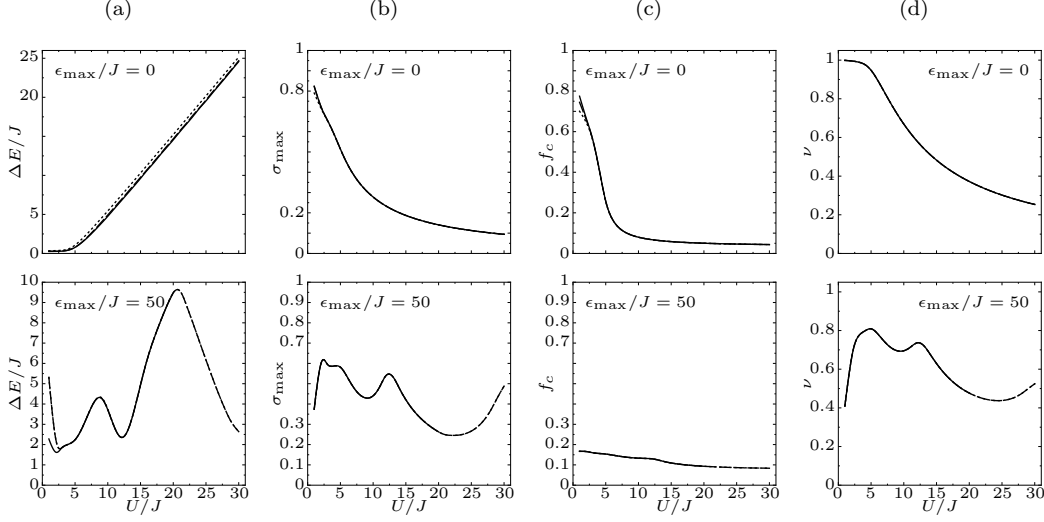Table 5.2: Bases specifications for the different DMRG calculations.

Figure 5.4: Check for the convergence of the DMRG calculations for a $I = N = 30$ lattice. Upper row: Superfluid to Mott-insulator transition ($\epsilon_{max}/J = 0$). Lower row: Localized to quasi Bose-glass transition ($\epsilon_{max}/J = 50$). (a) energy gap ΔE, (b) maximum number fluctuation σ_{max}, (c) condensate fraction f_c, (d) visibility ν. All plot shows three lines for the different bases: DMRG-C (dotted), DMRG-D (dashed), and DMRG-E (solid).

$U/J = 1$). Thus, the energy gap does not converge in the regime $U/J < 3$. Note that the exact calculation in a complete Hilbert space yields $\Delta E/J \approx 1$ at $U/J = 1$. The other observables refer to the ground state only which requires at most $\max\{n_i\} = 5$ to assemble all particles in the deepest well of the supercell. Hence, even the additional particle per lattice site provided by the DMRG-E basis does not change σ_{max}, f_c, and ν, i.e. they are converged for all values of U/J.

Homogeneous Mott-insulator to quasi Bose-glass transition ($U/J = 30$):
The observables in the Mott-insulator to quasi Bose-glass phase transition are shown in Figure 5.5. Here, all curves match perfectly, even for the small basis of the DMRG-C calculation. This indicates that the calculations in the strongly interacting regime are perfectly converged even when lattice irregularities are present.

To summarize, the DMRG is in general not the perfect method for the weakly interacting regime $U/J < 5$. Since the focus of the present work are the intermediate and the strong interaction regime, we conclude that the DMRG-C basis is already sufficient
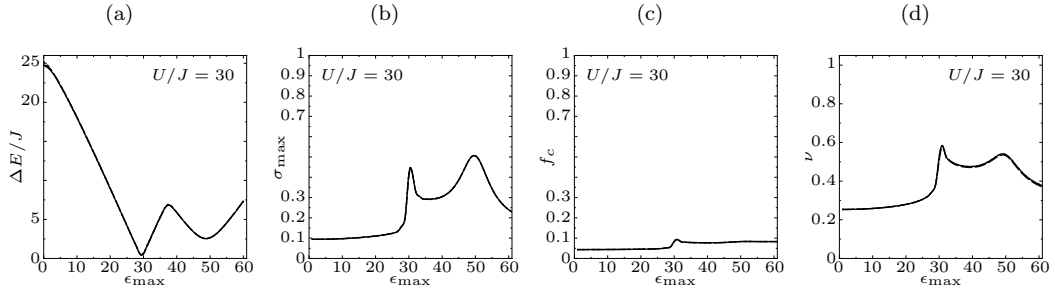
Figure 5.5: Check for the convergence of the DMRG calculations for a $I = N = 30$ lattice along the Mott-insulator to quasi Bose-glass transition. (a) energy gap ΔE, (b) maximum number fluctuation σ_{max}, (c) condensate fraction f_c, (d) visibility ν. All plot shows three lines for the different bases: DMRG-C (dotted), DMRG-D (dashed), and DMRG-E (solid)

to converge all observables. Nevertheless, we use the DMRG-D basis for the calculations presented in the remainder of this work. Calculations with this basis are still numerically feasible on a desktop PC.

5.3   Finite-Size Scaling Analysis

During our introduction of the relevant observables it already turned out that a detailed finite-size scaling analysis is necessary, in particular for the condensate fraction. Therefore, we calculate all observables for three different system sizes: $I = N = 10$, $I = N = 30$, and $I = N = 50$, using the DMRG-D basis as specified in Table 5.2. The less the observables deviate for different lattice sizes, the less they suffer from finite-size effects.

Superfluid to homogeneous Mott-insulator transition $(\epsilon_{\max} = 0)$:
The results for the superfluid to homogeneous Mott-insulator transition are shown in the upper row of Figure 5.6. The energy gap $\Delta E/J$ shows minor differences between the small and the two larger lattices in the vicinity of the phase transition $U/J \approx 5$. The number fluctuation $\sigma_{\max}$ is a local quantity, calculated with respect to single lattice sites only. Therefore, the size of the lattice does not play a crucial role for this of observable, as confirmed by the agreement of the calculations for the different lattice sizes. The condensate fraction, however, exhibits a strong, but expected, finite-size scaling. In the superfluid region $U/J < 5$, the differences are due to the limitations of the DMRG algorithm to describe the delocalization of particles which this leads to a systematic underestimation of f_c. The exact result can be calculated analytically to $f_c = 1$ at $U/J = 0$, independent of the size of the lattice (see Section 2.7.3). For large values of U/J one can clearly see the $1/I$ scaling of the condensate fraction. For $U/J > 2$ the visibility for the smallest lattice is always slightly below those of the two larger lattices, which lie on top of each other. As already mentioned, the visibility in homogeneous lattices is determined from the occupation numbers of the lowest and the highest quasi-momenta. In the small $I = N = 10$ lattice, the quasi-momentum space is rather coarse grained which leads to an artificially large occupation of the highest quasi-momentum and therefore a smaller visibility.

We also performed a calculation for the $I = N = 50$ lattice using the large DMRG-E basis. These results are not shown on the plots because there are no sizable deviations to calculations with the DMRG-D basis. Only in the superfluid regime, the condensate fraction obtained with the DMRG-E basis yields $f_c = 0.68$ instead $f_c = 0.63$ at $U/J = 1$. The results for all other observables remain completely unchanged when going to the larger DMRG-E basis.
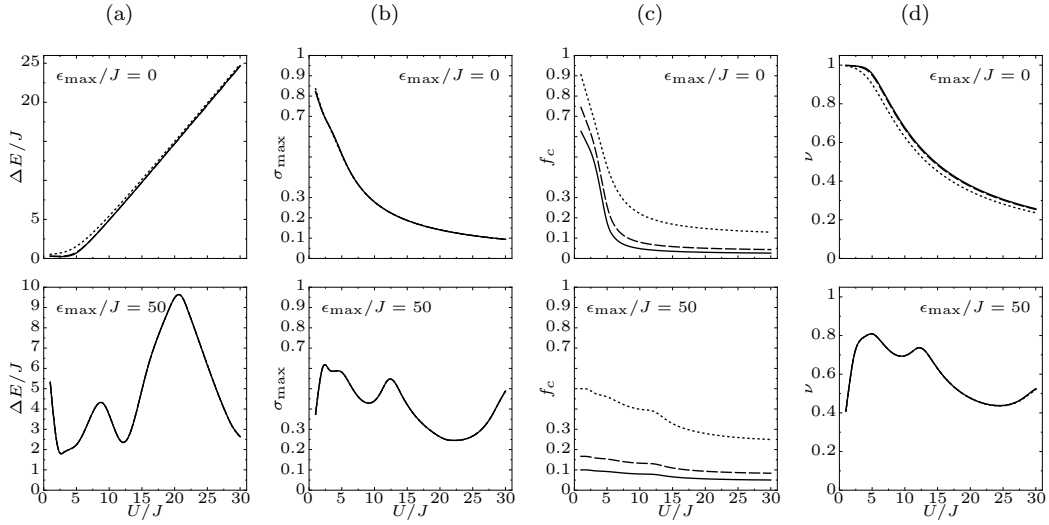
Figure 5.6: Finite-size scaling analysis using $I = N = 10$ (dotted), $I = N = 30$ (dashed), and $I = N = 50$ (solid), all calculated with the DMRG-D basis. Upper row: Superfluid to Mott-insulator transition ($\epsilon_{\max} = 0$). Lower row: Localized to quasi Bose-glass transition ($\epsilon_{\max} = 0$). (a) energy gap ΔE, (b) maximum number fluctuation $\sigma_{\max}$, (c) condensate fraction f_c, (d) visibility ν.

Localized to quasi Bose-glass phase transition ($\epsilon_{\max}/J = 50$):

The lower row of Figure 5.6 reveals that the condensate fraction shows a sizable finite-size effect with the characteristic $1/I$ scaling for large values of U/J. The results for the other observables are independent of the lattice size.

Homogeneous Mott-insulator to quasi Bose-glass transition ($U/J = 30$):

The analysis of the finite-size scaling for the Mott-insulator to quasi Bose-glass transition also reveals no suprises. In Figure 5.7, one can see that energy gap and number fluctuation show no dependence on the size of the lattice. The condensate fraction exhibits the $1/I$ scaling and the visibility is slightly different for the small $I = N = 10$ system.

Considering this analysis of the finite-size scaling for all observables, we conclude that calculations including 30 particles on 30 lattice sites are sufficient to provide quantitative predictions even for larger lattices. Current experiments typically have between $1.5 \cdot 10^4$ to $2 \cdot 10^5$ ^{87}Rb Bose-Einstein condensed atoms in the optical lattice [29, 26]. Thus, there are roughly 25 to 60 atoms in each spatial direction of the optical lattice and a
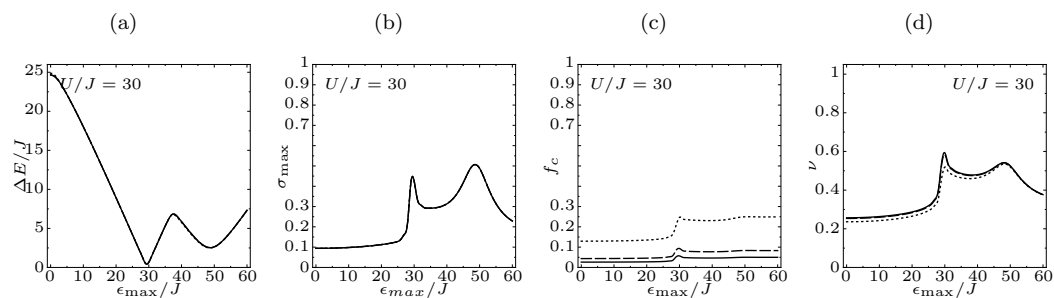
Figure 5.7: Finite-size scaling analysis along the Mott-insulator to quasi Bose-glass transition ($U/J = 30$), using $I = N = 10$ (dotted), $I = N = 30$ (dashed), $I = N = 50$ (solid), all calculated with the DMRG-D basis. (a) energy gap ΔE, (b) maximum number fluctuation σ_{max}, (c) condensate fraction f_c, (d) visibility ν.

calculation for $I = N = 30$ describes a realistic experimental situation.

5.4 Phase-Diagrams from Experimental Parameters

Now, the theoretical as well as the numerical framework to describe actual experiments is complete. We have introduced single-particle band structure calculations that provide the link between the experimental setup and the parameters of the Hubbard model. And we have introduced and tested the density-matrix renormalization group algorithm that allows for practically exact many-body calculations for lattice sizes that are realized in the experiment. Based on this framework, we will discuss the *ab-initio* phase diagram of ultracold ^{87}Rb atoms in a commensurate optical lattice as a function of the two optical lattice depths s_2 and s_1 and an optional harmonic trapping frequency ω_x. Furthermore, we will employ an incommensurate optical lattice to study a different superlattice topology and discuss the resulting changes in the structure of the quasi Bose-glass phase. Finally, we focus on one particular experiment to see whether our numerical results are in-line with the experimental results. The findings from Chapters 5.4.1 and 5.4.3 are published [53].

5.4.1 Commensurate Superlattice

We first consider a commensurate superlattice, where the ratio of the wavelengths, $\lambda_2 = 800$ nm and $\lambda_1 = 1000$ nm, is a fraction of small integers resulting in a super-lattice periodicity of five lattice sites. The phase shift between the lasers is $\phi = \pi/4$, the harmonic trapping frequency is $\omega_x = 0$, the perpendicular trapping frequency is $\omega_\perp = 30 E_{r_2}/h$, and the scattering length $a_s = 109\, r_{\mathrm{Bohr}}$ of ^{87}Rb is used. The resulting site-dependent Hubbard parameters are depicted in Figure 2.10. Our first conclusion from the analysis of the Hubbard parameters was that it is impossible to tune the two lattice amplitudes s_2 and s_1 such that ϵ_{max} dominates over $\bar{U}$. Hence, if we compare the generic phase diagram spanned by the the Hubbard parameters $\bar{U}/\bar{J}$ and $\epsilon_{\mathrm{max}}/\bar{J}$ with the experiment-specific phase diagram spanned by the optical lattice depths s_2 and s_1 in Figure 5.8, it turns out the localized phase is absent in the latter. In both cases we show the energy gap obtained from DMRG calculations for $I = N = 30$ using the DMRG-D basis specified in Table 5.2. Because the variation of s_2 and s_1 affects all site-dependent Hubbard parameters simultaneously, the (s_2, s_1) phase diagram is deformed relative to the generic $(U/\bar{J}, \epsilon_{\mathrm{max}}/\bar{J})$ phase diagram. Nonetheless, the superfluid phase, the Mott-insulator phase, and the quasi Bose-glass phase can be reached by variation of the two laser intensities alone, i.e., there is no need to vary other experimental parameters like the interatomic scattering length.
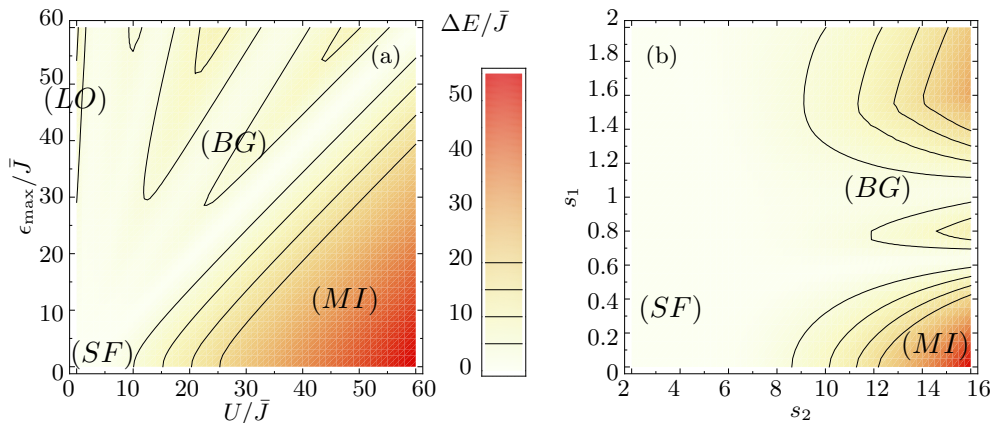
Figure 5.8: Contour plots of the energy gap computed with the DMRG-D basis for a commensurate superlattice with $I = N = 30$ as a function of the generic Hubbard parameters (a), and as a function of the experimental potential depth (b). The labels mark the domains of the superfluid (SF) phase, the homogeneous Mott-insulator (MI) phase, the quasi Bose-glass (BG) phase, and the localized (LO) phase.

A detailed analysis of the phase diagram as a function of s_2 and s_1 is given in Figures 5.9(a) to (d), where we depict the energy gap, the condensate fraction, the maximum number fluctuations, and the visibility, respectively, obtained in DMRG calculations for $I = N = 30$ using the DMRG-D basis specified in Table 5.2, and the experimental parameters mentioned above. The plots represent results from nearly 3000 individual DMRG calculations.

The superfluid (SF) phase is characterized by an almost vanishing energy gap, a large condensate fraction, large number fluctuations, and maximum visibility. Although the most stringent order parameter for this phase transition, i.e., the superfluid fraction [8, 28], is not shown here, these signatures allow us to identify the SF phase in the regime of small s_2, roughly up to $s_2 \lesssim 6$ for all $s_1 \lesssim 2$. In this regime the superlattice is shallow and tunneling dominates over on-site interactions and on-site energies. The large mobility of particles is a prerequisite for the long-range coherence present in the SF phase. For $s_1 = 0$, the ratio $\bar{U}/\bar{J}$ is about 1 at $s_2 = 2$, and reaches about 4.5 at $s_2 = 6$.

Around $\bar{U}/\bar{J} = 5$, the phase transition from a superfluid to a homogeneous Mott-insulator (MI) is expected, in one-dimensional Bose systems in homogeneous lattices

[54, 18], which is consistent with our observation. Even in the presence of the secondary laser, i.e. for $0 < s_1 \leq 2$, the lattice depth $s_2 = 6$ leads to $\bar{U}/\bar{J} \approx 4.5$, which explains the presence of the SF phase in the whole range of s_1 considered here. A detailed analysis of the phase transition as a function the generic Hubbard parameters based on an exact diagonalization technique in the complete Hilbert space can be found in Refs. [28, 38].

While increasing s_2 at fixed $s_1 = 0$ further, the system enters the MI phase at $U/J \gtrsim 5$. This phase is characterized by a large energy gap, a small condensate fraction, small fluctuations, and a minimal visibility. These signatures are clearly visible in Figure 5.9 for large values of s_2 and small values of s_1. At $s_1 = 0$ and $s_2 = 16$ the ratio U/J is about 60 and the system is deep in the MI regime.

If we now increase s_1 at fixed $s_2 \gtrsim 10$, the modulation of the site-dependent Hubbard parameters grows rapidly as we have observed in Figure 2.9. Already at $s_1 \approx 0.6$ the spread of the on-site energies becomes comparable to the average interaction strength, i.e., $\epsilon_{\max}/\bar{J} \approx \bar{U}/\bar{J} \approx 60$. Thus, it becomes energetically favorable to move particles from the lattice sites with largest on-site energies to the sites with the lowest on-site energies and create double occupancies. In this way the homogeneous MI phase is broken up and the transition to a quasi Bose-glass (BG) phase occurs. The maximum number-fluctuation, the condensate fraction, and the visibility depicted in Figure 5.9 show a sudden increase at the transition point, indicating that local as well as global properties of the system change.

The commensurate superlattice exhibits only 5 different on-site energies. This always gives rise to finite energy gaps and extended domains in the BG phase, where certain occupation-number states dominate the ground state—two of those domains are also visible in Figure 5.9(a). Only in the transition regions between those domains the energy gaps become small. In a random infinite-size lattice, the BG phase is characterized by a vanishing energy gap. Intuitively, this results from the continuous distribution of on-site energies, which allows the construction of excited states with infinitesimal small excitation energies by redistributions of atoms to sites with infinitesimally larger on-site energies. We will approach this limit by applying an incommensurate superlattice in Section 5.4.3.
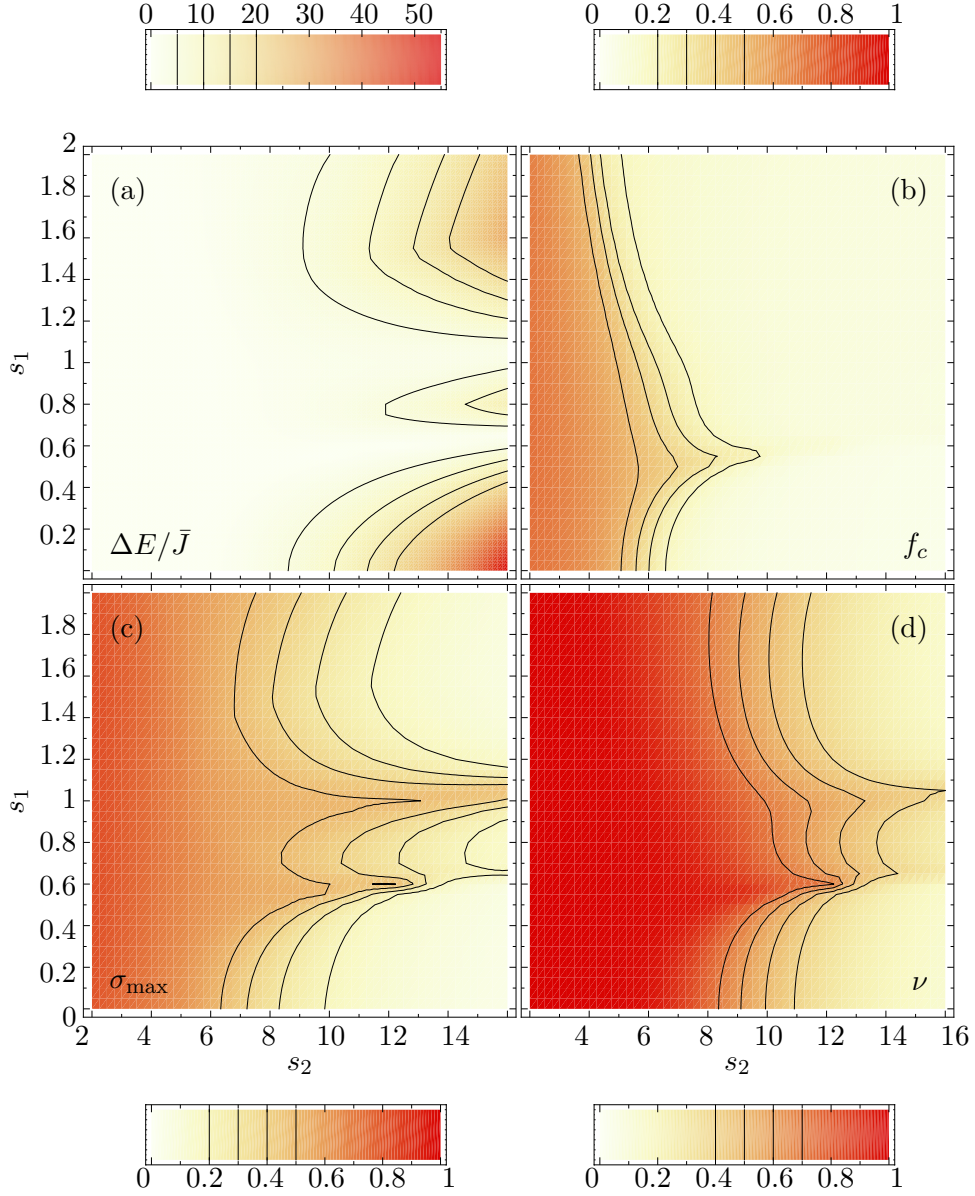
Figure 5.9: Phase diagrams for an $I = N = 30$ lattice using realistic experimental parameters (see text). (a) Energy gap $\Delta E/\bar{J}$, (b) condensate fraction f_c, (c) maximum number fluctuations $\sigma_{\max}$, and (d) visibility ν.

5.4.2   Influence of the Harmonic Trapping Potential

Our *ab-initio* framework allows for studying the effects on account of the Gaussian beam profile of the strong primary laser and the magnetic trapping potential via a harmonic potential with frequency ω_x (see Eq. 2.37), chosen according to typical experimental setups. We will discuss phase diagrams for increasing ω_x in the following.

We have already discussed the energy scales introduced by this harmonic potential in Section 2.6 and found that up to $\omega_x = 2\pi\,25$ Hz, the influence on the on-site energies ϵ_l is an order of magnitude smaller than $\bar{U}$. For this reason, the phase diagram remains practically unaltered compared to the phase diagram with $\omega_x = 0$ as visible in Figures 5.9 and 5.10.

Table 2.1 reveals that for $\omega_x = 2\pi\,50$ Hz the on-site energies are smaller but of the same order of magnitude as the interaction energy. Thus, all observables depicted in Figure 5.11 remain almost unaltered for an optical potential $s_1 < 0.5$ generated by the weak laser. However, above $s_1 = 0.5$ the energy gap in Figure 5.11(a) shows a supression of the lobes in the quasi Bose-glass phase. Together with the maximum fluctuations this indicates that redistributions of particles happen more frequently. This is beacause at $\omega_x = 0$ there are only 5 different on-site energies available for the superlattice topology we employ. For $\omega_x \neq 0$, this periodicity of 5 is broken. Thus, there are more regions in the phase diagrams where redistribution of particles can occur due to the increased number of different on-site energies. The onset of the quasi Bose-glass phase appears earlier at $s_1 \approx 0.4$ instead of $s_1 \approx 0.6$ for $\omega_x = 2\pi\,25$ Hz. This is a direct consequence of the additional contribution of the harmonic potential to the on-site energies ϵ_l.

For frequencies $\omega_x = 2\pi\,75$ Hz, the maximum on-site energy $\epsilon_{\max}$ is just below the interaction energy $\bar{U}$ (see Table 2.1). The corresponding Figure 5.12(a) reveals that the energy gap stays small even for values $s_2 \approx 11$ for $s_1 = 0$. The fluctuations as well as the visibility decrease not until $s_2 \gtrsim 10$, compared to smaller values of ω_x. This means that the onset of the Mott-insulating phase is clearly shifted towards larger s_2. The onset of the quasi Bose-glass phase now already occurs at $s_1 \approx 0.2$ for $s_2 \lesssim 10$.

In Table 2.1 we can see that the maximum on-site energy $\epsilon_{\max}$ clearly dominates the energy scales at $\omega_x = 2\pi 100$ Hz. Therefore, in Figure 5.13(a) the Mott-insulating phase has completely vanished for the range of the optical lattice depth considered in this work, and consequently, the Mott-insulator to quasi Bose-glass phase transition is no longer

visible.

To conclude, we have observed that a strong change of the structures in the phase diagram is induced by an additional harmonic potential. A clear identification of the homogeneous Mott-insulating phase for the laser frequencies studied here is only possible in the region of $\omega_x \lesssim 2\pi\,75$ Hz. One can clearly observe a shift of the SF to MI transition towards larger values of s_2 with increasing ω_x due to the growing repulsive interactions that are needed to overcome the increasing differences between the on-site energies. Therefore, a unique definition of the critical value for s_2, or equivalently $\bar{U}/\bar{J}$, for the superfluid to Mott-insulator phase transition is intimately connected to the value of ω_x. We further point out, that experiments aiming at the regime of the Bose-glass phase by using a two-color superlattice should be aware that trapping frequencies above $\omega_x = 2\pi\,25$ Hz lead to ambiguous signatures of this phase due to the subtle interplay of the two energy scales. These issues should be considered in ongoing experiments.
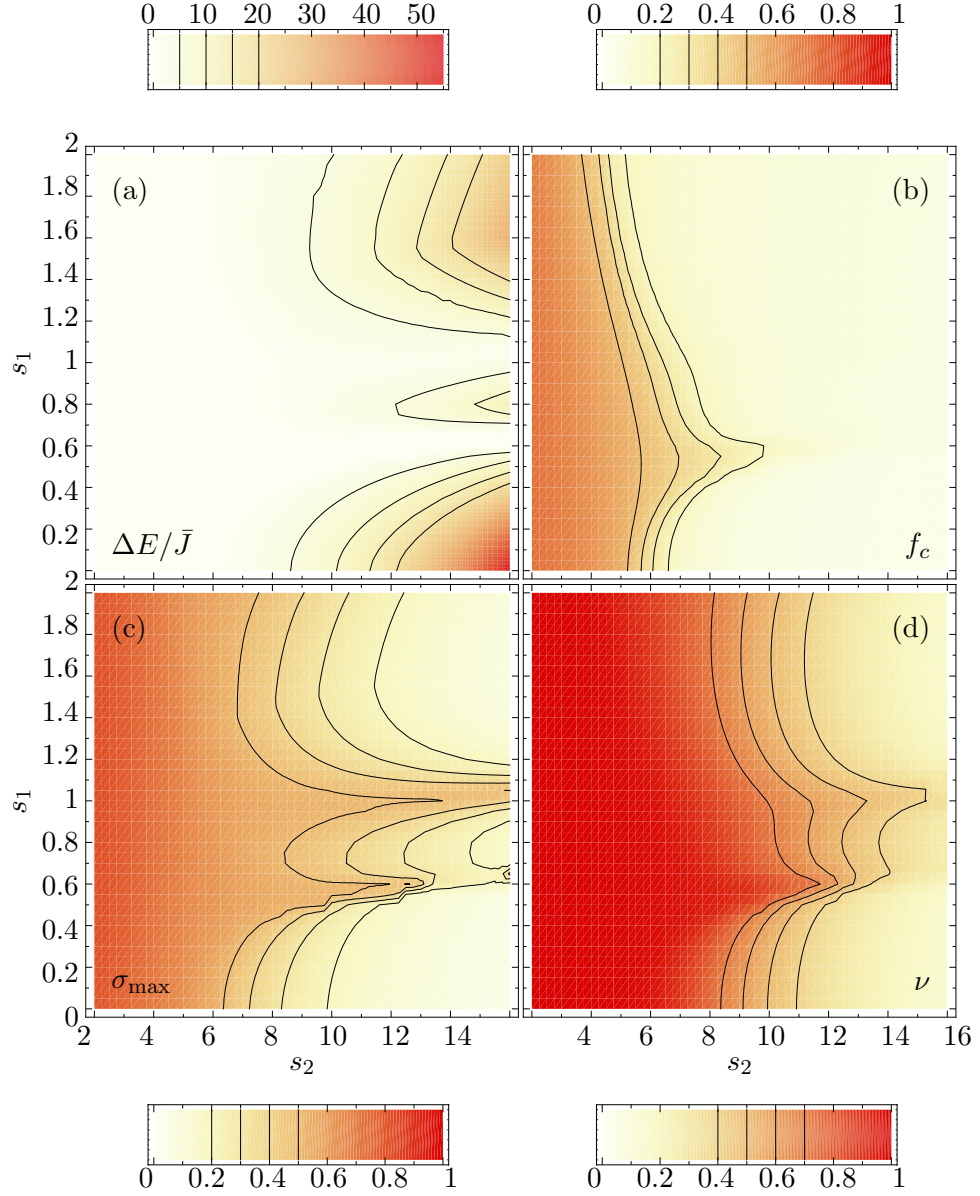
Figure 5.10: Phase diagrams for an $I = N = 30$ lattice using realistic experimental parameters (see text) and $\omega_x = 2\pi\,25$ Hz. (a) Energy gap $\Delta E/\bar{J}$, (b) condensate fraction f_c, (c) maximum number fluctuations $\sigma_{\max}$, and (d) visibility ν.
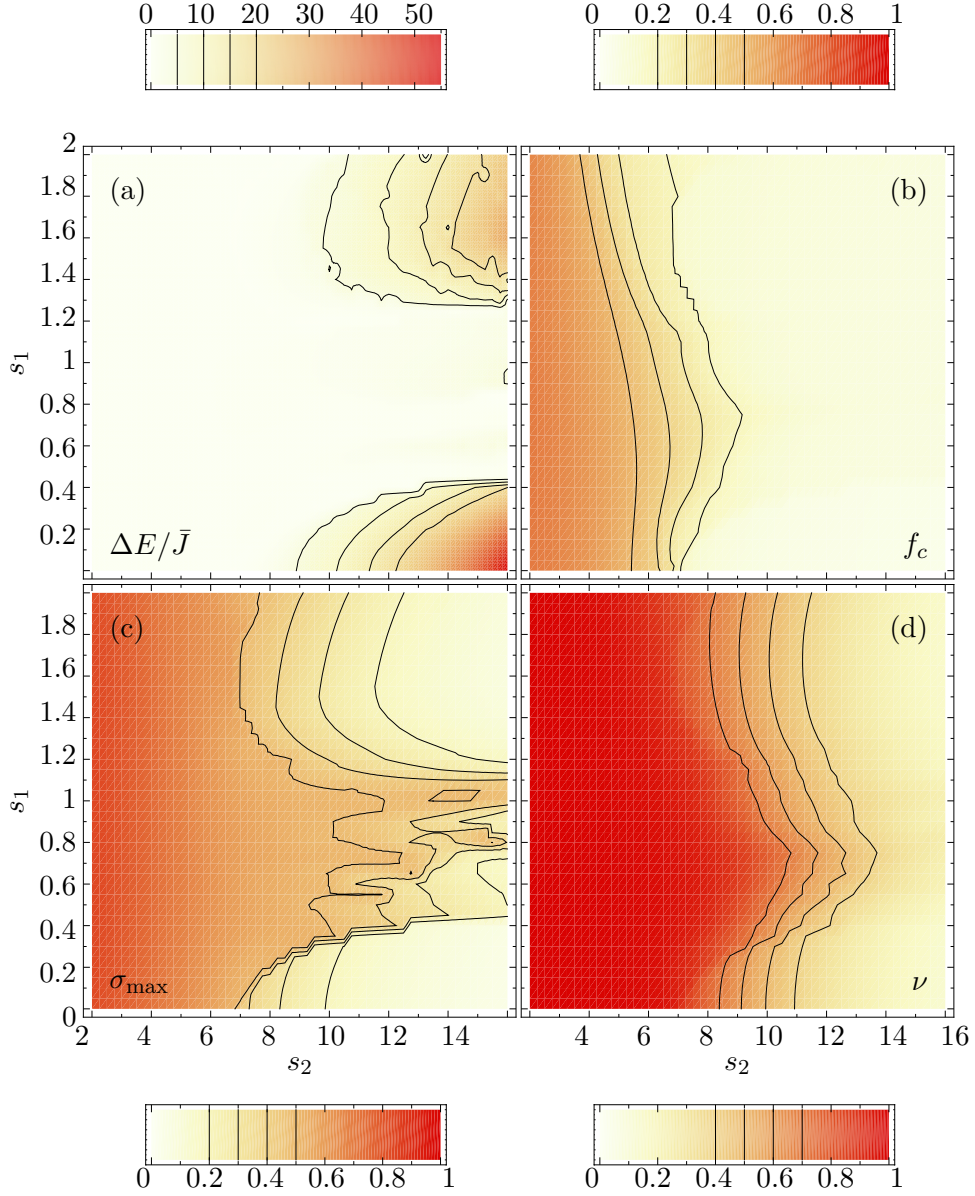
Figure 5.11: Phase diagrams for an $I = N = 30$ lattice using realistic experimental parameters (see text) and $\omega_x = 2\pi\,50$ Hz. (a) Energy gap $\Delta E/\bar{J}$, (b) condensate fraction f_c, (c) maximum number fluctuations $\sigma_{\max}$, and (d) visibility ν.

Figure 5.12: Phase diagrams for an $I = N = 30$ lattice using realistic experimental parameters (see text) and $\omega_x = 2\pi\,75$ Hz. (a) Energy gap $\Delta E/\bar{J}$, (b) condensate fraction f_c, (c) maximum number fluctuations $\sigma_{\max}$, and (d) visibility ν.
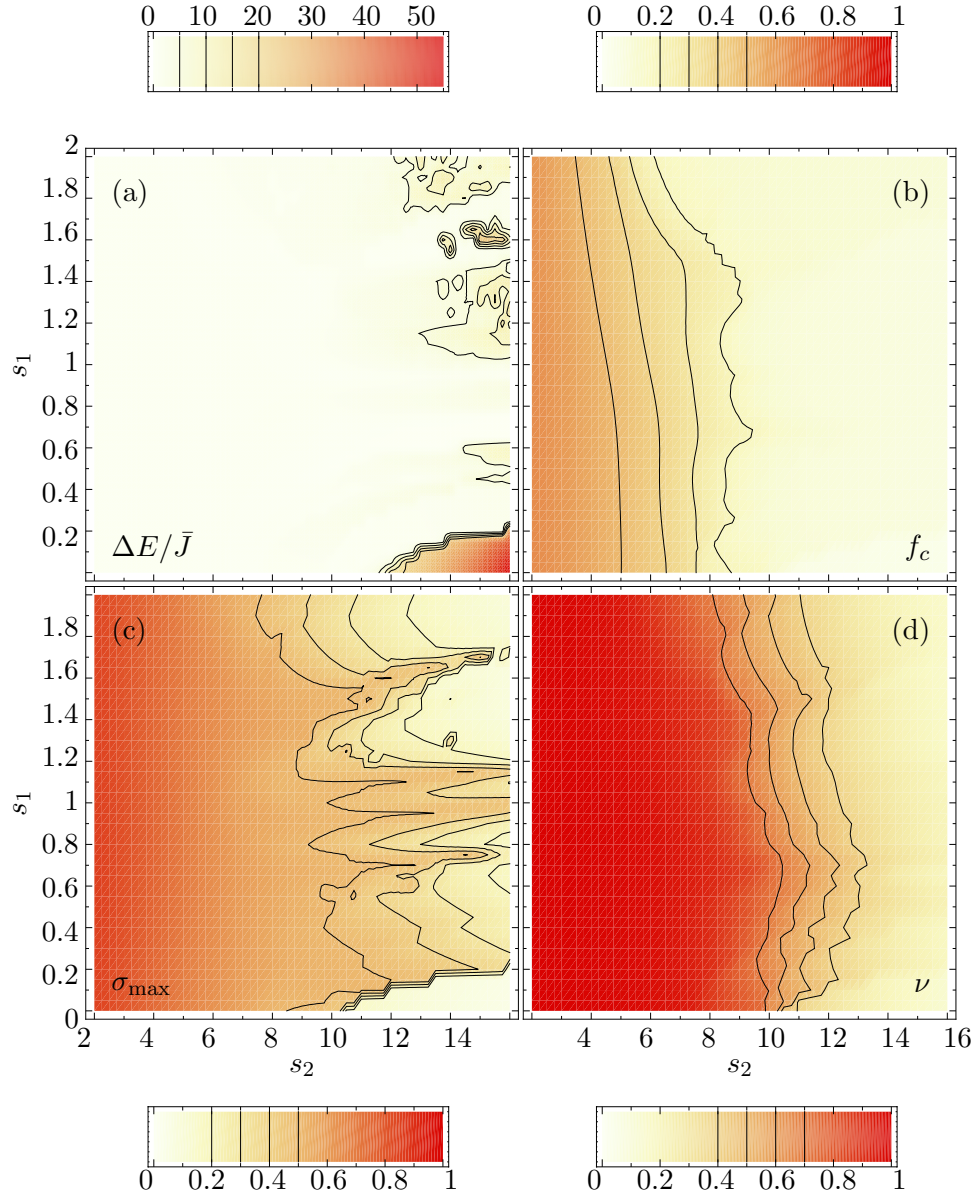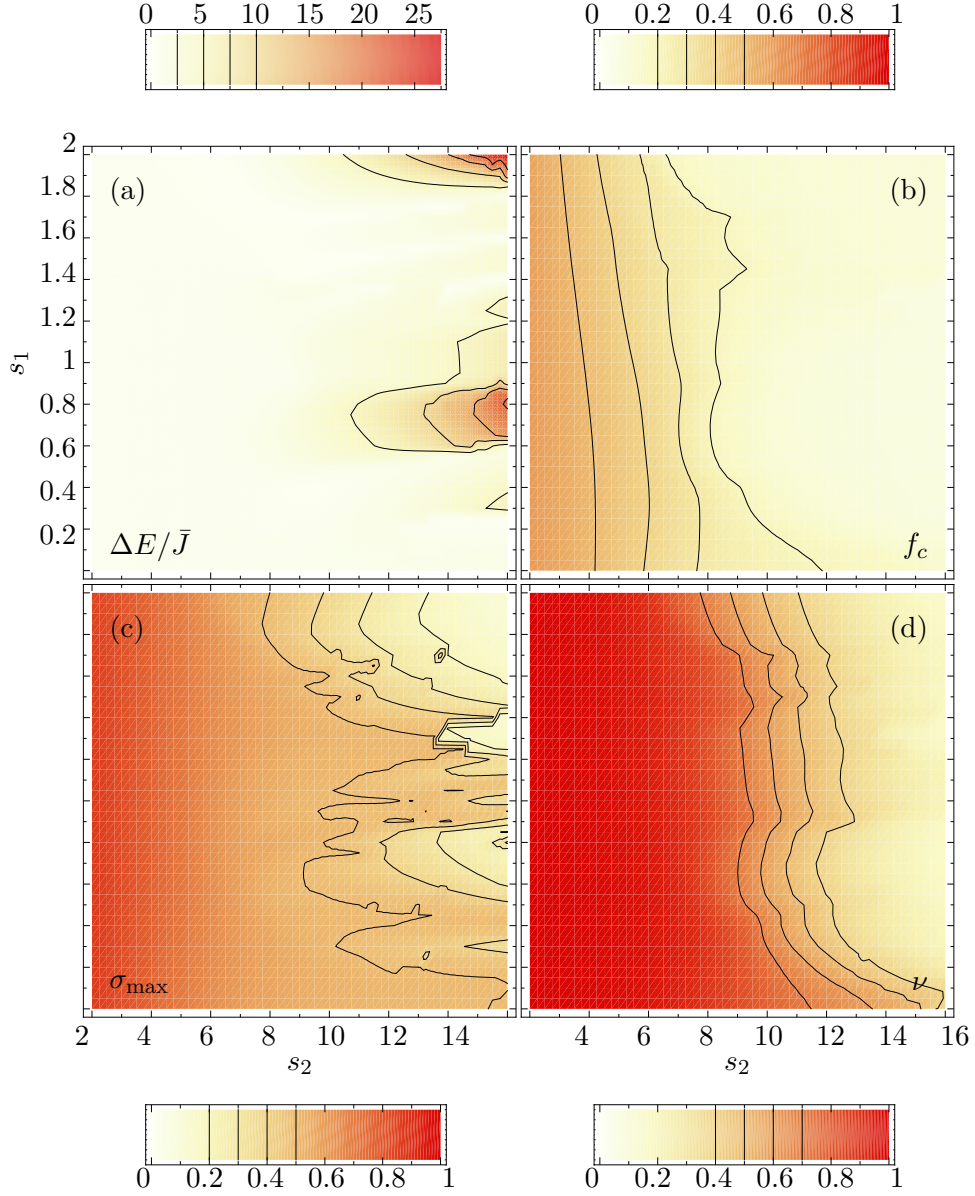
Figure 5.13: Phase diagrams for an $I = N = 30$ lattice using realistic experimental parameters (see text) and $\omega_x = 2\pi\,100$ Hz. (a) Energy gap $\Delta E/\bar{J}$, (b) condensate fraction f_c, (c) maximum number fluctuations $\sigma_{\max}$, and (d) visibility ν.

5.4.3 Incommensurate Lattice

The commensurate superlattice we discussed in the previous section is by definition unable to generate a true Bose-glass phase. For that reason we have introduced the terminology *quasi* Bose-glass. As already mentioned, the true Bose-glass phase is signaled by a vanishing energy gap caused by continuous redistributions of the particles among the lattice sites while changing the strength of the superlattice. Following this strict definition, the Bose-glass phase can only occur in an infinite lattice with random on-site energies. We are of course limited to a finite lattices and can only study the influence of larger number of different on-site energies. In order to approach a more realistic Bose-glass phase, we have to consider more complex lattice topologies. To this end, we repeat the above analysis for an incommensurate lattice with $\lambda_2 = 830$ nm, $\lambda_1 = 1076$ nm, $\phi = \pi/3$ inspired by the experimental setup in Refs. [26, 29]. For the sake of simplicity we abandon the harmonic potential and set $\omega_x = 0$. The incommensurate wavelengths lead to a modulation of the site-dependent Hubbard parameters with a periodicity which does not correspond to a small integer number of lattice sites, as seen in Fig. 2.9. Therefore, the pattern of on-site energies ϵ_l is not periodic anymore as in the case of the commensurate lattice.

The resulting phase diagrams for $I = N = 30$ are depicted in Figures 5.14. Evidently, the structure and extension of the superfluid and the Mott-insulator phases are not affected by the change in the lattice topology. Only the Bose-glass phase exhibits a different behavior. The energy gap is clearly reduced due to the irregular character of the superlattice. The larger number of different on-site energies allows for redistributions associated with lower excitation energies and reduced energy gaps. The more irregular the lattice, the stronger the reduction of the energy gap in the quasi Bose-glass phase—eventually the true Bose-glass phase in a random lattice would be approached. Observables like the condensate fraction and the visibility are still suppressed in the Bose-glass phase and allow for a unique distinction from the superfluid phase.
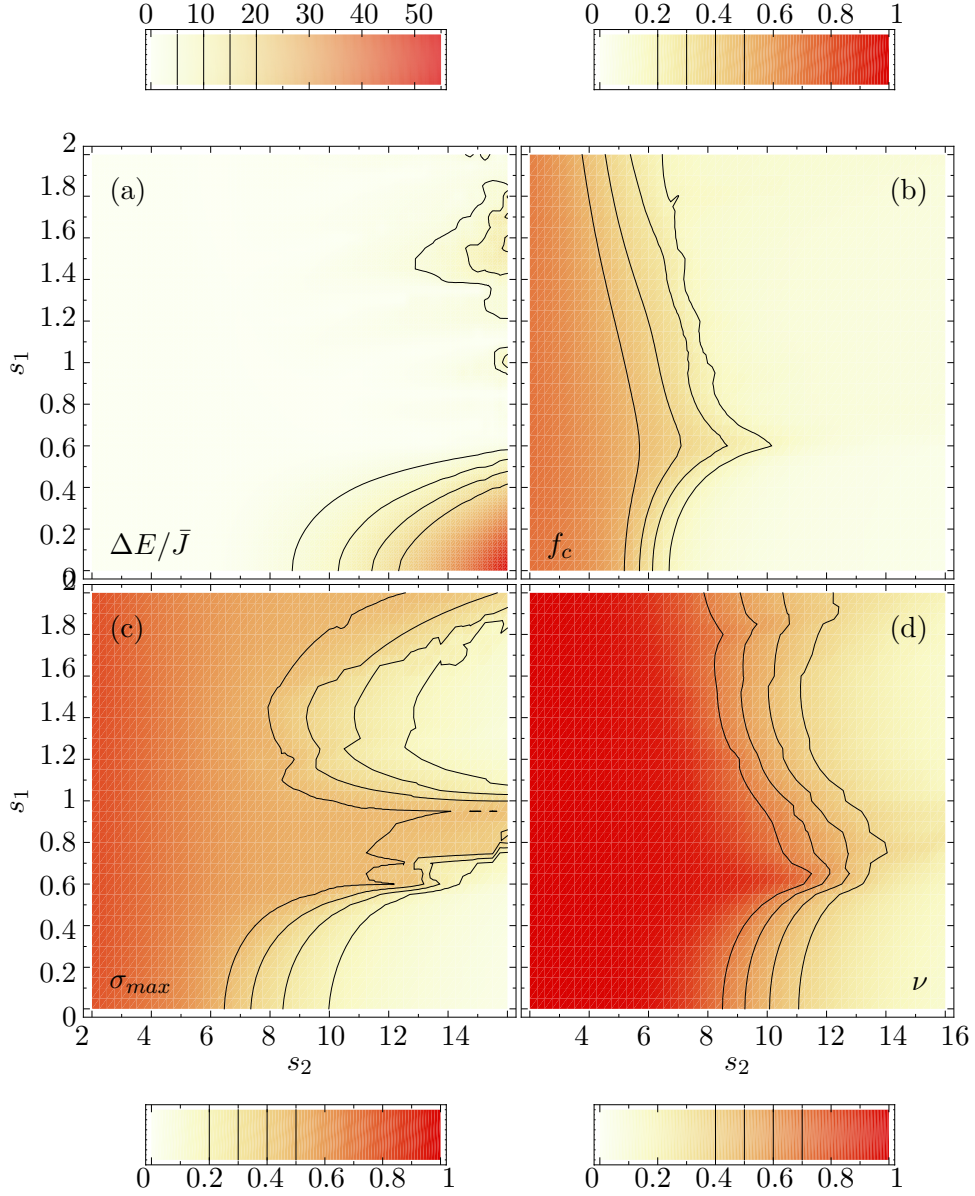
Figure 5.14: Phase diagrams for an incommensurate $I = N = 30$ lattice using realistic experimental parameters (see text). (a) Energy gap $\Delta E/\bar{J}$, (b) condensate fraction f_c, (c) maximum number fluctuations σ_{max}, and (d) visibility ν.

5.4.4   Comparison to an Experiment

Our rigorous approach starting directly from the experimental parameters allows us to express the energy gap in units of the natural energy scale, the recoil energy. We can exploit this to establish a direct connection to an experiment done by Stöferle et al. [10], where the excitation spectrum of Bose-Einstein condensed ^{87}Rb atoms in an optical lattice was measured via a time-dependent modulation of the laser intensity and consequently the optical potential. We do not have the ability to calculate the full excitation spectrum because this would require a dynamic treatment of the many-body problem which can be found in Refs. [32, 33, 55]. However, the energy gap ΔE sets a lower bound for possible energy transfers to the system. Thus, we expect the system to start to respond to a modulation of the lattice around a modulation frequency of $\Omega_{\mathrm{mod}} = \Delta E / \hbar$.

In the following, we assume one laser with wavelength $\lambda = 826$ nm and the harmonic trapping frequency $\omega_x = 2\pi 20$ Hz for the harmonic potential, as specified in [10].

In previous calculations we mostly employed a transverse trapping frequency of $\omega_\perp = 2\pi 16.3$ kHz to calculate the interaction parameter U via Equation (2.33). Now we use the trapping frequency

$$\omega_\perp = \sqrt{\frac{2 s_\perp E_r}{m}} \frac{2\pi}{\lambda} \tag{5.2}$$

as calculated in Appendix A.2. Although this choice of $\omega_\perp$ does not reproduce the mapping from the optical lattice depth s to the Hubbard parameters U/J given in Figure 2(a) of Ref. [10] (see Fig. 5.16), we think it provides an adequate description of the experiment. For a potential depth of $s_\perp = 30$ in the transverse directions, we obtain $\omega_\perp = 2\pi\,37.5$ kHz using Eq. (5.2). A comparison of the Hubbard parameters resulting from the different transverse trapping frequencies can be found in Appendix A.4. As a direct consequence of the larger $\omega_\perp$, the system enters the Mott-insulating phase at smaller values of the lattice depth. This is evident from the condensate fraction f_c shown in Figure 5.15 for the two different transverse trapping frequencies with all other parameters unchanged.

The resulting data from the experiment were already shown in Figure 1.3, where the width of the central interference peak is measured. This width is correlated to the energy transfer to the system induced by the modulation. The experimental excitation spectra for different depth of the optical lattice are shown in Figure 5.16. The excitation
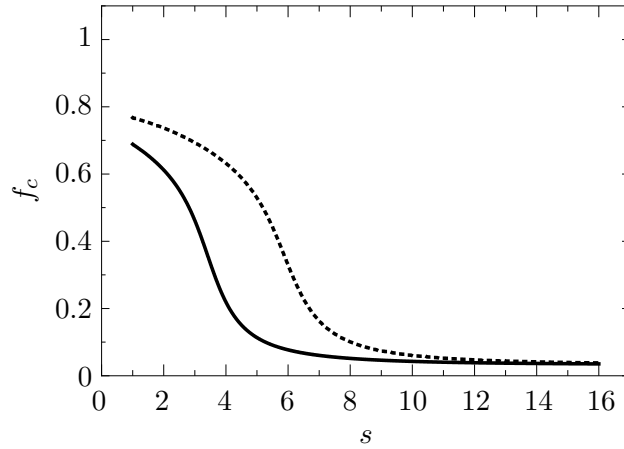
Figure 5.15: Condensate fraction f_c for $I = N = 30$ and $\omega_\perp = 2\pi\,37.5$ kHz (solid) obtained from Eq. (5.2), and $\omega_\perp = 2\pi\,16.3$ kHz (dotted) which reproduces the mapping from the optical lattice depth s to the Hubbard parameters U/J in Ref. [10].

spectrum was measured for a potential depth $s = 10$ which corresponds to $U/J = 32$ if we use a transverse trapping frequency of $\omega_\perp = 2\pi\,37.5$ kHz instead of $U/J = 14$ for $\omega_\perp = 2\pi\,16.3$ kHz as stated in Ref. [10].

Since we allow for a harmonic trapping potential along the optical lattice, the energy gap depends on the number of particles in the system. However, this information cannot be determined by the experiment. Therefore, we employ two different lattice sizes, $I = N = 30$ and $I = N = 60$, that cover the experimental relevant regime. Our results for the energy gap ΔE are depicted in Figure 5.17. At $s = 10$ we have an energy gap of $\Delta E = 0.5\,E_r$ which results in $\Omega_{\mathrm{mod}} \approx 2\pi\,1.7$ kHz for the small $I = N = 30$ system, and $\Delta E = 0.46\,E_r$ which gives $\Omega_{\mathrm{mod}} \approx 2\pi\,1.55$ kHz for the large $I = N = 60$ system. The centroid of the first excitation peak in the experiment is approximately around 1.6 kHz. Hence, our calculation is in good agreement with the experiment.

On the other hand, our calculations show an increase of the energy gap with increasing potential depth s. This would result in a slight shift of the excitation peak towards larger modulation frequencies which is not observed in the experiment as shown in Figure 5.16. The reason for this could be a nontrivial correlation between the width of the central interference peak and the energy transfer to the system. Regarding this, we are still in
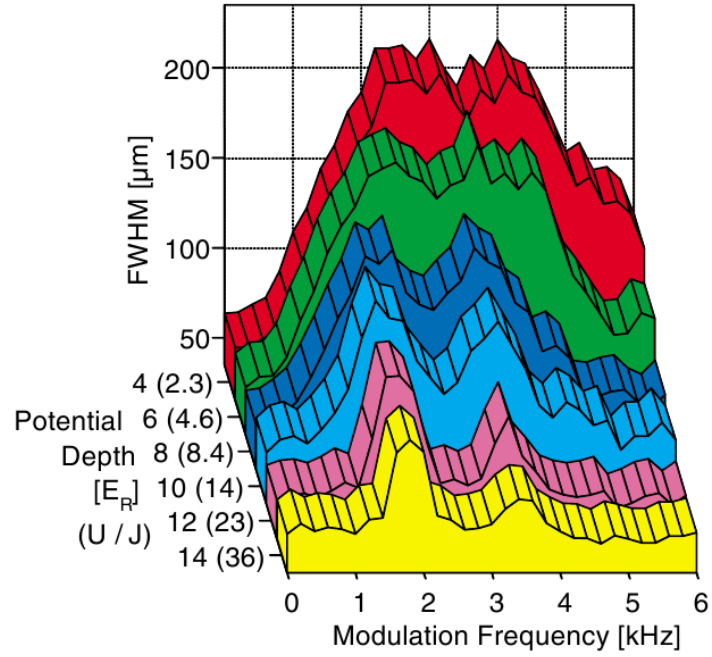
Figure 5.16: Spectroscopy of ultracold ^{87}Rb atoms in an array of 1D optical lattices. The system is excited via a modulation of the intensity of the laser beam. The picture is taken from [10].

good agreement with the experimental data. Therefore, we conclude that our *ab-initio* framework, starting directly from the experimental parameters is capable of providing qualitative and even quantitative results for the observables we have presented in this work.

Figure 5.17: Energy gap $\Delta E/E_r$ for the parameters specified in the experiment [10] and $I = N = 30$ (solid), $I = N = 60$ (dotted).

Chapter 6

BEC in an Optical Ring-Potential

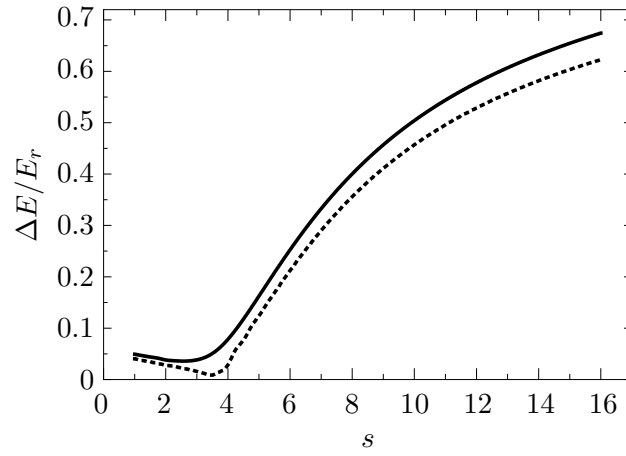## 6.1 Experiment with Thermal Atoms

The group of Gerhard Birkl [19] designed an experiment which will enable them to study the time evolution of ultracold ^{87}Rb atoms in a quasi one-dimensional ring-shaped optical-potential. As an application, this setup could be used as a high-precision atom interferometer. But it is also very appealing from a theoretical point of view since it is an experimental realization of periodic boundary conditions. The optical ring-potential is generated via an image of a ring-lense that is irradiated with a laser with wavelength $\lambda = 795$ nm. This red-detuning with respect to the atomic resonance of ^{87}Rb leads to an attractive force in direction of the intensity maximum [21]. A comprehensive introduction to the experiment as well as the detailed optical setup can be found Ref. [56].

In the laboratory the first experiments with a cloud of thermal atoms with temperatures of about $100\,\mu$K have already been performed. A sequence of fluorescence images at different times is shown in Figure 6.1. After the atoms are trapped and cooled, they are loaded to the optical ring-potential which is aligned vertically. One can clearly see a sizeable fraction of the atoms following the optical ring potential.

In order to use this setup as an interferometer, one needs a possibility to split the atom cloud and guide the two parts along the ring potential. This can be achieved with a elongated laser beam that irradiates a stripe of the ring lense. If the stripe is moved over the lense, this results in an time-dependent potential moving along the optical ring.
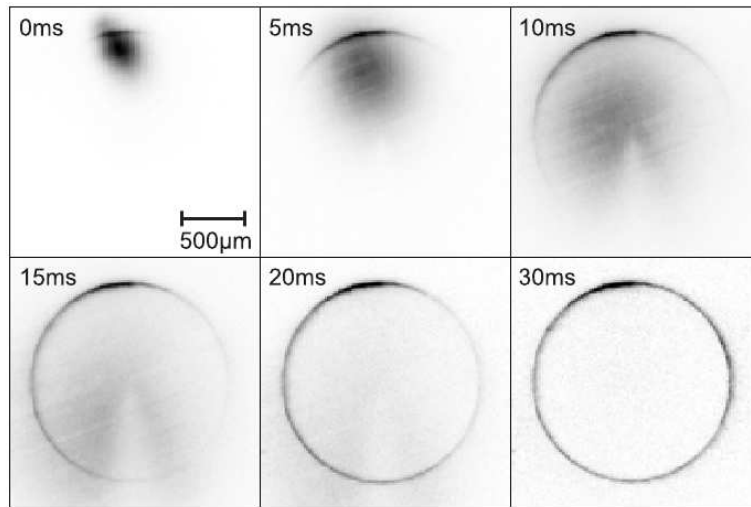
Figure 6.1: Sequence of fluorescence images of thermal atoms following the tilted, optical ring-potential. The potential depth is about $V_0 = 2\,k_B$ mK and the diameter of the ring is 1.5 mm. In the last picture approximately 3000 atoms are distributed over the optical ring-potential. The picture is from [56].

We will introduce a such a potential later on. For an example of the potential we refer to Figure 6.4. The experimental results for the thermal atoms that are now transported along the optical ring are shown in Figure 6.2.

Figure 6.2: Time evolution of a thermal atom cloud with a guiding potential. The picture is from [56].

6.2   BEC in an Optical Ring-Potential

After the demonstrating the feasibility of trapping and guiding cold atoms inside the one-dimensional optical ring potential, the next experimental goal is using Bose-Einstein condensed atoms instead of thermal atoms. Our aim is to provide some insight regar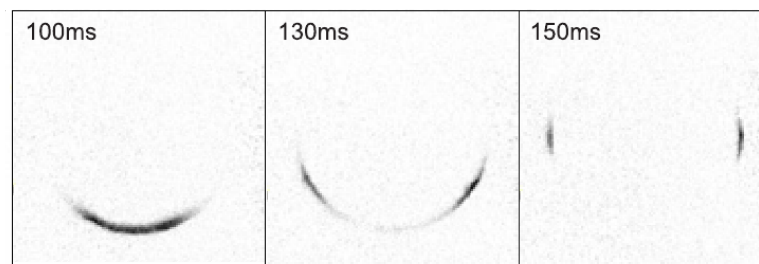ding the relevant timescales, geometries, and potential depths that might help designing the experiment. To this end, we employ the time-dependent Gross-Pitaevskii equation (GPE) [57] for the description of an interacting Bose-Einstein condensate. For the time evolution we use the numerically efficient and stable Split-Operator Fast-Fourier Transformation (SOFFT) method.

After an introduction of the theoretical framework, we present free time evolutions in two optical rings with different diameters to study the expected timescales in the experiment. Then we consider the time-dependent potential that is used in the experiment to guide the Bose-Einstein condensate along the optical ring and make first statements of the required potential depth. More comprehensive simulations based upon this framework accounting for a variety of different experimental parameters were subject of a Bachelor thesis [59].

6.2.1   Gross-Pitaevskii Equation

The Gross-Pitaevskii equation (GPE) can be used to describe a Bose-Einstein condensate with an additional two-particle contact interaction in an external trapping potential. The Gross-Pitaevskii ansatz assumes that the gas is a perfect Bose-Einstein condensate, i.e., all particles occupy the energetically lowest single-particle state, therefore, the temperatue is zero. For the sake of convenience, we start directly with the one-dimensional GPE.

A symmetrized N-body $\left| \psi \right\rangle$ can be written as

$$\left| \psi \right\rangle = \hat{\mathcal{S}} \left| \alpha_1 \right\rangle \otimes \left| \alpha_2 \right\rangle \otimes \cdots \otimes \left| \alpha_N \right\rangle \equiv \left| \alpha_1, \alpha_2, \cdots, \alpha_N \right\rangle_s , \qquad (6.1)$$

where $\hat{\mathcal{S}}$ is the symmetrization operator and $\left| \alpha_i \right\rangle$ the single-particle states. The many-body Hamilton operator including an external time-dependent potential and an additional two-body interaction term is written in second quantization

$$\hat{H} = \sum_{\alpha\alpha'} T_{\alpha\alpha'} \hat{a}_\alpha^\dagger \hat{a}_{\alpha'} + \sum_{\alpha\alpha'} V_{\alpha\alpha'}(t) \hat{a}_\alpha^\dagger \hat{a}_{\alpha'} + \frac{1}{2} \sum_{\alpha_1,\alpha_2} \sum_{\alpha_1',\alpha_2'} U_{\alpha_1\alpha_2\alpha_1'\alpha_2'} \, \hat{a}_{\alpha_1}^\dagger \hat{a}_{\alpha_2}^\dagger \hat{a}_{\alpha_2'} \hat{a}_{\alpha_1'} \qquad (6.2)$$

with the matrix elements

$$T_{\alpha\alpha'} = \big\langle\, \alpha \,\big|\, \frac{\hbar^2 \hat{k}^2}{2m} \,\big|\, \alpha' \,\big\rangle \,, \tag{6.3}$$

$$V(t)_{\alpha\alpha'} = \big\langle\, \alpha \,\big|\, V(\hat{x}, t) \,\big|\, \alpha' \,\big\rangle \,, \tag{6.4}$$

$$U_{\alpha_1\alpha_2\alpha_1'\alpha_2'} = \big\langle\, \alpha_1\alpha_2 \,\big|\, u(\hat{x}_1, \hat{x}_2) \,\big|\, \alpha_1'\alpha_2' \,\big\rangle \,, \tag{6.5}$$

where the latter indicates a matrix element with respect to a product state. We assume a contact interaction with s-wave scattering length a_s and a Gaussian shape of the wavefunction in the transverse directions resulting from a harmonic potential with frequency $\omega_\perp$. The one-dimensional contact interaction is then given by

$$u(\hat{x}_1, \hat{x}_2) = 2\hbar\,\omega_\perp\, a_s\, \delta(\hat{x}_1 - \hat{x}_2) \,. \tag{6.6}$$

For more details about the 1D contact interaction we refer to Appendix A.1. Using the coordinate representation $\alpha_j(x_i) = \big\langle\, x_i \,|\, \alpha_j \,\big\rangle$, the two-body matrix element is given by

$$
\begin{aligned}
\big\langle\, \alpha_1\alpha_2 \,\big|\, u(\hat{x}_1, \hat{x}_2) \,\big|\, \alpha_1'\alpha_2' \,\big\rangle =\,& 2\hbar\omega_\perp a_s \big\langle\, \alpha_1\alpha_2 \,\big|\, \delta(\hat{x}_1 - \hat{x}_2) \\
&\cdot \int dx_1 \int dx_2 \,\big|\, x_1 x_2 \,\big\rangle\!\big\langle\, x_1 x_2 \,\big|\,\big|\, \alpha_1'\alpha_2' \,\big\rangle \\
=\,& 2\hbar\omega_\perp a_s \int dx_1 \int dx_2 \,\delta(x_1 - x_2) \\
&\cdot \alpha_1^*(x_1)\,\alpha_2^*(x_2) \cdot \alpha_1'(x_1)\,\alpha_2'(x_2) \\
=\,& 2\hbar\omega_\perp a_s \int dx_1 \,\alpha_1^*(x_1)\alpha_2^*(x_1)\alpha_1'(x_1)\alpha_2'(x_1) \,. \tag{6.7}
\end{aligned}
$$

The calculation of the one-body matrix elements for the kinetic energy and the external harmonic potential is straightforward.

If we now follow the assumption of the Gross-Pitaevskii ansatz and put all particles in the same single-particle state $\big|\, \alpha_i \,\big\rangle = \big|\, \phi \,\big\rangle$ we obtain from the expectation value of the Hamiltonian at a fixed time t_0 an energy functional of the form:

$$\big\langle\, \psi \,\big|\, \hat{H} \,\big|\, \psi \,\big\rangle = E[\phi] = \tag{6.8}$$

$$N \int dx \left(-\frac{\hbar^2}{2m}\phi^*(x)\frac{\partial^2}{\partial x^2}\phi(x) + V(x, t_0)\phi^*(x)\phi(x) + \frac{(N-1)}{2}\, 2\,\hbar\,\omega_\perp\, a_s\, \big[\phi^*(x)\big]^2 \big[\phi(x)\big]^2 \right) .$$

Usually one defines a macroscopically N-body wavefunction using $\Psi(x) = \sqrt{N}\phi(x)$ and $N \approx (N-1)$. This yields the energy functional

$$E[\Psi] = \int dx \left(-\frac{\hbar^2}{2m}\Psi^*(x)\frac{\partial^2}{\partial x^2}\Psi(x) + V(x, t)\Psi^*(x)\Psi(x) + \hbar\omega_\perp a_s \big[\Psi^*(x)\big]^2 \big[\Psi(x)\big]^2 \right) . \tag{6.9}$$

The minimization of this energy functional under the constraint of conserving the total particle number

$$\int |\Psi(x)|^2 dx = N \tag{6.10}$$

leads to

$$0 = \delta\left(E[\Psi(x)] - \lambda \int |\Psi(x)|^2 dx\right) \tag{6.11}$$

$$= \int dx \left(-\frac{\hbar^2}{2m}\frac{\partial^2}{\partial x^2}\Psi(x)^* + V(x,t_0)\Psi(x)^* + 2\hbar\omega_\perp a_s \left[\Psi^*(x)\right]^2 \Psi(x)^* - \lambda\Psi(x)^*\right) \cdot \delta\Psi(x).$$

For a fixed total particle number the Lagrange parameter λ is the total energy of the system at time t_0. The latter expression has to vanish for all variations $\delta\Psi(x)$, thus the integral kernel has to vanish. We obtain a non-linear Schroedinger equation which is called the Gross-Pitaevskii equation

$$\left(-\frac{\hbar^2}{2m}\frac{\partial^2}{\partial x^2} + V(x,t_0) + 2\hbar\omega_\perp a_s \rho(x)\right)\Psi(x) = E\Psi(x). \tag{6.12}$$

This is a stationary Schrödinger equation with an additional mean-field interaction term that is proportional to the local particle-density $\rho(x) = |\Psi(x)|^2$. The time dependent version of the equation is given by

$$\left(-\frac{\hbar^2}{2m}\frac{\partial^2}{\partial x^2} + V(x,t) + 2\hbar\omega_\perp a_s \rho(x,t)\right)\Psi(x,t) = \mathbf{i}\hbar\frac{\partial}{\partial t}\Psi(x,t). \tag{6.13}$$

The only implicit approximation we have used so far is the description of the two-body interaction via a contact interaction. Of course we use the explicit approximation that the Bose-Einstein condensate does not interact with anything else, e.g., a thermal cloud of atoms.

6.2.2 Split-Operator Fast-Fourier Transformation Method

An efficient way to perform the time evolution for a one-body Schrödinger equation is the Split-Operator Fast-Fourier Transformation (SOFFT) method. Furthermore, this method can be used to find ground states of a stationary Schrödinger equation by evolving in imaginary time. We will derive the SOFFT method in the following.

The time-evolution operator $\hat{U}(t,t_0)$ can be formally obtained by integrating the Schrödinger equation:

$$\hat{U}(t,t_0) = \mathcal{T}\exp\left\{-\mathbf{i}/\hbar \int_{t_0}^{t} dt' \hat{H}(t')\right\}. \tag{6.14}$$

The operator $\mathcal{T}$ is responsible for the canonic ordering of the Hamiltonians for different times. For a numerical treatment, we need a discretized version of the time-evolution operator

$$\hat{U}(t_N, t_0) = \mathcal{T} \exp\left\{-\mathbf{i}/\hbar \sum_{n=1}^{N} \hat{H}(t_{n-1})\Delta t\right\}, \qquad \Delta t = t_{n+1} - t_n. \tag{6.15}$$

Writing down the Dyson series, the commutators $[\hat{H}(t_n), \hat{H}(t_{n'})]$ are of the order $(\Delta t)^2$. The nested commutators are of even higher orders in Δt. So we obtain

$$\hat{U}(t_N, t_0) = \prod_{n=1}^{N} \exp\left\{-\mathbf{i}/\hbar\hat{H}(t_{n-1})\Delta t\right\} + \mathcal{O}(\Delta t)^2 + \mathcal{O}(\Delta t)^3 + \cdots. \tag{6.16}$$

The Hamiltonian shall have a kinetic term $T(\hat{p})$ and a time dependent potential term $V(\hat{x}, t)$. We now derive the time-evolution operator for a single time step $t_0 \to t_1$. Writing down the Taylor series, splitting the kinetic from the potential, and separating terms of order $(\Delta t)^2$ we obtain

$$\begin{aligned}
\hat{U}(t_1, t_0) &= \mathcal{T} \exp\left\{-\mathbf{i}/\hbar\big(T(\hat{p}) + V(\hat{x}, t_0)\big)\Delta t\right\} \\
&= \exp\left\{-\mathbf{i}/\hbar\, T(\hat{p})\,\Delta t\right\} \cdot \exp\left\{-\mathbf{i}/\hbar\, V(\hat{x}, t_0)\,\Delta t\right\} + \mathcal{O}(\Delta t)^2.
\end{aligned} \tag{6.17}$$

Obviously this is the split-operator (SO) part of the SOFFT method.

The discrete N-step time-evolution of a state in coordinate space is given by:

$$\psi(x, t_N) = \big\langle\, x \,\big|\, \hat{U}(t_N, t_{N-1})\ldots\hat{U}(t_1, t_0) \,\big|\, \psi, t_0 \,\big\rangle. \tag{6.18}$$

For the sake of clarity we exemplarily continue for a single time step. We only account for linear terms in Eqs. (6.16) and (6.17), which introduces an error of order $(\Delta t)^2$ and consequently the time steps must be sufficiently small

$$\big\langle\, x \,\big|\, \hat{U}(t_1, t_0) \,\big|\, \psi, t_0 \,\big\rangle \approx \big\langle\, x \,\big|\, \exp\left\{-\mathbf{i}/\hbar\, T(\hat{p})\,\Delta t\right\} \cdot \exp\left\{-\mathbf{i}/\hbar\, V(\hat{x}, t_0)\,\Delta t\right\} \,\big|\, \psi, t_0 \,\big\rangle. \tag{6.19}$$

Now, we insert two unity operators in coordinate space and one unity operator in momentum space. Technically, this switching between the basis representations is done by Fast-Fourier Transformations (FFT):

$$\begin{aligned}
\big\langle\, x \,\big|\, \hat{U}(t_1, t_0) \,\big|\, \psi, t_0 \,\big\rangle &\approx \big\langle\, x \,\big|\, \hat{1}\ \exp\left\{-\mathbf{i}/\hbar\, T(\hat{k})\,\Delta t\right\}\ \hat{1}\ \exp\left\{-\mathbf{i}/\hbar\, V(\hat{x}, t_0)\,\Delta t\right\}\ \hat{1}\ \big|\, \psi, t_0 \,\big\rangle \\
&= \int dk' \int dk'' \int dx'\ \big\langle\, x \,\big|\, k' \,\big\rangle \big\langle\, k' \,\big|\, \exp\left\{-\mathbf{i}/\hbar\, T(k'')\,\Delta t\right\} \,\big|\, k'' \,\big\rangle \\
&\quad\cdot \big\langle\, k'' \,\big|\, \exp\left\{-\mathbf{i}/\hbar\, V(x', t_0)\,\Delta t\right\} \,\big|\, x' \,\big\rangle \big\langle\, x' \,\big|\, \psi, t_0 \,\big\rangle.
\end{aligned} \tag{6.20}$$

With the coordinate representation of a plane wave $\langle\, x \mid k \,\rangle = e^{-\mathbf{i}kx}$ we obtain

$$
\begin{aligned}
\langle\, x \mid \hat{U}(t_1, t_0) \mid \psi, t_0 \,\rangle &\approx \int dk' \int dk'' \int dx'\ e^{-\mathbf{i}k'x} e^{-\mathbf{i}/\hbar\, T(k'')\, \Delta t}\ \delta(k', k'') \\
&\qquad \cdot\ e^{-\mathbf{i}/\hbar\, V(x', t_0)\, \Delta t} e^{\mathbf{i}k''x'} \psi(x', t_0) \\
&= \int dk' \int dx'\ e^{-\mathbf{i}k'x} \cdot e^{-\mathbf{i}/\hbar\, T(k')\, \Delta t} \cdot\ e^{\mathbf{i}k'x'} \cdot e^{-\mathbf{i}/\hbar\, V(x', t_0)\, \Delta t} \cdot \psi(x', t_0)
\end{aligned}
\tag{6.21}
$$

To summarize, first, the potential-energy term of the time-evolution operator acts on the wavefunction in coordinate space. Second, the resulting wavefunction is fourier-transformed to momentum space and the kinetic-energy term of the time-evolution operator acts on it. Finally, we fourier transform again to coordinate space. This scheme is iterated until the algorithm has evolved to the desired time. The most prominent feature of the algorithm is that there is no need to store matrices because the wavefunction is always transformed to the eigenbasis of the respective operators that appear in the Hamiltonian.

Besides the discretization in coordinate space, the error of the SOFFT method seems only to be the neglected non-linear orders of Δt. However, the discretization of the time includes another subtle approximation. For the step-wise evolution of the wavefunction

$$
\psi(x, t_{i+1}) = e^{-\mathbf{i}/\hbar\left(-\frac{\hbar^2}{2m}\frac{\partial^2}{\partial x^2} + V(x, t_i) + 2\hbar\omega_\perp a_s \rho(x, t_i)\right)} \psi(x, t_i)
\tag{6.22}
$$

we arbitrarily employ the potential $V(x, t_i)$ and the density $\rho(x, t_i)$ at the beginning of the time interval Δt. To justify this, we have to assume a negligible change of these terms during the time interval. The natural check for convergence is again done by employing smaller time steps Δt until the results do not change any more.

6.2.3 Simulations – Free Evolution

The first experimental goal is to observe interference patterns of the Bose-Einstein condensate inside the quasi one-dimensional ring potential. Due to the finite optical resolution there is a constraint on the size of the interference structures. Furthermore, the contrast, given by the density variations, has to be high enough. In order to obtain first insights to the relevant length scales and densities, we use the above framework to time evolve a Bose-Einstein condensate of $N = 4000$ ^{87}Rb atoms in the one-dimensional ring potential.

We start with a free evolution of a Gaussian wavepacket of the form

$$G(x, t_0) = \sqrt{N} \left(\pi \sigma_0^2 \right)^{1/4} e^{-\frac{x^2}{2\sigma_0^2}} \tag{6.23}$$

with width $\sigma_0 = 20\,\mu\text{m}$. The expected coherence times of the condensate are about 100 ms. In the current experiment, the ring potential has a diameter of $d = 1.5$ mm. A simulation of the time-evolution is shown in Figure 6.3(a). After 200 ms the atoms are distributed over roughly a third of the optical ring. Since the expected coherence times in the experiment are about 100 ms, a free evolution of the BEC in a ring with this diameter will probably not yield visible interference patterns. Yet, a ring with diameter $d = 0.15$ mm is completely circled by a fraction of the atoms after 80 ms as shown in Figure 6.3(b). The appearance of the inner cone is a result of the initial Gaussian wavepacket. The large interaction energy at the dense center of the initial Gaussian wavepacket provides particles with kinetic energy and they pass the particles from the tails of of the Gaussian at about 20 ms. The inset in 6.3(b) shows a zoom of the resulting interference pattern in the upper right corner of the picture. Considering the results of the simulations we suggest that an optical ring with a diameter clearly smaller than $d = 1.5$ mm provides a more promising geometry for the experiment.

6.2.4   Simulations – Guided Evolution

The aim of the experiment is not a free evolution of the atoms, but to guide them with an optical potential. A first approximation of the additional potential resulting from an elongated laser that is moved over the ring lense is given by a Gaussian of the form:

$$V(x, t) = -V_0 e^{-\frac{1}{2} \frac{(|x| - v_L t)^2}{(\sigma_{\text{pot}})^2}} \,, \tag{6.24}$$

where V_0 is the depth of the potential and v_L the velocity of the laser moving over the ring lense. The time dependent velocity in tangential direction can be derived to

$$v(t) = \sqrt{\frac{r^2 v_L}{2rt - v_L t^2}} \,. \tag{6.25}$$

We use width of $\sigma_{\text{pot}} = 100\,\mu\text{m}$ for the potential and the velocity of the laser shall be $v_L = 1.75$ mm/s. Potentials $V(x, t)$ for $V_0 = 0.15\,k_B\mu\text{K}$ and different times are shown in Figure 6.4.

We start the time evolution with a solution of the Gross-Pitaevskii equation at time $t_0 = 0$. The resulting simulation with a potential depth of $V_0 = 0.15\,k_B\mu\text{K}$ is shown
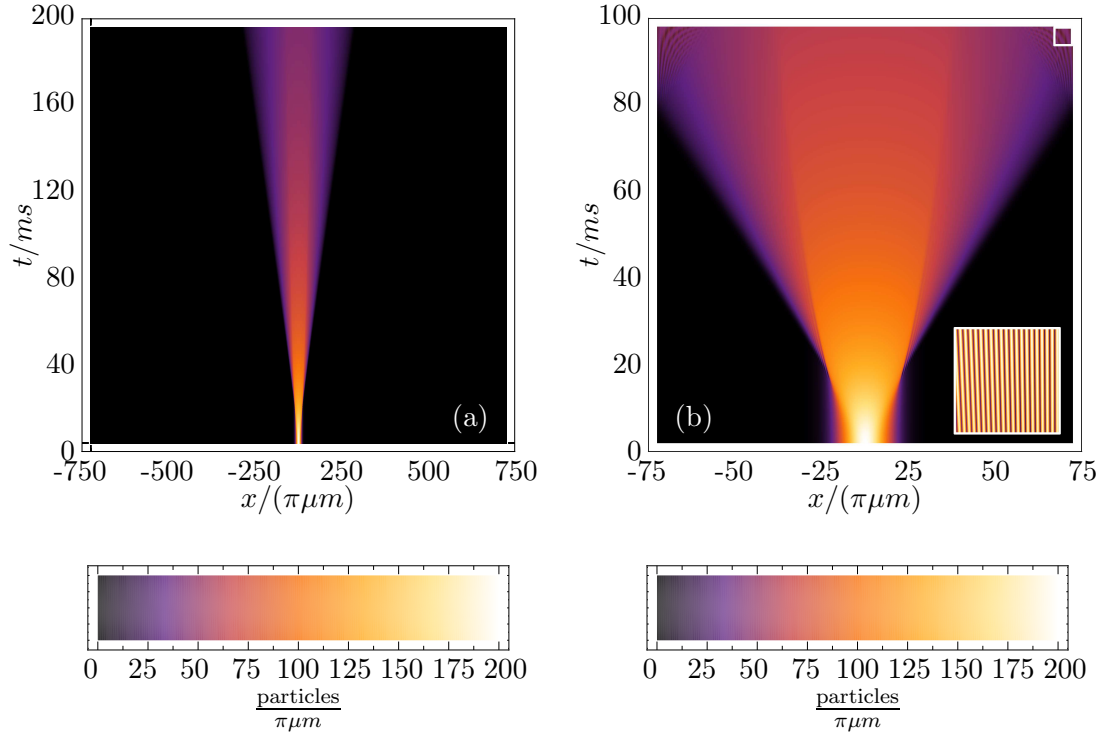
Figure 6.3: Time evolution of 4000 ^{87}Rb atoms with a coordinate-time grid of $N_x = 8000$, $N_t = 8000$ points. (a) Large ring with diameter $d = 1.5$ mm. (b) Small ring with diameter $d = 0.15$ mm. The inset in (b) shows a zoom of factor 6 into the upper right corner. The magnified section is about $20 \times 20 \, \mu\text{m}^2$.

in Figure 6.5(a). As a consequence of the growing barrier at the origin of the ring, the Bose-Einstein condensate is quickly divided into two parts. Both parts follow the potential minima and meet at the opposite side of the ring after about 70 ms. The size of the interference pattern is similar to those in Figure 6.3(b).

A more comprehensive discussion of the subject employing a realistic experimental potential with a variety of different parameters for the potentials depth and geometries of the optical ring was subject of a Bachelor thesis [59].
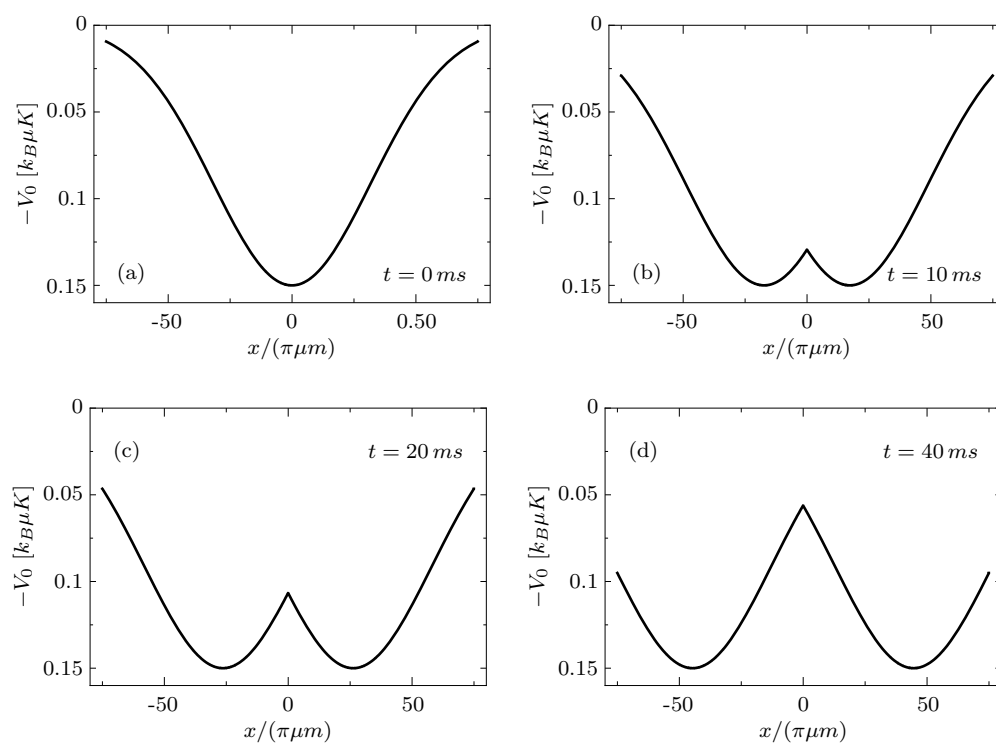
Figure 6.4: Guiding potential for the Bose-Einstein condensate.
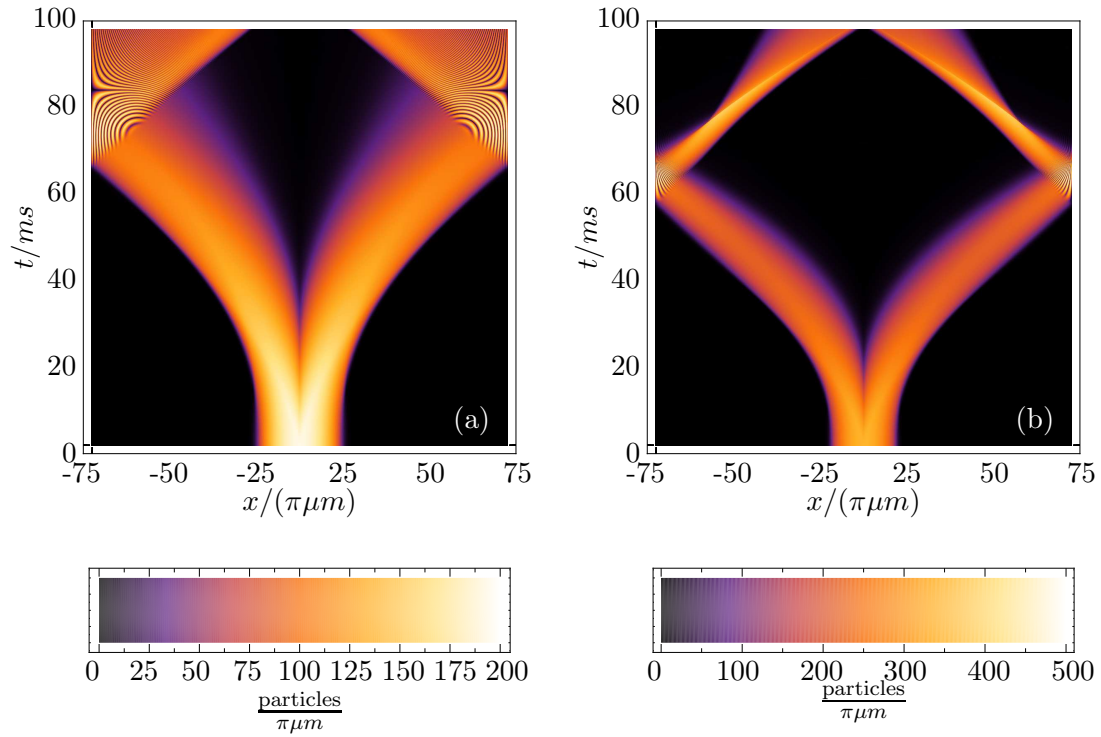
Figure 6.5: Time evolution of 4000 ^{87}Rb atoms in a guiding potential. The parameters are: $d = 150\,\mu$m, $N_x = 10^4$, $N_t = 10^4$. (a) potential depth $V_0 = 0.15\,k_B\mu$K, (b) potential depth $V_0 = 0.30\,k_B\mu$K

Appendix A

Appendix

A.1 From 3D Contact Interaction to 1D Contact Interaction

We start with the 3D contact interaction

$$u_{3D}(\vec{x}, \vec{x}') = \frac{4\pi a_s \hbar^2}{m}\, \delta^{(3)}(\vec{x} - \vec{x}') \tag{A.1}$$

and assume a 1D Gauss function for the two remaining spatial directions

$$G(y) = \left(\frac{m\omega_y}{\pi\hbar}\right)^{1/4} e^{-\frac{m\omega_y}{2\hbar}y^2}\,. \tag{A.2}$$

The integral over 4th power of the Gaussian leads to

$$\int_{-\infty}^{\infty} dy |G(y)|^4 = \left(\frac{m\omega_y}{\hbar 2\pi}\right)^{1/2}\,. \tag{A.3}$$

Putting these terms together, we obtain the 1D contact interaction

$$u_{1D}(x, x') = \int_{-\infty}^{\infty} dy \int_{-\infty}^{\infty} dy' \int_{-\infty}^{\infty} dz \int_{-\infty}^{\infty} dz' |G(y)|^2 |G(z)|^2 \, u_{3D}(\vec{x}, \vec{x}')\, |G(y')|^2 |G(z')|^2$$
$$= 2\omega_\perp \hbar\, a_s\, \delta(x - x')\,, \tag{A.4}$$

where we used $\omega_y = \omega_z = \omega_\perp$.

A.2   Oscillator Length

The definition of the oscillator length for $H_x = -\frac{\hbar^2}{2m}\frac{\partial^2}{\partial x^2} + \frac{m\omega^2}{2}x^2$ is given by

$$a_0 = \sqrt{\frac{\hbar}{m\omega}}\,. \tag{A.5}$$

In the vicinity of a lattice site we approximate the optical potential by

$$V_{opt}(x) = sE_r \sin^2\left(\frac{2\pi}{\lambda}x\right) \approx sE_r\left(\frac{2\pi}{\lambda}\right)^2 x^2 \tag{A.6}$$

and therefore,

$$\omega = \sqrt{\frac{2sE_r}{m}}\frac{2\pi}{\lambda} \ \ \text{with} \ \ E_r = \frac{\hbar^2 4\pi^2}{2\lambda^2 m}\,.$$

This leads to the following approximation of the oscillator length

$$a_0 = \frac{\lambda}{2\pi}\left(\frac{V_0}{E_r}\right)^{1/4}\,. \tag{A.7}$$

A.3   Analytic Interaction Matrix Element

At the center of a lattice well we approximate

$$V_{opt}(x) = sE_r \sin^2\left(\frac{2\pi}{\lambda}\right)x^2 \approx \underbrace{sE_r\left(\frac{2\pi}{\lambda}\right)^2}_{1/2m\omega^2}x^2\,. \tag{A.8}$$

With the assumption that the Wannier function is a Gaussian function (A.4) the integral is (A.3):

$$U = 2\omega_\perp \hbar a_s \int dx\,|w_{\xi_l}(x)|^4 \approx 2\omega_\perp \hbar a_s \int dx\,|G(x)|^4 = 2\omega_\perp \hbar \frac{a_s}{\lambda}\left(4\pi^2\frac{V_0}{E_r}\right)^{1/4}\,. \tag{A.9}$$

A.4 Hubbard Parameters for Different Transverse Trapping Frequencies

A transverse trapping frequency of $\omega_\perp = 2\pi\, 16.3$ kHz reproduces the Hubbard parameters in Fig. 5.16 in Ref. [10]. A transverse trapping frequency of $\omega_\perp = 2\pi\, 37.5$ kHz results from the the assumption of a transverse harmonic trapping with potential depth $V_\perp = 30\, E_r$.

	independent of $\omega_\perp$	$\omega_\perp = 2\pi\, 16.3$ kHz		$\omega_\perp = 2\pi\, 37.5$ kHz	
$s = V_0/E_r$	J/E_r	U/E_r	U/J	U/E_r	U/J
1	0.1781	0.1294	0.7268	0.2979	1.6724
2	0.1428	0.1571	1.1005	0.3609	2.5283
3	0.1110	0.1799	1.6208	0.4131	3.7208
4	0.0855	0.1992	2.3302	0.4571	5.3475
5	0.0658	0.2156	3.2782	0.4947	7.5215
6	0.0508	0.2297	4.5245	0.5299	10.380
7	0.0394	0.2421	6.1411	0.5552	14.088
8	0.0308	0.2530	8.8215	0.5803	18.843
9	0.0242	0.2628	10.849	0.6028	24.885
10	0.0192	0.2717	14.168	0.6232	32.494
11	0.0153	0.2798	18.319	0.6419	42.009
12	0.0122	0.2874	23.473	0.6593	53.824
13	0.0099	0.2944	29.837	0.6754	68.408
14	0.0080	0.3010	37.650	0.6905	86.308
15	0.0065	0.3072	47.194	0.7047	108.17

A.5 Units and Constants

$\hbar$	$1.05457 \cdot 10^{-34}$ Js	Planck's Constant
k_B	$1,38 \cdot 10^{-23}$ J/K	Boltzmann's Constant
u	$1.66 \cdot 10^{-27}$ Kg	atomic mass unit
m	86.909 u	mass of ^{87}Rb
r_{Bohr}	$5.2918 \cdot 10^{-11}$ m	Bohr radius
a_s	$109\, r_{\mathrm{Bohr}}$	s-wave scattering length of ^{87}Rb

Bibliography

[1] A. Einstein
"Quantentheorie des einatomigen idealen Gases",
Sitzungsberichte der preussischen Akademie der Wissenschaften (1924)

[2] S. N. Bose
"Plancks Gesetz und Lichtquantenhypothese",
Zeitschrift für Physik **26***, 178 (1924)*

[3] J. Bardeen, L. N. Cooper, and J. R. Schrieffer
Phys. Rev. **108***, 1175 (1957)*

[4] K. B. Davis, M. O. Mewes, M. R. Andrews, N. J. van Druten, D. S. Durfee, D. M. Kurn, and W. Ketterle
Phys. Rev. Lett. **75***, 3969 (1995)*

[5] M. H. Anderson, J. R. Ensher, M. R. Matthews, C. E. Wieman, and E. A. Cornell
Science **269***, 198 (1995)*

[6] I. Bloch
Nature Physics **1***, 23 (2005)*

[7] J. Hubbard
Proc. Roy. Soc. A **276***, 238 (1963)*

[8] M. P. A. Fisher, P. B. Weichmann, G. Grinstein, and D. S. Fisher
Phys. Rev. B **40***, 546 (1989)*

[9] M.Greiner, O. Mandel, T. Esslinger, T. W. Hänsch, and I. Bloch
Nature (London) **415***, 39 (2002)*

[10] T. Stöferle, H. Moritz, C. Schori, M. Köhl, and T. Esslinger
Phys. Rev. Lett. **92***, 130403 (2004)*

[11] D. van Oosten, P. van der Straten, and H. T. C. Stoof
Phys. Rev. Lett. A **63***, 053601 (2001)*

[12] G. G. Batrouni, V. Rousseau, R. T. Scalettar, M. Rigol, A. Muramatsu, P. J. H. Denteneer, and M. Troyer
*Phys. Rev. Lett. **89**, 117203 (2002)*

[13] G. G. Batrouni, V. Rousseau, R. T. Scalettar
*Phys. Rev. B **46**, 9051 (1992)*

[14] J. K. Freericks and H. Monien
*Phys. Rev. B **53**, 2691 (1996)*

[15] R. Roth and K. Burnett
*Phys. Rev. A **68**, 023604 (2003)*

[16] R. Roth and K. Burnett
*J. Phys. B: At. Mol. Opt. Phys. **37**, 3893 (2004)*

[17] S. Rapsch, U. Schollwöck, and W. Zwerger
*Europhys Lett. **46**, 559 (1999)*

[18] G. Roux, T. Barthel, I. P. McCulloch, C. Kollath, U. Schollwöck, and T. Giamarchi
*Phys. Rev. A **78**, 023628 (2008)*

[19] Prof. Dr. Gerhard Birkl
Atoms - Photons - Quanta Group, TU Darmstadt

[20] W. Jones and N. H. March
University of Rochester New York,
Theoretical Solid State Physics, Volumes 1+2 (1973)

[21] R. Grimm, M. Weidemüller, Y. B. Ovchinnikov
*Adv. At. Mol. Opt. Phys. **42**, 95 (2000)*

[22] N. Marzari, I. Souza, and D. Vanderbilt
*Psi-K Newsletter **57**, (2003), http://www.psi-k.org*

[23] N. Marzari and D. Vanderbilt
*Phys. Rev. B **56**, 12847 (1997)*

[24] D. Jaksch, C. Bruder, J. I. Cirac, C. W. Gardiner, and P. Zoller
*Phys. Rev. Lett. **81**, 3108 (1998)*

[25] I. Bloch, J. Dalibard, and W. Zwerger
*Rev. Mod. Phys. **80**, 885 (2008)*

[26] L. Fallani, J. E. Lye, V. Guarrera, C. Fort, and M. Inguscio
*Phys. Rev. Lett. **98**, 130404 (2007)*

[27] J. Li, Y. Yu, A. M. Dudarev, and Q. Niu
*New J. Phys. **8**, 154 (2006)*

[28] R. Roth and K. Burnett
*Phys. Rev. A **67**, 031602 (2003)*

[29] J. E. Lye, L. Fallani, C.Fort, V. Guarrera, M. Modugno, D. Wiersma, C. Fort, and M. Inguscio
*Phys. Rev. A **75**, 061603 (2007)*

[30] O. Penrose and L. Onsager
*Phys. Rev. **104**, 576 (1956)*

[31] C. N. Yang
*Phys. Mod. Rev. **34**, 694 (1962)*

[32] M. Hild, F. Schmitt, and R. Roth
*J. Phys. B: At. Mol. Opt. Phys. **39**, 4547 (2006)*

[33] M. Hild, F. Schmitt, I. Türschmann, and R. Roth
*Phys. Rev. A **76**, 053614 (2007)*

[34] Arpack Software
Source: http://www.caam.rice.edu/software/ARPACK/

[35] G. Modugno, G. Roati, F. Riboli, F. Ferlaino, R. J. Brecha, M. Inguscio
*Science **27**, 297 (2002)*

[36] M. Köhl, H. Moritz, Th. Stöferle, K. Günter, and T. Esslinger
*Phys. Rev. Lett. **94**, 080403 (2005)*

[37] K. Günter, T. Stöferle, H. Moritz, M. Köhl, and T. Esslinger
*Phys. Rev. Lett. **96**, 180402 (2006)*

[38] R. Roth and K. Burnett
*Phys. Rev. A **69**, 021601(R) (2004)*

[39] M. Lewenstein, L. Santos, M. A. Baranov, and H. Fehrmann
*Phys. Rev. Lett. **92**, 050401 (2004)*

[40] F. Schmitt, M. Hild, and R. Roth
J. Phys. B: At. Mol. Opt. Phys. **40**, *371 (2007)*

[41] R. Pugatch, N. Bar-gill, N. Katz, E. Rowen, and N. Davidson
Preprint cond-mat/0603571 (2006), Identifying the Bose glass phase

[42] R. Roth, P. Navratil
Phys. Rev. Lett. **99**, *092501 (2007)*

[43] R. P. Feynman, Frontiers in physics
Statistical Mechanics, A set of lectures (1972)

[44] S. R. White
Phys. Rep. **301**, *187 (1998)*

[45] U. Schollwöck
Rev. Mod. Phys. **77**, *259 (2005)*

[46] K. A. Hallberg
Adv. in Phys. **55**, *477 (2006)*

[47] K. G. Wilson
Rev. Mod. Phys. **47**, *773 (1975)*

[48] P. A. Lee
Phys. Rev. Lett. **42**, *1492 (1979)*

[49] S. Binder
The Numerical Renomalization Group applied to the Bose-Hubbard Model,
Bachelor Thesis, TU Darmstadt (2007)

[50] S. R. White and R. M. Noack
Phys. Rev. Lett. **68**, *3487 (1992)*

[51] S. R. White
Phys. Rev. B **48**, *10345 (1993)*

[52] G. K.-L. Chan and M. Head-Gordon
J. Chem. Phys. **116**, *4462 (2002)*

[53] F. Schmitt, M. Hild, and R. Roth
Phys. Rev. A **80**, *023621 (2009)*

[54] T. D. Kühner, S. R. White, and H. Monien
Phys. Rev. B **61**, *12474 (2000)*

[55] S. R. Clark and D. Jaksch
New J. Phys. **8**, *160 (2006)*

[56] A. Lengwenus
Manipulation der internen und externen Freiheitsgrade neutraler Atome in optischen Mikropotentialen,
PhD Thesis, TU Darmstadt (2008)

[57] F. Dalfovo, S. Giorgini, P. Pitaevskii, and S. Stringari
Rev. Mod. Phys. **71**, *463 (1999)*

[58] A. L. Migdall, J. V. Prodan, and W. D. Phillips
Phys. Rev. Lett. **54**, *2596 (1985)*

[59] L. Görgen
Dynamik von Bose-Einstein-Kondensaten in eindimensionalen optischen Ringpotentialen, Bachelor Thesis, TU Darmstadt (2009)

Acknowledgments

First of all, I would like to thank Professor Robert Roth for being an outstanding mentor. All the years I worked as a member of his group were a great pleasure for me. I really appreciate his enduring support for my scientific work. But even more, I appreciate that his support reached far beyond.

A lot of thanks to Professor Jochen Wambach for reviewing this thesis.

I would also like to thank my colleagues: Markus Hild for his friendship during our studies and of course for becoming my groomsman, Heiko Hergert for proofreading this thesis and many fruitful discussions, and Mathias Wagner and Verena Kleinhaus for the relaxing coffee brakes. The rest of the theory group as well as Genette Kluckner provided a very pleasant working environment, thanks to all of you.

Special thanks go to my family: my mother Monika for many, many things, my brother Florian for encouraging me to proceed with my studies, and my wonderful wife Alexandra for her love; you are a true Ally.

Thanks to all my friends, in particular to Stefan Friedrich and his family, and to Jens Engemann for always bringing me back down to earth.